The two-dimensional vibrating reed technique: A study of anisotropic pinning in high-temperature superconductors

Der Universität Bayreuth
zur Erlangung des Grades eines
Doktors der Naturwissenschaften (Dr. rer. Nat)
vorgelegte Abhandlung

von

Anna Karelina

aus Moskau

1. Gutachter: Prof. Dr. Hans F. Braun
2. Gutachter: Prof. Dr. Lothar Kador

Tag der Einreichung: 16.12.2003
Tag des Kolloquiums: 18.02.2004

Contents

Chapter 1

Introduction

The discovery in 1986 of the superconductivity at 35 K in an oxide of La, Ba and Cu by Bednorz and Müller [1] revealed a new class of superconducting materials with unique properties and unexpectedly high temperature of the superconducting transition. All these compounds have layered structure consisting of the copper oxide planes, which determine the superconducting properties. This type of materials did not behave as ordinary BCS superconductors. The tunnelling measurement shows that the energy gap is not fully formed [2, 3]. Also, the thermodynamic, optical and transport properties exhibit power-law rather than exponential temperature dependence [for example, 4, 5].

The numerous experiments show that these superconductors may have an unconventional pairing state with an order parameter that has symmetry different from that of the isotropic s-wave state. The experiments on NMR relaxation [6] gave direct evidence of spin-singlet pairing. Thus most of the attention was focused on a particular state with d-wave symmetry first suggested by N. E. Bickers et al. [7]. This state has a four-fold symmetry of the magnitude of the order parameter and exhibits nodes and lobes in the energy gap aligned with the in-plane lattice vectors.

The possible effect of the pairing state on the pinning forces and the dynamic properties of the flux line lattice is an open question. It is reasonable to expect the appearance of a

four-fold symmetry in the pinning potential. To study this question the vibrating reed technique may be very useful.

The vibrating reed technique was proved to be a powerful tool to study the dynamics of the flux lines and the pinning forces acting on them [8]. In particular, this is a reliable method to measure the curvature of the pinning potential (Labusch parameter) for thin samples. To determine the symmetry of the pinning potential it is necessary to measure the Labusch parameter for vortex motion in planes aligned parallel to the crystallographic c-axis, but oriented at different angles relative to the a- or b-direction. Such a motion can be easily produced with the vibrating wire with two degrees of freedom instead of the vibrating cantilever. The construction and use of this device is described in this work, and results obtained on single crystals of $YBa_2Cu_3O_{7-\delta}$ and $Bi_2Sr_2CaCu_2O_{8+\delta}$ are presented.

Chapter 2

Theoretical description of pinning potential

2.1. Vortices in the high temperature superconductors

The discovery of high-temperature superconductors [1] was very exciting since it revealed a new class of superconducting materials with unique properties and unexpectedly high temperature of the superconducting transition. Within several years new materials were discovered such as $YBa_2Cu_3O_{7-\delta}$, $Bi_2Sr_2CaCu_2O_{8+\delta}$ and $Tl_2Ba_2Ca_nCu_{n+1}O_{6+2n}$ with the T_c equal 93 K, 110 K and 130 K respectively. All these compounds consist of superconducting copper oxide planes separated by non-superconducting blocks. This layered structure of the materials results in their large effective mass anisotropy between the directions c (011) and a (001) or b (010). The anisotropy in the ab-plane is much smaller.

Compared to conventional superconductors the cuprate compounds are characterized by a small value of coherence length ξ, which is the typical length scale for spatial variations of the order parameter $|\Psi|^2$. Typical values of ξ are about $1 \div 2$ nm. In contrast, the penetration depth λ is larger than in conventional superconductors and is about $100 \div 250$ nm. Thus, the Ginzburg-Landau parameter is very large $k = \lambda / \xi \gg 1$. That means that high-temperature cuprate compounds are type II superconductors.

Thus, an external magnetic field can penetrate into the high-T_c superconductor as an arrangement of parallel magnetic flux lines, each carrying an elementary flux quantum $\Phi_0 = h/2e$. These flux lines, or vortices, consist of a core with radius $\approx \xi$ where the order parameter and density of superconducting electrons are depressed. This core is surrounded by shielding currents extending over a region with radius λ.

Vortex motion, driven by Lorentz force, leads unavoidably to dissipation of energy and to a non-zero resistivity of the superconductor. Fortunately, vortices can be pinned by defects in the crystal structure such as dislocations, vacancies, grain and twin boundaries and columnar defects. Therefore, pinning of flux lines plays an essential role in establishing high critical current density.

2.2. s- and d-wave symmetry in the cuprate superconductors

Since the discovery of the high temperature superconductors the question of the superconducting pairing mechanism was actively studied. It was recognised that these materials did not behave as ordinary superconductors. For example there was extensive experimental evidence which shows that the energy gap is not fully formed. This is revealed in tunnelling measurements that display a high sub-gap density of states [2, 3]. These experimental results suggested that HTSCs may exhibit an unconventional pairing state.

The allowed symmetries for the pairing state are described in reference [4]. The experiments with NMR relaxation rates and Knight shift gave direct evidence of spin-singlet pairing [6], so the only two possibilities left are s-wave and d-wave symmetry.
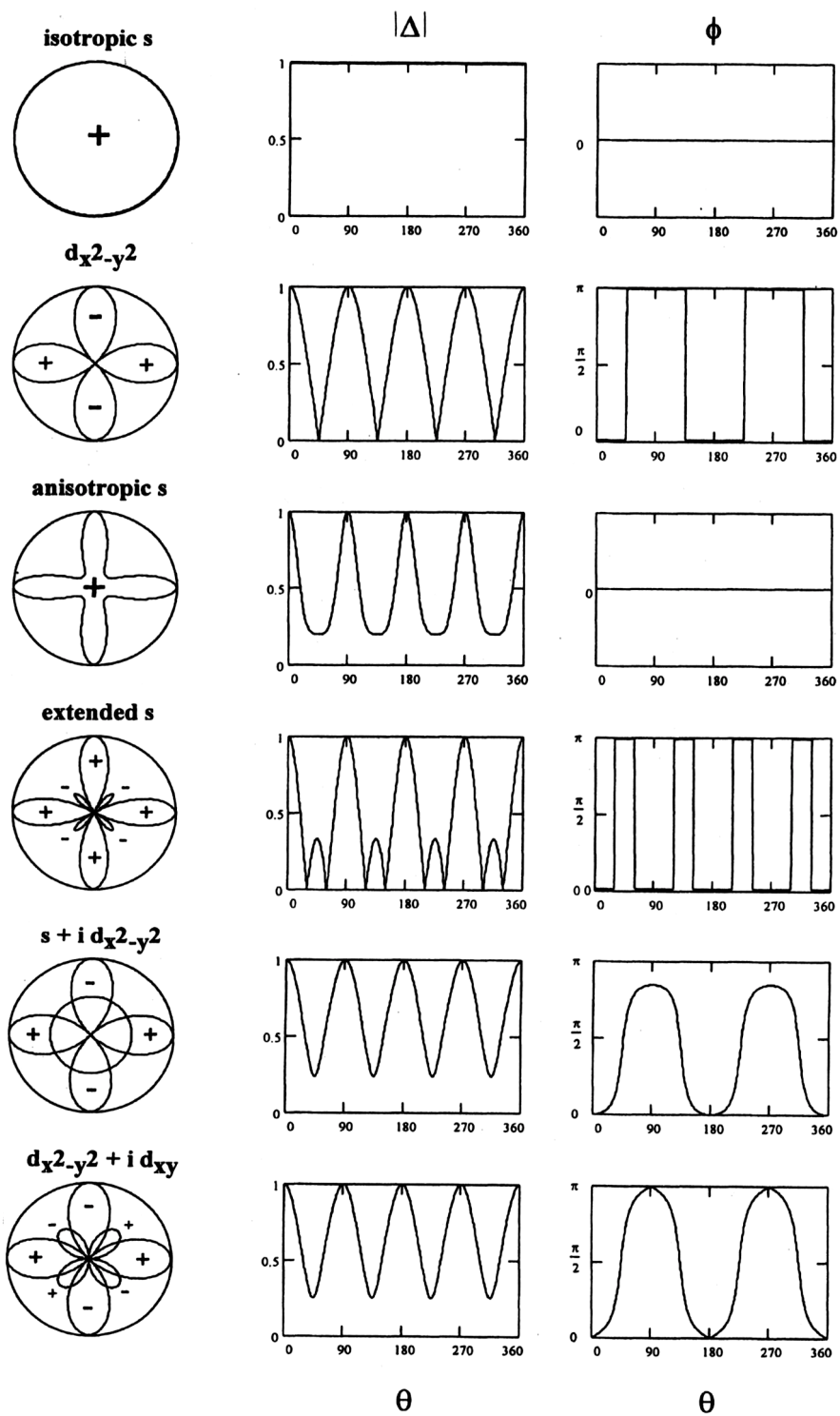
Figure 2.2.1. *Magnitude and phase of the superconducting order parameter as a function of direction in k-space for the main candidate pairing states. Taken from [15].*

Determination of the symmetry of the pairing state is possible by direct measurement of the anisotropy of the order parameter. The magnitudes and the phase of the order parameter as function of k-space direction are shown in Fig.2.2.1. For symmetries other than the conventional s-wave the magnitude has a modulation with four-fold symmetry. In all these cases a depression of the order parameter exists in the (110) direction. The reduced gap along some directions results in an excess of excited quasiparticles and can be observed in transport measurements and tunnelling spectra. Many experiments such as NMR spectroscopy [9], angle-resolved photoemission [10], scanning tunneling microscopy [11], Raman scattering [12], angle resolved torque magnetometry [13, 14] and so on, have shown the spatial anisotropy and gave evidence for four-fold symmetry in magnitude. However impurities can obscure the presence of zero magnitude of the order parameter in nodes. This prevents determination of the pairing state by the magnitude sensitive experiments. Thus, it is necessary to probe the phase of the order parameter in different directions of k-space which is different for the various states. In particular, the s-wave state has a uniform phase whereas the d-wave state exhibits discontinuous jumps of π at the (110) direction with sign change of the order parameter. For the $s+id$ and $d+id$ mixture states the phase varies continuously with angle. The interferometer experiments sensitive to the phase of the order parameter in different directions were carried out. These experiments are reviewed in [15]. This is the most direct experiments based on dc SQUID and on single Josephson junctions.

The main idea of the two-junction interferometer (dc SQUID) experiment [16, 17] is demonstrated in Fig.2.2.2. The Josephson tunnel junctions are fabricated on the orthogonal surfaces of a single crystal of a high-temperature superconductor. The junctions are joined by a loop of a conventional s-wave superconductor. For s-wave symmetry the phase of the order parameter is the same at each junction so the circuit behaves as an ordinary dc SQUID and the critical current is a maximum for zero flux. The circulating supercurrent at this point is zero. In contrast, for d symmetry the order parameter has an intrinsic phase shift π between a and b directions. At zero applied field the junction currents are exactly out of phase and a circulating current flows to maintain phase coherence around the loop. As a result at zero flux the critical current will be

minimal. The experimental measurements of the resistance and current-voltage characteristics shows evidence for a phase shift of order π between a and b directions which is consistent with the d pairing state.
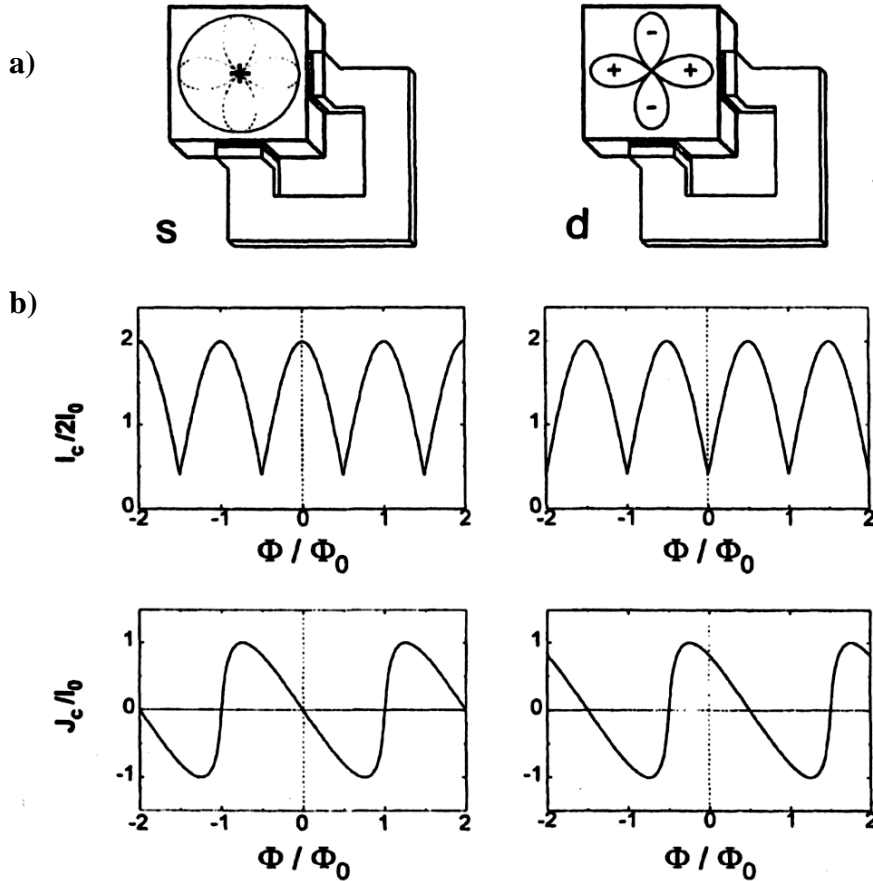
Figure 2.2.2. *a) The scheme of the dc-SQUID experiment. The Josephson tunnel junctions are connected to a (001) and b (010) surfaces of YBCO single crystal.*

b) The modulation of the critical current vs applied magnetic flux for s-wave and d-wave symmetries (taken from [15]).

Another way to explore the phase difference between directions is the single Josephson junction modulated experiment [18]. In this experiment one measures the critical current of a junction fabricated on the corner of the crystal as shown in Fig.2.2.3. In this geometry part of the tunnelling is into the (001) face of the crystal and part is into (010)

7

face. For an s-wave superconductor with isotropic phase the critical current would have the usual Fraunhofer diffraction pattern. However in case of a d-wave sample the order parameter in the *a* (001) and *b* (010) directions would be of opposite sign resulting in a modified pattern. At zero field in this case the currents through the orthogonal faces cancel and critical current would be zero. So the key feature to distinguish pairing states is a peak or a dip in the critical current at zero field. The experimental data shows the dip at zero flux and this is evidence for d-wave paring.
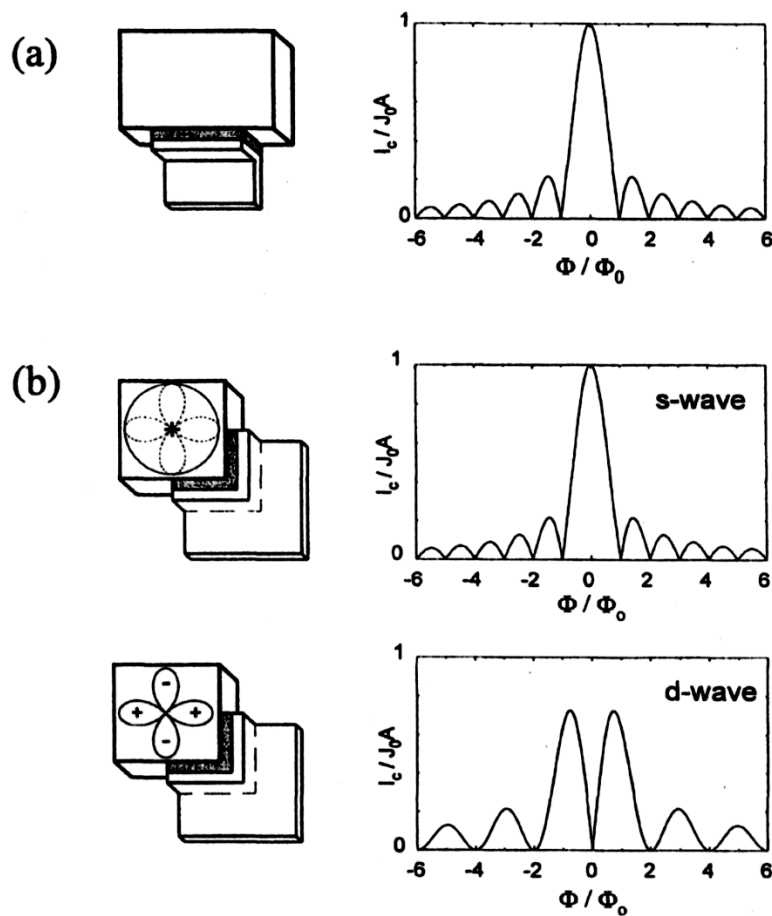
Figure 2.2.3. *a) The scheme of a single junction experiment.*
b) Fraunhofer diffraction pattern for the critical current modulation of a single Josephson junction with applied magnetic field for s-wave and d-wave symmetries (taken from [15])

However in spite of such strong evidence the answer to the question of pairing of high temperature superconductors is not so straightforward. The fact is there are some experiments demonstrating s-wave behaviour of HTSCs as c (110) axis Josephson tunnelling [19] and a hexagonal interference experiment [20].

Recent discussions result in the assumption that unconventional superconductors may have a mixture of d-wave and s-wave states. It was recognized that the order parameter of HTSCs may be unstable in the presence of perturbations at surfaces and interfaces or in presence of nonmagnetic and magnetic impurities [21]. A $d_{x^2-y^2} + is$ or $d_{x^2-y^2} + id_{xy}$ pairing state has been suggested near a surface or twin boundary with (110) orientation [22, 23]. The difficulty is that most phase sensitive experiments involve surface or boundary properties of HTSCs and many experiments suggested that the surface order parameter is not necessarily the same as the bulk order parameter.

2.3. Pinning in unconventional superconductors

It is an interesting question how the pairing state affects the symmetry of the pinning properties and vortex dynamics. Since in the d-wave state the order parameter has four-fold symmetry, it is reasonable to expect the appearance of this symmetry in the pinning potential. Unfortunately the experiments demonstrating four-fold symmetry of pinning are rather scarce. There is an interesting result in torque magnetometry [13, 14, 24] where four-fold symmetry in intrinsic intraplane pinning was observed (see Fig.2.3.1).

For better understanding the effect of the pairing state on the pinning symmetry it is necessary to model the interaction of a single flux line and point defect, and then to carry out the summation of these elementary forces for a random distribution of pinning centres.
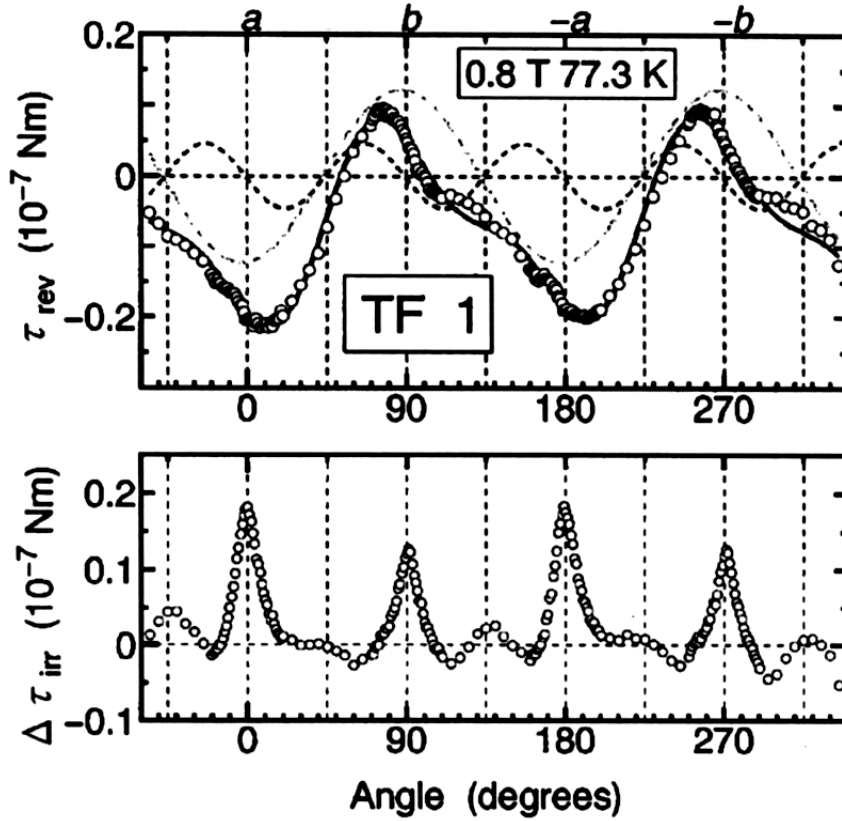
Figure 2.3.1. *The reversible and irreversible torque of the YBa$_2$Cu$_3$O$_{7-\delta}$ untwinned single crystal upon rotating the field (0.8 T) around the c(110) axis at a temperature of 77.3 K. The lines for τ_{rev} represent the twofold torque, the fourfold torque and their sum. In the lower figure, the isotropic twofold sinusoidal torques are subtracted from the irreversible torque τ_{irr}. Taken from [13].*

The shape of the pinning potential for a single pancake vortex and a point pinning center has been calculated by M.Endres [25] in the group of Prof. D.Rainer using the method described in classical work [26]. The main idea of this method is that pinning is caused not by suppression of superconducting condensation near the pinning center, but by quasiparticle scattering on the center. In case of small impurities of size d in the superconductor with coherence length ξ_0 the new mechanism leads to pinning energies larger by the factor ξ_0/d than the energy from the excluded volume effect. For calculating the defect pinning potential the quasiclassical method (equivalent to the

10

WKB method of quantum mechanics) was applied. The defects are modelled by a point scattering center. The superconductor was assumed two-dimensional with an isotropic Fermi surface and with either d-wave or s-wave symmetry. The modelling was performed in the unitary limit at a temperature $T = 0.3\ T_c$. The results of the calculations are shown in Fig.2.3.2 - 2.3.5. The length scale used in the figures is the coherence length $\xi_0 = v_F/2\pi$, the energy is given in units of the critical temperature T_c. Figure 2.3.2 shows the pinning potential as a function of the distance between vortex core and defect for isotropic s-wave and for d-wave along one of the crystal axes and at 45° to it. The difference in absolute value of the pinning for the two pairing states is not large enough to be measured. The difference of the potential in two different directions for d-wave is also very small.
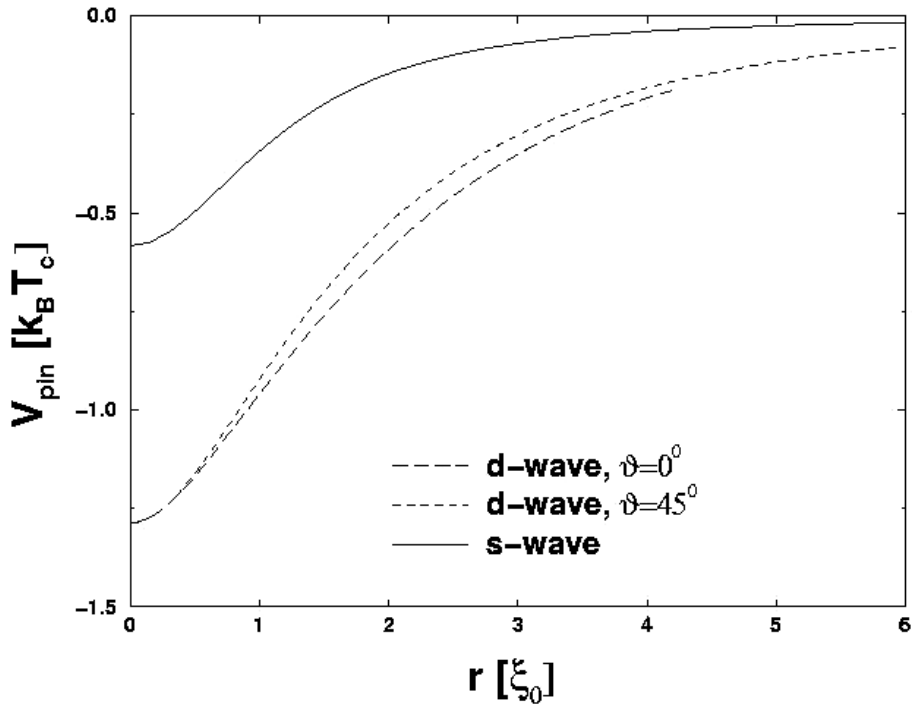
Figure 2.3.2. *Pinning potential as a function of the distance from the pinning centre for s-wave and d-wave. In case of d-wave calculation was made for two directions: along one of the crystal axes and under 45°.*

The shape of the pinning potential in the CuO_2 plane for d-wave symmetry of the order parameter is shown in Fig.2.3.3. As it was reasonably assumed before, the four-fold symmetry of order parameter and gap results in four-fold symmetry of the pinning potential and the equipotential lines deviate from circles. When a vortex is moved away from the pinning center, the pinning potential anisotropy leads to the appearance of a restoring force component perpendicular to the deflection of the vortex from the pinning center. This transverse force is directed towards a higher value of the order parameter. Obviously this force is equal to zero for deviations along an axis and under 45°. The maximum value of the transverse force is observed near 22°. Figure 2.3.4 shows the dependence of this force on the deviation angle for three different values of distance between the vortex and the pinning center. The calculation shows that the transverse force is maximal for elongations of order the coherence length ξ_0.

The dependence of the radial force on the distance from the pinning center is shown in Fig.2.3.5. This attractive force increases monotonically for distances smaller than the coherence length ξ_0. When the distance gets larger than ξ_0 the attraction weakens. The dependence of the radial force on the direction is so small than it seems unlikely to be observable.

Lines of Constant Potential
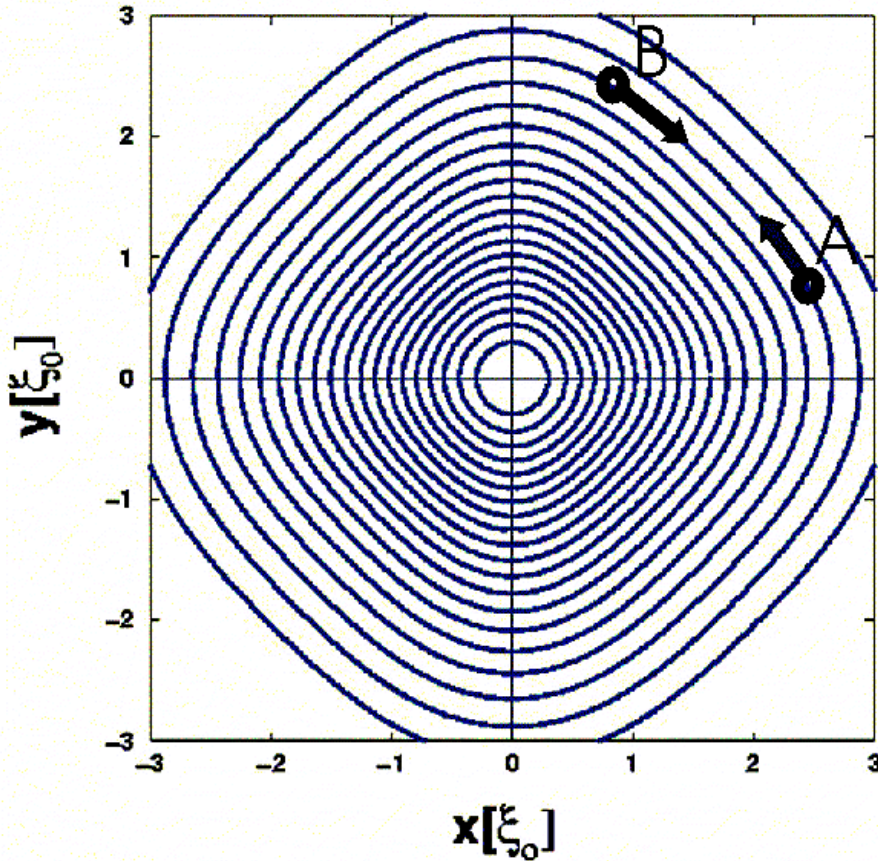
Figure 2.3.3. *The shape of the pinning potential. The equipotential lines have four-fold symmetry caused by symmetry of the order parameter. The arrows show the direction of the transverse forces acting on a vortex at points A and B. x and y denote the directions of the crystallographic axes in the basal plane. Displacement is shown in units of the coherence length ξ_0. The pinning center is located at (x, y) = (0, 0).*

To obtain the interaction between the flux line lattice and the superconductor it is necessary to summarize the elementary forces for a random set of pinning sites. The perfectly rigid and periodic flux line lattice can not be effectively pinned by the randomly distributed pinning sites. However, elasticity of the flux line lattice allows flux lines to deviate from the ideal periodic arrangement to lower their energy by better pinning but at the expense of increasing the elastic energy. This idea was developed as

the theory of collective pinning by Larkin and Ovchinnikov [27]. Unfortunately it is difficult to perform the exact summation of forces between randomly distributed pinning sites and the flux line lattice. But it is reasonable to assume that the symmetry of the elementary pinning force appears at sufficiently strong pinning and less rigid flux lines lattice.
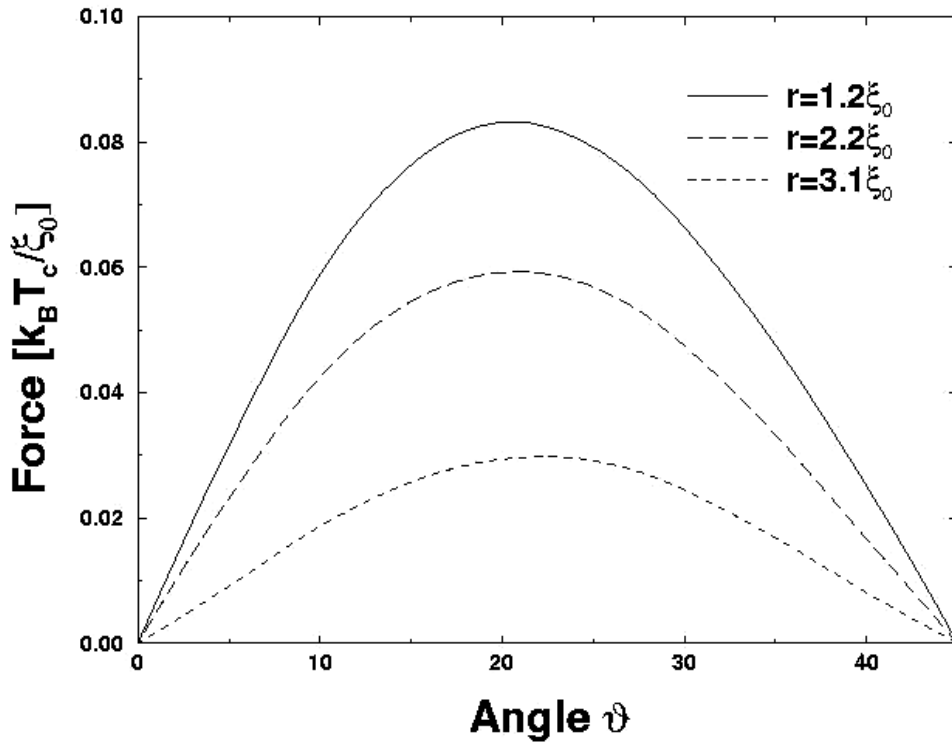
Figure 2.3.4. *The transverse force as function of magnitude and direction of the vortex displacement from the pinning site. The calculation shows that the maximal value is reached at an angle about 22° to the crystallographic axis and at a displacement of about the coherence length ξ_0.*
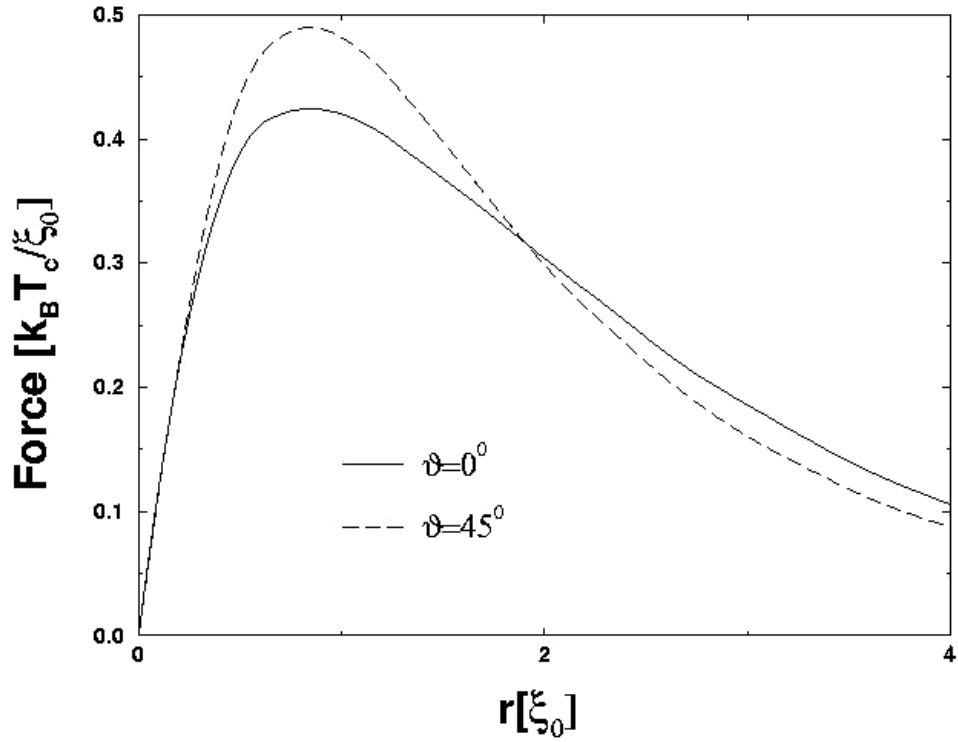
Figure 2.3.5. *The radial force as function of the displacement of the vortex from the pinning center. Displacement is shown in units of the coherence length ξ_0.*

2.4. Choosing the optimal conditions of experiment

From these considerations we can find requirements for the experimental measurement of the pinning potential symmetry. These measurements should be carried out at low temperatures far away from T_c to decrease the effect of the thermally activated flux flow and depinning. Also the magnetic field should not be too small since the total pinning force is proportional to the number of the vortices in the sample. However, since the elastic moduli C_{66} and C_{44} increase proportionally to the square of the magnetic field B^2, the magnetic field should not be too high.

The material of the superconductor is also very important for the experiment. $YBa_2Cu_3O_{7-\delta}$ is the first choice because this material is well studied and proven to be a d-wave material. Because of the interest in the symmetry of the point pinning the sample of $YBa_2Cu_3O_{7-\delta}$ should be an untwinned single crystal in which pinning is dominated by point-like oxygen defects. Samples of $Bi_2Sr_2CaCu_2O_{8+\delta}$ should even be better because of its more pronounced layered structure. This leads to smaller interaction between vortices in adjacent layers and to smaller elastic moduli of the flux line lattice.

Chapter 3

Vibrating reed technique

The vibrating reed technique has been known as a powerful tool to study Young's modulus, the sound velocity, and internal friction of different materials. It is interesting to use this method to study static and dynamic properties of the flux line lattice (FLL) in type II superconductors (see detailed reviews [8, 28]). The vibration of the superconductor in a static magnetic field between H_{c1} and H_{c2} leads to a measurable change in resonance frequency and damping of the reed because of the interaction between the FLL and the pinning centres. It appears to be a very useful method to study FLL properties and pinning forces, especially for the measurement of the Labusch parameter [29], the curvature of the average pinning potential. This method allows contact-free measurements of very tiny pieces of superconductor.

3.1. Standard experimental set-up

The standard experimental set-up of the vibrating reed consists of a platelet clamped at one end, while two electrodes near the free end serve to drive and to detect its motion electrostatically. The platelet might be the superconducting sample itself or a dielectric

host reed sputtered with a thin metal layer, with the superconducting sample fixed near its free end. At small amplitudes the reed behaves like a driven harmonic oscillator with natural frequency ω_0 and damping Γ

$$(\frac{\partial^2}{\partial t^2} + 2\Gamma\frac{\partial}{\partial t} + \omega_0^2)u_{reed} = \frac{F_0}{m^*}\cos\omega t \qquad [3.1]$$

where F_0 is proportional to the driving force, m^* is the effective reed mass and u_{reed} is the reed amplitude

$$u_{reed} = \frac{F_0}{m^*}\frac{1}{[(\omega_0^2 - \omega^2)^2 + 4\Gamma^2\omega^2]^{1/2}}. \qquad [3.2]$$

The two parameters of the vibration, resonance frequency ω_0 and damping Γ, are measured. Since the oscillation is excited by a constant driving force, the reed amplitude at resonance can be used to determine the magnitude of damping. But this is possible only in case of a constant gap between the reed and the driving/detecting electrode. Otherwise, the full resonance curve should be measured in order to determine the damping from the width of the resonance.

The application of a magnetic field causes an enhancement of the resonance frequency and an increase of the damping. For an understanding of the process it is important to remember that at such vibrations the superconductor is *tilted* in the magnetic field. A superconductor moving in a homogeneous magnetic field without rotation does not feel any force or torque. But the situation changes when the II type superconductor tilts in the magnetic field. For the magnetic field greater than a lower critical field B_{c1} the magnetic field penetrates in the superconductor in form of a periodic arrangement of the flux lines. Since the flux lines are pinned in the superconductor the tilt causes an increase of the magnetic energy and consequently additional restoring force acting on the reed. There were different experimental modifications with vibrating and rotating superconductor in a homogeneous field or linear oscillations in a nonhomogeneous field

[30 – 33]. But here we consider the behaviour of the superconducting sample glued to the vibrating reed, which oscillates in a homogeneous field.

Here we assume negligible magnetization of the superconductor which requires $\kappa>>1$, applied field $B_a>>B_{c1}$ so that the field penetrates completely the superconductor, i.e. $B_a = B$.

3.2. Line tension

The distortion of the magnetic field lines inside the tilted superconductor and around it causes an increase of the magnetic energy, which leads to a measurable additional restoring force. The value of this restoring force is proportional to the tilt modulus c_{44} of the flux line lattice in the reed and also to the magnetic energy needed to bend the outside field [34, 35]. Depending on the superconducting sample geometry and field direction these factors prevail in the mechanism of the increasing of the magnetic energy.

It is convenient to introduce here the line tension P (energy per unit length) to calculate the magnetic energy due to the curved field when the superconductor tilts in a homogeneous field. The resonance frequency enhancement is caused by the additional line tension

$$\omega^2(B) - \omega_0^2 \cong \frac{Pl}{I} \qquad [3.3]$$

where ω_0 is the resonance frequency in zero magnetic field, I denotes an effective moment of inertia of the reed, and l is the reed length. The additional line tension may be caused by different mechanisms: by tilt modulus of FLL, by energy of the curved magnetic field around the sample or by elastic coupling of the FLL to atomic lattice. The reed set-up configuration determines which mechanism prevails. In general we can

distinguish three types of line tension which correspond to three set-up configurations (shown in Fig.3.2.1.).
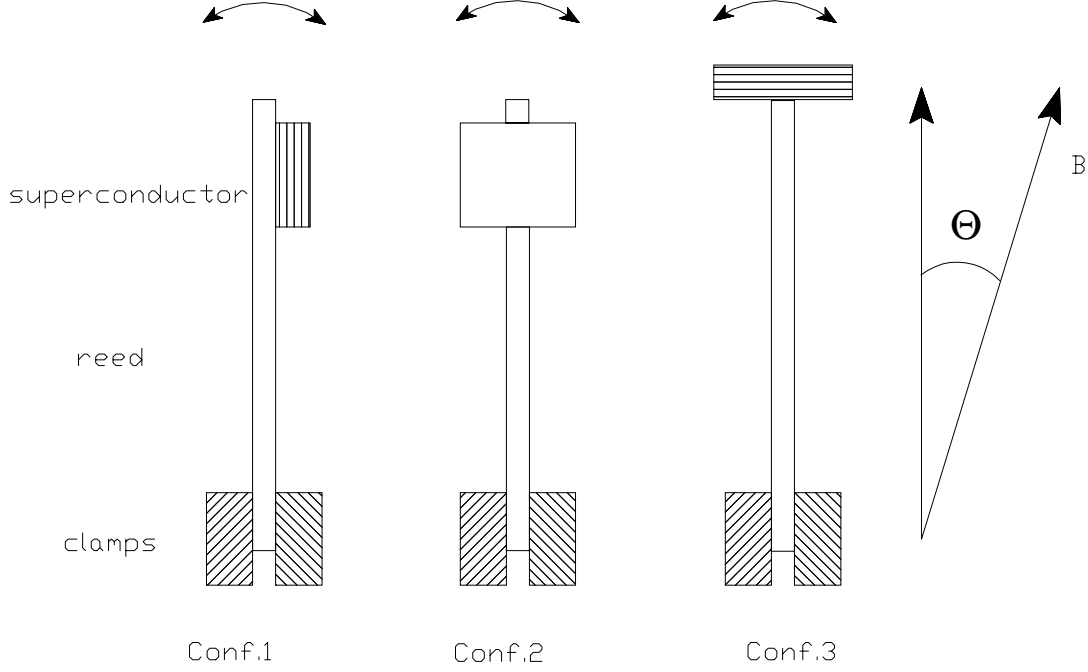
Figure 3.2.1. *Three different configurations of the vibrating set-up (taken from reference [36])*

The first case corresponds configuration 1, when the magnetic field is applied along the length of the sample with size $l_s \geq w_s >> d_s$ glued to the host reed (l, w, d). Then for rigidly pinned FLL or perfectly diamagnetic reed the line tension is mainly provided by energy of the distorted field and is given by [36]

$$P_1 = \left(\frac{\pi w_s^2}{4} \right) \frac{B_a^2}{\mu_0} \frac{l_s}{l} . \qquad [3.4]$$

This relation is valid if $\dfrac{l_s}{2} >> \left(\dfrac{\pi w_s}{4 d_s} \right) \lambda_{44}$ [37]. Here $\lambda_{44} = (c_{44}/\alpha)^{\frac{1}{2}}$ is the Campbell penetration depth for tilt waves. This parameter λ_{44} characterises how deep the small

oscillating disturbances of outer magnetic field penetrate in the superconductor [38, 39]. Thus, Campbell penetration depth determines the distortions of the flux lines inside the vibrating sample. In case if the penetration depth λ_{44} is smaller than the dimension of the sample along the field direction, the vortices are bent only in a thin surface layer. The value of λ_{44} is proportional to the FLL tilt modulus $c_{44} = BB_a/\mu_0$ and is inversely proportional to α, the Labusch parameter, i.e. the curvature of the average pinning potential $U(s, B, T, \Theta)$ for small displacement s of the FLL: $\alpha = \dfrac{\partial^2}{\partial s^2}[U(s, B, T, \Theta)]$.

The physical reason for appearance of the additional line tension P is the shielding of the small component δB perpendicular to the applied field when the reed is tilted by an angle ϕ.

The line tension P_1 is a factor $\pi w_s / 4 d_s \gg 1$ larger than the line tension

$$P'_1 = w_s d_s c_{44}(l_s / l) \qquad [3.5]$$

due to the FLL tilt modulus c_{44}, which is dominant in configuration 2 [36].

If the magnetic field is oriented perpendicular to the sample surface, i.e. along the thickness $d_s \gg 2\lambda_{44}$ ($\Theta = 90°$ in configuration 1), the line tension is mainly due to the FLL tilt modulus

$$P_2 = w_s l_s c_{44}(d_s / l). \qquad [3.6]$$

For arbitrary angle Θ the line tension is obtained by decomposing the magnetic field into components parallel to the length and thickness of the sample

$$P_{12} = P_1 \cos^2 \Theta + P_2 \sin^2 \Theta = \frac{\pi w_s^2 c_{44} l_s}{4l}\left(\cos^2 \Theta + \frac{4 d_s}{\pi w_s}\sin^2 \Theta\right). \qquad [3.7]$$
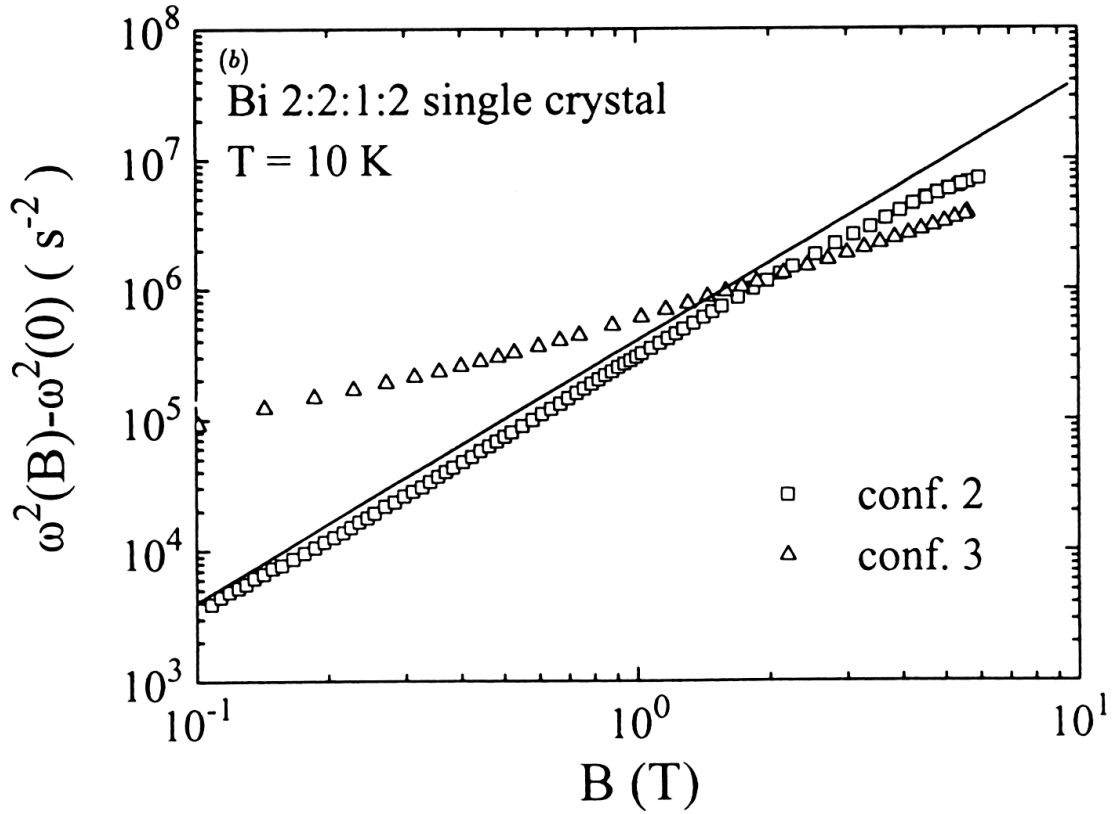
Figure 3.2.2. *Resonance frequency enhancement in magnetic field of single crystals of Bi₂Sr₂CaCu₂O₈₊δ. The measurements were done at T=10K. The continuous line is theoretically predicted dependence B² (Taken from reference [36])*

☐ *Bi₂Sr₂CaCu₂O₈₊δ in configuration 2;*

△ *Bi₂Sr₂CaCu₂O₈₊δ in configuration 3;*

The line tension is derived in the limit of infinite pinning. A relative movement between flux and the superconducting sample can be considered with appropriate corrections [37, 40]

In Fig.3.2.2 [36] the resonance frequency of $Bi_2Sr_2CaCu_2O_{8+\delta}$ in magnetic field is shown. The frequency change in configuration 2 is proportional to B^2 according to the theoretical equation [3.4]. The continuous line in figure is obtained with those equations showing that the theory describes well the measured $\omega^2(B)-\omega_0^2$ at the small magnet field in regime of strong pinning for the configuration 2.

3.3. Labusch parameter

The response of the superconductor is different when the penetration depth λ_{44} is larger than sample dimension along the field direction. In this case flux lines are pinned elastically and stay parallel to the external field. Therefore elastic pinning gives the main contribution to the magnetic energy and frequency enhancement. Thus, the line tension is provided mainly by the elastic coupling constant α, which characterizes the coupling between FLL and atomic lattice.

In configuration 3 or configuration 1 at $\Theta = 90°$ the line tension is then given by [36, 41]

$$P_3 = w_s l_s \alpha \frac{d_s^3}{3l} .$$ [3.8]

The result of the experiment with $Bi_2Sr_2CaCu_2O_{8+\delta}$ single crystal ($2.0 \times 0.9 \times 0.02$ mm^3) in configuration 3 is shown in Fig.3.2.2 at $T = 10$ K [36]. Here the dependence of frequency enhancement $\omega^2(B)-\omega_0^2$ was not proportional to B^2 as it was for configuration 2 because the thickness of the sample along the magnetic field is comparable to Campbell penetration depth λ_{44} and the field dependence of the frequency change is determined by the field dependence of the Labusch parameter. A similar result is obtained in configuration 1 as shown in Fig.3.3.1. The measurements were carried out with a $Bi_2Sr_2CaCu_2O_{8+\delta}$ single crystal ($1.8 \times 1.0 \times 0.025$ mm^3) at $T = 60$ K for angles $\Theta = 0 - 75°$ [36].
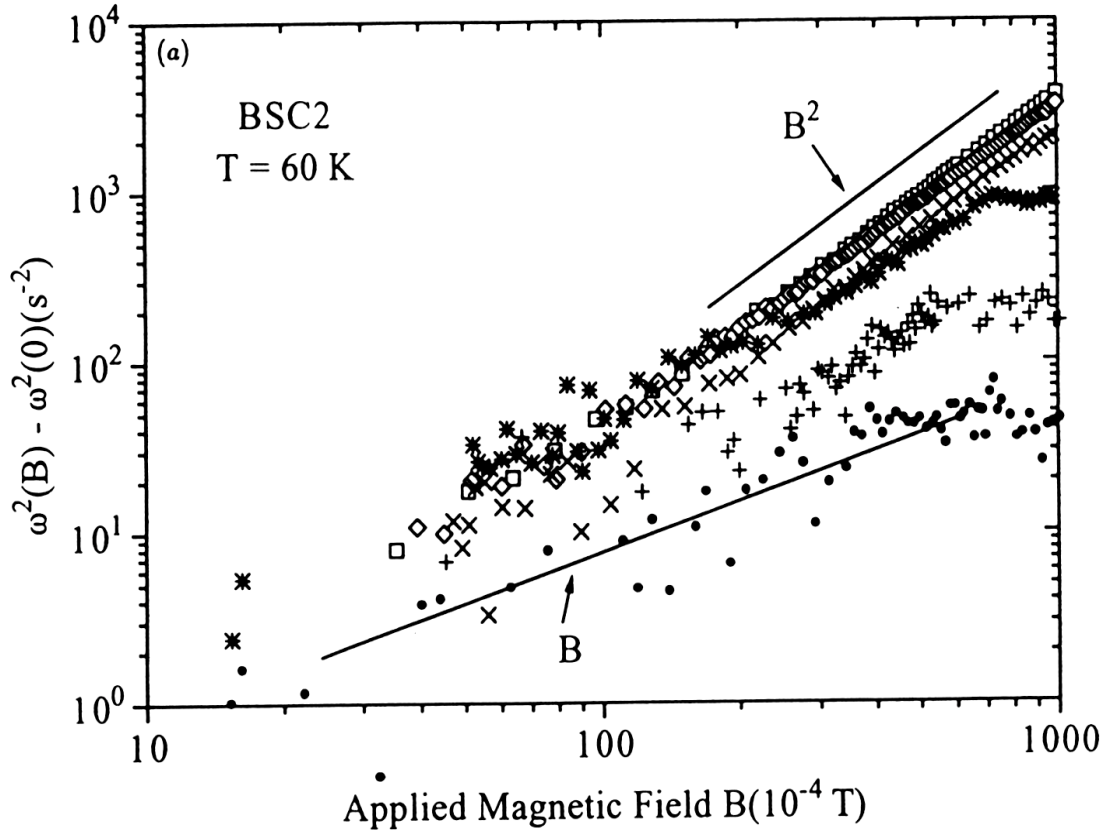
Figure 3.3.1. *Frequency enhancement as a function of the applied field for the Bi$_2$Sr$_2$CaCu$_2$O$_{8+\delta}$ crystal at T = 60 K and at different angles between field and CuO$_2$ planes (Taken from [36])* ● *- 75°;* ✚ *- 60°;* ✱ *- 45° ;* ✕ *- 30°;* ◇ *- 15°;* ☐ *- 0°*

For small angles the frequency enhancement $\Delta\omega^2$ is proportional to B^2 in agreement with theory, but for larger angles the slope of the curves is smaller and for $\Theta = 75°$ a linear field dependence is observed. This experiment might be interpreted as a crossover from a response due to distortion of the magnetic field at small angles $\Theta < 15°$ to a frequency enhancement due to elastic pinning α at $\Theta > 75°$.

Besides thin single crystals, reeds fabricated from granular suspensions are also used for direct measurements of the Labusch parameter [41, 42]. If the grain size $R < \lambda_{44}$ then the response of the reed is due to the elastic pinning. In this case the line tension is given by [41]

24

$$P_4 = wdf\alpha \frac{\langle R^5 \rangle}{5\langle R^3 \rangle}$$

[3.9]

where f is the volume fraction of grains in the reed and $<...>$ denotes the average over the particle size distribution. The frequency enhancement of $Bi_{1.5}Pb_{0.5}Sr_2CaCu_2O_8$ suspension and bulk reeds is shown at Fig.3.3.2 (taken from [42]). The estimation of the Campbell penetration depth λ_{44} gives value 129µm, i.e. larger than the grain size $<R> =$ 18.5 µm. Thus the result of these measurements is that α is proportional to $B^{1.9}$ in the field range 0.1 T $< B <$ 8 T, in agreement with results for polycrystalline reeds, which generally show $B^{2.0\pm0.2}$ proportionality.
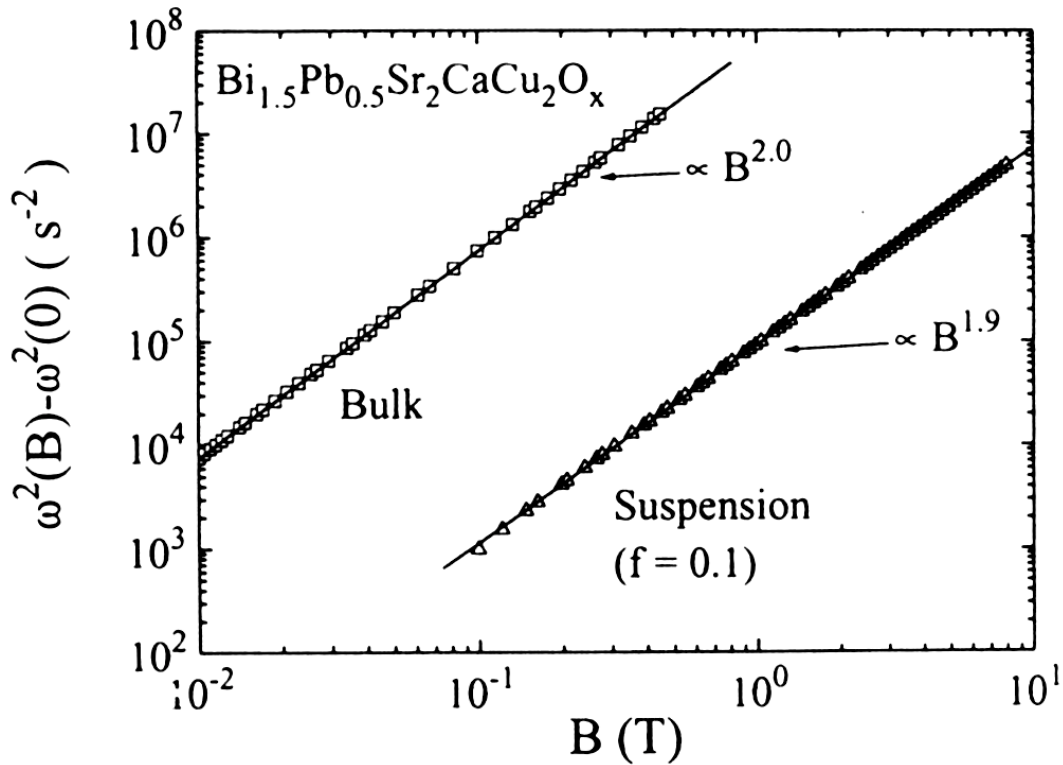
Figure 3.3.2. *Resonance frequency enhancement of a $Bi_{1.5}Pb_{0.5}Sr_2CaCu_2O_8$ suspension and bulk reed in configuration 1 at $\Theta = 0°$ and $T = 10K$. The solids lines are fits to the data of the form B^n with n = 2.0 (bulk) and n = 1.9 (suspension). (Taken from [42]).*

3.4. Thermally activated depinning

The ideal pinning picture considered in the previous case strictly spoken applies only at zero temperature. At T>0 thermally activated depinning of flux lines causes a non-vanishing resistivity. The important role of thermal depinning in high temperature superconductors was first pointed out by Dew-Hughes [43]. Thermal depinning, or "giant flux creep", occurs mainly because of the features which are peculiar to high-T_c superconductors. Small coherence length ξ and large magnetic penetration depth λ decrease elementary pinning energy and increase flexibility of the flux lines. Moreover, large material anisotropy leads to very low line tension of the vortices and thus FLs easily break into short segments or point pancake vortices which then depin individually with very low activation energy. The diffusive nature of the thermally activated flux motion caused by small flux density gradients was shown by Kes et al [44] introducing the thermally assisted flux flow (TAFF) model based on Anderson's ideas [45].

In the vibrating reed experiments the effect of thermal depinning was studied thoroughly since the method is very convenient for non-contact investigations of flux dynamics in HTSCs. The typical measurement of the resonance frequency change $\Delta\nu$ and damping Γ is shown in Fig.3.4.1 for an $YBa_2Cu_3O_{7-\delta}$ single crystal at $B = 2.8$ T and for three different vibration amplitudes [36]. Note that the vibrating superconductor response does not depend on the amplitude of vibration. It was found that the step in the resonance frequency and the accompanying damping maximum can be understood as a crossover from a pinned to an unpinned flux line lattice.
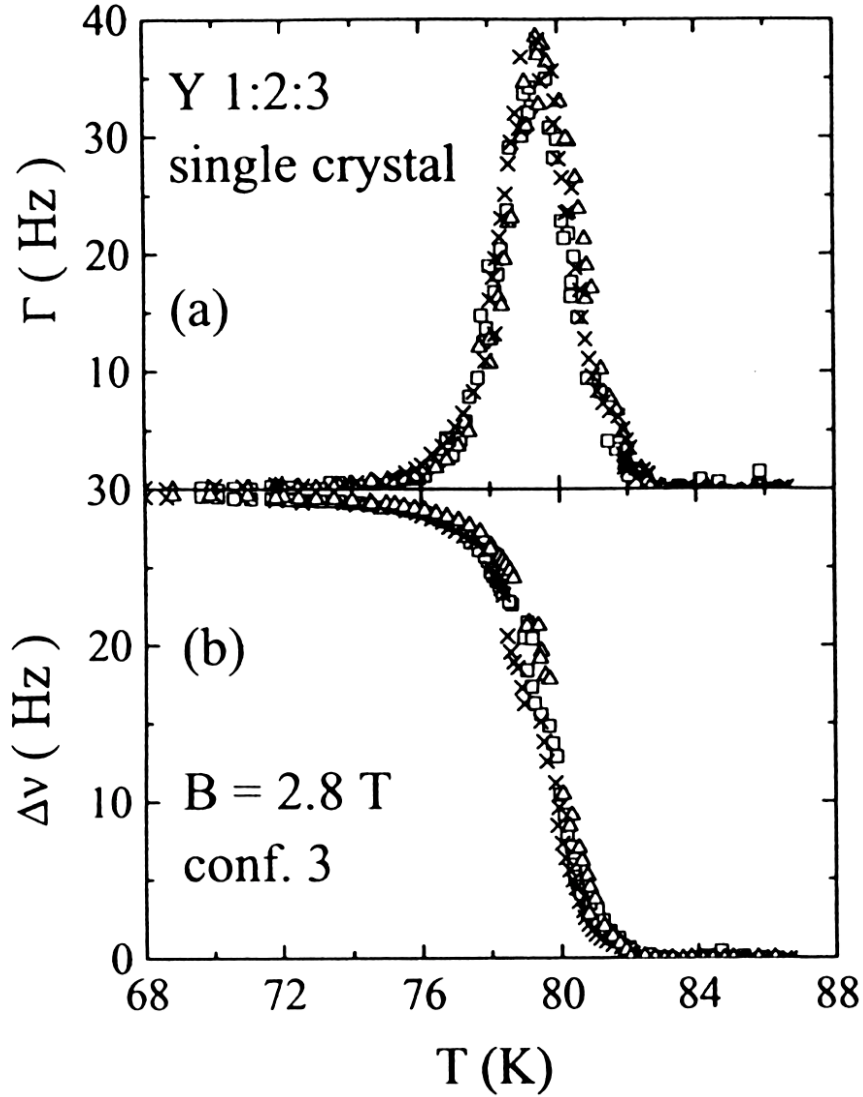
Figure 3.4.1. *Damping and frequency resonance enhancement of YBa$_2$Cu$_3$O$_{7-\delta}$ single crystal in an applied field B$_a$ =2.8 T at three different amplitudes A/A$_{min}$ = 1, 4, 8. Taken from [36].*

To understand this process let us consider the question how a moving superconductor with pinned flux line responds to a small field gradient ∇B. According to the Kim-Andersen model, in presence of a field gradient the vortices move by thermally activated hopping process in the direction of the Lorentz force

$$F_L = J \times B = -B\nabla B/\mu_0, \qquad [3.10]$$

Where J denotes the average current density. The expression for electric field caused by the flux jumps is given by Andersen and Kim [45]

$$E(J) = 2\rho_c J_c \exp\left(-\frac{U}{k_B T}\right)\sinh\left(\frac{JU}{J_c k_B T}\right) \qquad [3.11]$$

with the phenomenological parameters $J_c(B)$ (critical current density at $T = 0$), $\rho_c(B,T)$ (resistivity at $J = J_c$), and $U(B,T)$ (activation energy for flux jumps). The physical meaning of this expression is that the Lorentz force density $J \times B$ acting on the FLL increases the rate of thermally activated jumps of flux lines along the force, and reduces the jump rate for backward jumps.

The conservation of magnetic flux is expressed by a continuity equation [46]

$$\frac{\partial B}{\partial t} = -\nabla \cdot \mathbf{J}_\Phi \qquad [3.12]$$

with the vortex current density $\mathbf{J}_\Phi = -uB(\nabla B / |\nabla B|)$ where u is flux motion velocity

$$u = u_0 \exp\left(-\frac{U}{k_B T}\right)\sinh\left(\frac{JU}{J_c k_B T}\right). \qquad [3.13]$$

At low current densities $J << (kT/U)J_c$ the vortex velocity is linear in the current density [43]. Linearizing the continuity equation for a small perturbation B leads to a diffusion equation [44, 47, 48]

$$\frac{\partial B}{\partial t} = D\nabla^2 B \qquad [3.14]$$

with a diffusion constant

$$D = \frac{v_0 B_a}{\mu_0 J_c}\frac{U}{kT}\exp\left(-\frac{U}{kT}\right). \qquad [3.15]$$

The depinning of the flux lines will increase the energy loss, i.e. the damping of the reed oscillation, and will reduce the resonance frequency since there is no additional line tension caused by field shielding or tilting of the vortices. The resonance frequency reduces to its zero field value when all flux lines are parallel to the external field. This happens when the tilt of the flux lines (i.e. the small field perturbation δB_{ac}) diffuses to the center of the reed. The time scale for thermally activated depinning is

$$\tau \cong \frac{\eta}{\alpha}\exp\left(\frac{U}{kT}\right), \qquad\qquad [3.16]$$

where η is the viscosity of the flux lines. The penetration length for AC deviation λ_{AC} is given by [49, 50]

$$\lambda_{AC}^2 = \lambda^2 + \frac{B^{'2}}{\mu_0}\left(\frac{\alpha}{1-i/\omega\tau}+i\omega\eta\right)^{-1}. \qquad\qquad [3.17]$$

The schematic picture describing the depinning transition is shown in Fig.3.4.2 (taken from [51]). At frequencies $\omega \gg \tau^{-1}$ the effective AC field, generated by tilting of the superconductor in the DC magnetic field, is shielded leading to a resonance frequency enhancement, as described in the previous part. At $\omega \approx \tau^{-1}$ flux lines tilt penetrate to the sample centre and the maximum in damping (energy losses) is observed. At $\omega \ll \tau^{-1}$ the deformation of the flux lines diffuses through the sample thus the lines are always parallel to the direction of the applied field. Therefore, there is no FLL contribution to the line tension and no frequency enhancement.
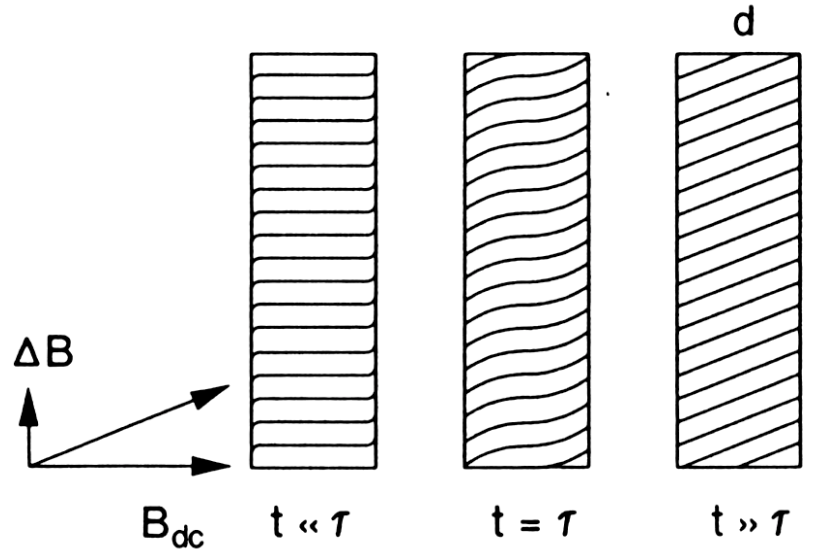
Figure 3.4.2. *Schematic picture of diffusive flux penetration into a superconductor (taken from [51]). A static magnetic field B_{dc} is applied parallel to the thickness of the superconducting sample. At t = 0 a small field ΔB is applied perpendicular to B_{dc}. This field perturbation diffuses into the superconductor on a characteristic time scale τ. For t « τ, ΔB is shielded at the surface leaving the field orientation inside the superconductor parallel to B_{dc}, for t = τ the perturbation has penetrated to the centre of the sample and for t » τ the field inside the superconductor has become parallel to the applied field.*

3.5. Double peaks in dissipation of the superconductors

In several publications dealing with vibrating superconductors [52; 53] and superconductors in ac-field [54, 55] an interesting effect was reported. Two distinct peaks in the dissipation as function of the temperature were observed when the DC component of the applied field was directed under some non-zero angle to the symmetry axis of the sample. When the field was applied along the axis one of the peaks disappeared.

As it was explained in [51], this effect can have geometrical origin and relates to the diffusion of the field perturbation by thermally activated flux depinning. The different relaxation times τ, i.e. penetration times for field perturbation, lead to different modes of the flux lines diffusion. So the relaxation time along the thickness is $\tau_d = \dfrac{d^2}{\pi^2 D}$ and along the length is $\tau_l = \dfrac{l^2 d}{w \pi^2 D}$. If the field is directed along x, y or z axis, a single diffusion mode is exited and only one peak observed. The situation with oblique field is different as shown in Fig.3.5.1. In a first relaxation mode the flux line tilt diffuses across the slab thickness, then in second slower mode along the length.

$$\Gamma = \left(\frac{B^2 V_s}{2\mu_0} \right) \left(\left(\frac{\chi_d'' \sin^2 \Theta}{2I\omega} \right) + \left(\frac{\pi w_s}{4 d_s} \frac{\chi_l'' \cos^2 \Theta}{2I\omega} \right) \right). \qquad [3.18]$$

So the damping can be calculated using equation [3.18], where V_s is the sample volume and χ_d'' and χ_l'' are the imaginary (absorption) part of the complex AC susceptibility for two different modes

The experimental results [56] demonstrated very good agreement with this equation as shown in Fig.3.5.2. The measurements of the damping of single crystal $YBa_2Cu_3O_{7-\delta}$ were carried out in a field $B_a = 0.7$ T at different angles. At $\Theta = 60°$ a double peak structure is clearly visible and at $\Theta = 30°$ the maximum corresponding mode along d appears as a shoulder on the low-temperature side of the peak. The solid curves are calculated according to equation [3.18].
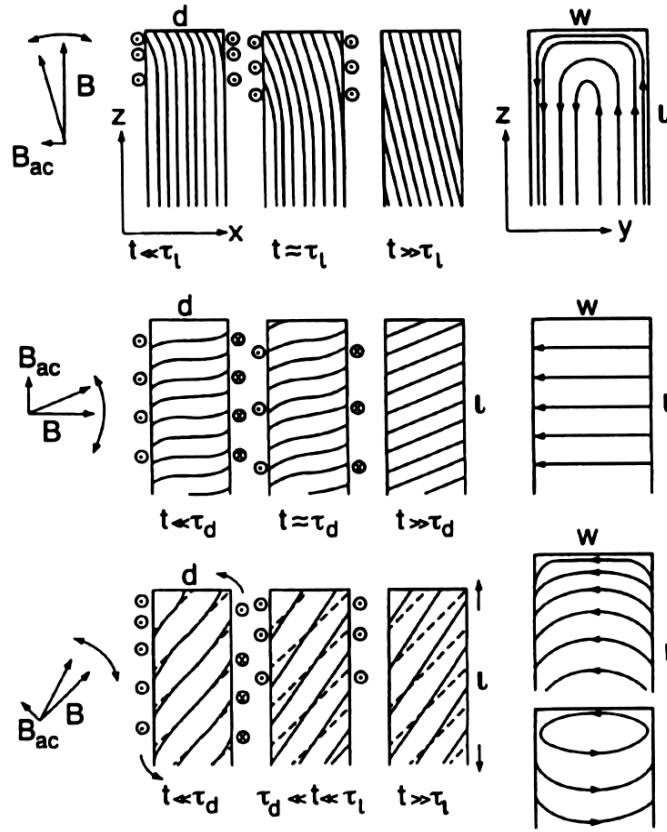
Figure 3.5.1. *Visualization of relaxation modes in superconducting sample in tilting magnetic field. The shielding currents which appear on the surface of the sample immediately after field tilting are shown as circles with dots and crosses. At the right picture the current patterns are shown. Top picture: B||z, longitudinal mode. The flux line tilt diffuses from the top end of the slab along the length in a time* $\tau_l = \dfrac{l^2 d}{w\pi^2 D}$.

Middle picture: B||x, perpendicular mode. The flux lines across the sample curve and straighten in a time $\tau_d = \dfrac{d^2}{\pi^2 D}$. *Bottom picture: B tilted by an angle* Θ. *In a first mode the field perturbation diffuse across slab thickness to realign the fluxes along field B. This leads to increased flux density, which has to expand in a second slower mode along z. Taken from [51]*
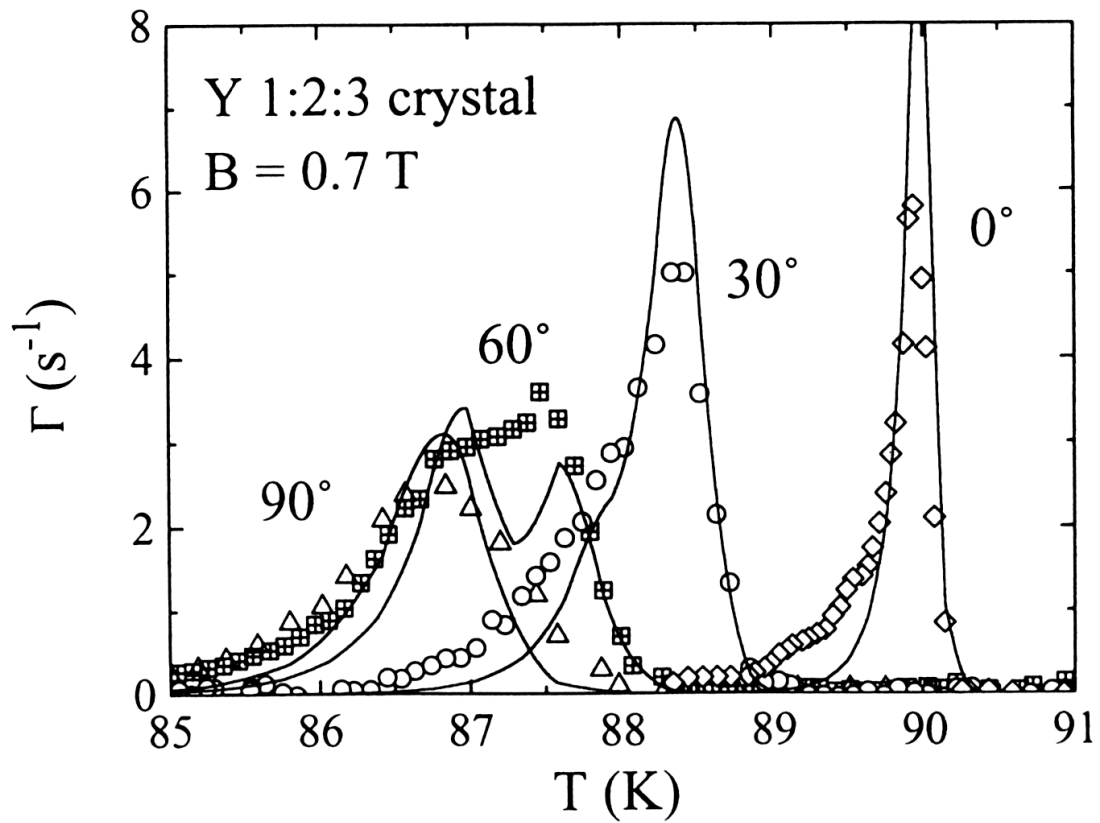
Figure 3.5.2. *Damping of YBa$_2$Cu$_3$O$_{7-\delta}$ single crystal at B$_a$ = 0.7 T. The continuous lines represent fits to the flux diffusion theory (taken from [56]).*

Chapter 4

Description of the experiment

4.1. Two-dimensional vibrating reed

4.1.1. The mechanical oscillator

The main part of the two-dimensional vibrating reed is a sapphire fiber (diameter 100μm, Good Fellows) glued into the hole at the center of a ruby disk – a jewel stone of old watches (Fig.4.1.1). The materials were chosen because of special requirements to the reed. It should be dielectric to prevent eddy currents in magnetic field. The material of the reed also should have very good thermal conductivity since the diameter of the wire is rather small. The dielectric crystals are ideal for this. Also crystal sapphire has good mechanical properties so the reed has rather high quality factor (up to 50 000) at frequency 400 – 800 Hz. The dielectric reed is covered by a thin conducting layer of evaporated gold or silver for driving the reed electrostatically and detecting its elongation from equilibrium by capacitance method.
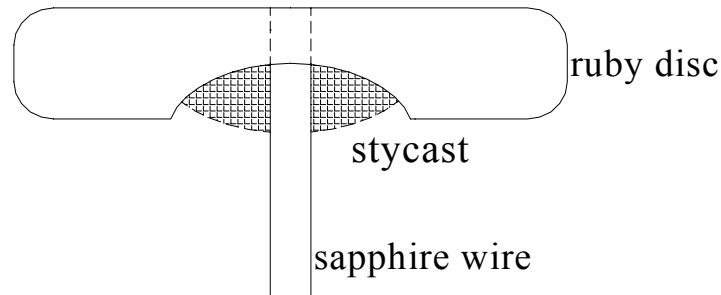
Figure 4.1.1. *The sapphire wire glued into the hole of the ruby disc (watches jewel stone) with Stycast. The diameter of the hole is about 120÷140 µm, the wire diameter is 100 µm, and the wire length is about 7 mm.*

4.1.2. The cell

Figure 4.1.2 shows the scheme of the vibrating reed cell for measurements of the superconducting sample (1), glued on the top of the reed (2). The other end of the reed is glued with Stycast into a thin copper capillary (3) which is clamped by copper blocks (4). Two orthogonal electrodes-screws (6) are fixed in plastic isolators (7) to isolate them electrically from the copper reed holder. The gap between electrode and the reed can be adjusted by screwing the electrode in and out. In the experiment this distance is usually about 10µm.

On the clamped end of the reed the small screw head (5) is glued. It allows adjustment to find the principal axes of inertia of the reed. It is shown in the Appendix B that this is always possible for such a mechanical oscillator with two degrees of freedom. Indeed when the detection coordinates coincide with the easy axes of the reed, the oscillation decouples to two independent oscillations along the axes. In other cases we have a system of two coupled oscillators, and the resonance curve will have two peaks. In such a system the free oscillations will have beating. Another feature of such a system with

two degrees of freedom is that applying a driving force at one electrode will result in a signal at both detectors, and the free reed end will move on an elliptical trajectory. Thus the easiest way to find the main axes of the inertia of the reed in the experiment is the use of two criteria. The first is absence of beating at free oscillation of the reed. The second criterion is the absence of the signal on one detecting electrode when the drive is applied along the other.

The two modes of oscillation have slightly different frequencies because the elastic properties of the sapphire wire are anisotropic and the shape of the reed is not absolutely symmetrical. Usually this intrinsic difference between frequencies ω_x and ω_y is about 5-8Hz. Since the width of the resonance curves is about 0.05Hz such a distance between resonance frequencies is too large for the excitation of oscillations at both directions. To reduce this distance the additional weight made of plastic mass was attached on the top of the ruby disc. This plastic weight is soft at room temperatures. That makes it convenient for adjustment. At low temperatures plastic mass hardens and allows long measurements without detuning. This additional plastic weight has oblong shape and allows making difference between mode frequencies 0.5-1Hz
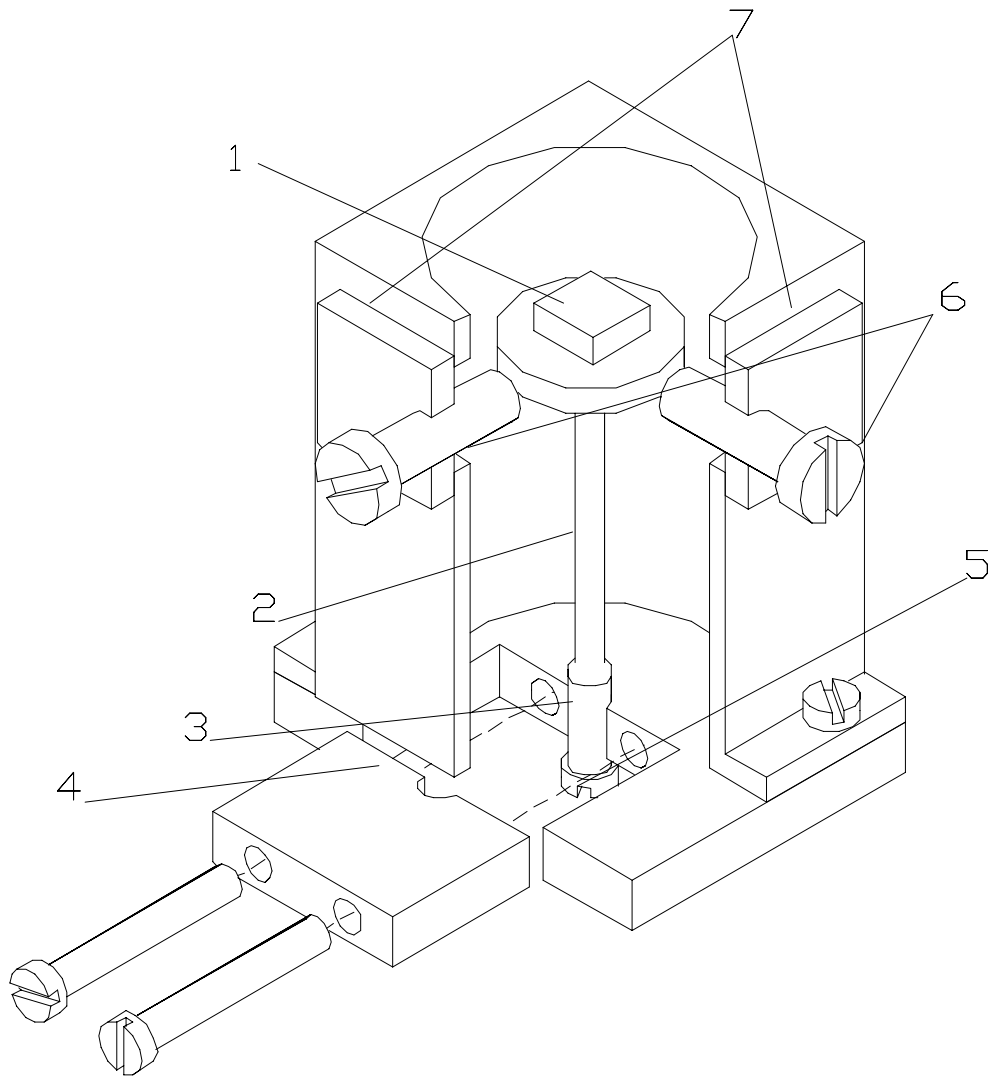
Figure 4.1.2. *Two-dimensional vibrating reed.*

1. Superconducting sample, $YBa_2Cu_3O_{7-\delta}$

2. The vibrating reed: sapphire wire, diameter 100μm, length about 7mm, glued into the centre of the ruby disc

3. Copper capillary, inner diameter 0.2mm, outer diameter 0.5mm

4. Copper clamp

5. Adjusting screw head

6. Electrodes, screws

7. Dielectric electrode holders, textolite

4.1.3. The measurement technique

The deviation of the reed from its equilibrium position is measured by the electrodes by a capacitance method. The change of the capacitance between the electrode and reed causes the modulation of the high frequency of the LC-generator with 100 MHz base frequency (see diagram 4.1.3.). The high-frequency signal is demodulated in the tuner and the demodulated signal fed into the lock-in amplifier and the oscilloscope.
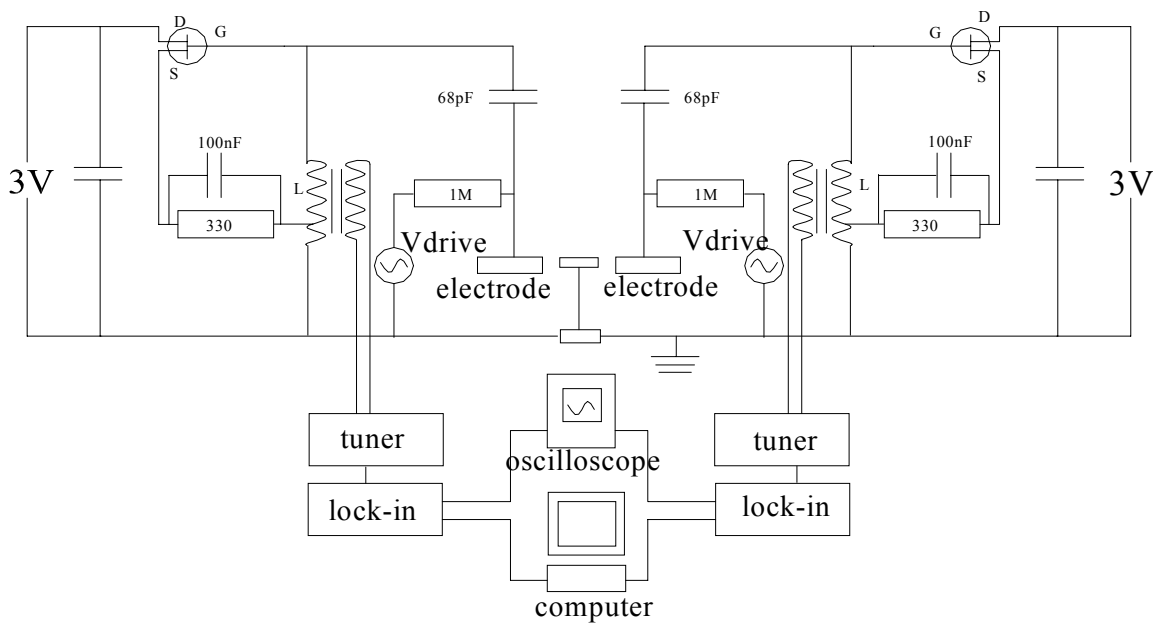
Figure 4.1.3. Diagram *of the LC-generators. The frequencies are about 100MHz and 90MHz.*

The same electrodes which are used for detecting also excite the motion of the reed by applying an AC voltage from driving voltage supply ELUB643 (Electronic Laboratory of Uni-Bayreuth) with changeable phase difference between two outputs (diag.4.1.4). The frequency synchronization was realized either from the output of synthesized frequency generator (Stanford Research System, model DS 340) or by output from the

lock-in amplifier. In the latter case we have the auto-generation cycle locked on the frequency of the reed resonance.
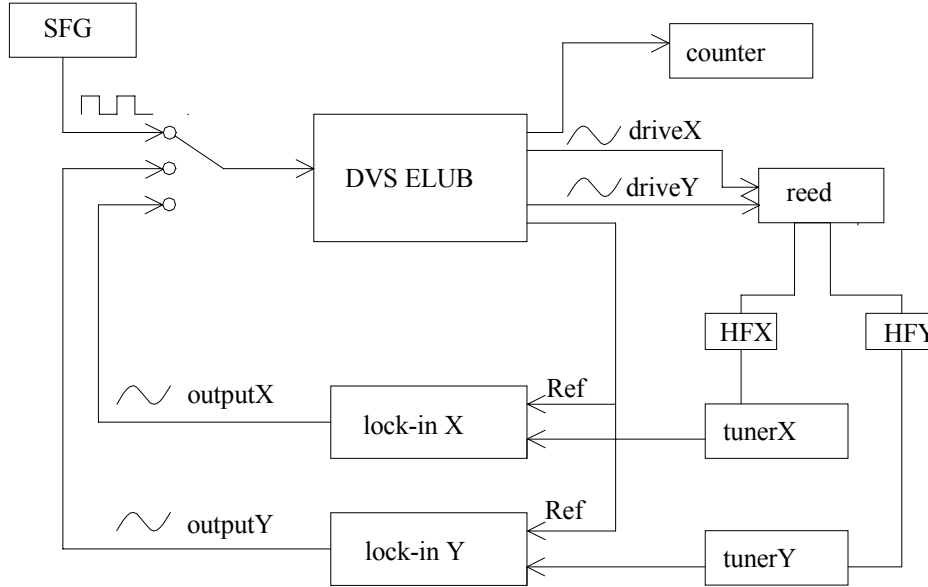
Figure 4.1.4. *Diagram of the measurements. DVS ELUB – driving voltage supply; SFG – synthesized function generator; HFX and HFY – high-frequency LC-generators.*

4.1.4. The normalisation of the measured values

For the experiment it is important to know the relation between the real amplitudes of oscillation along *x* and *y* directions. If we assume that the effective surface area of the measuring/detecting capacitors is the same for both electrodes, we do not need to know exact value of the gap between electrodes and the reed. The driving force F_{drivve} is proportional to square of driving voltage φ^2: $F_{drive} = \dfrac{\varphi^2 C}{d}$, where *d* is the distance between electrode and reed, and *C* is the capacitance of the reed/electrode capacitor. The oscillation amplitude in resonance can be found from the equation of motion of the reed

$$a = \frac{F_{drive}}{2m^*\Gamma\omega} = \frac{1}{2m^*\Gamma\omega}\frac{\varphi^2 C}{d} . \qquad [4.1]$$

The reed vibration leads to an oscillation of the capacitance with amplitude

$$\Delta C = C\frac{a}{d} = \frac{1}{2m^*\Gamma\omega}\frac{\varphi^2 C^2}{d^2} . \qquad [4.2]$$

The change of the capacitance is modulating the frequency of the HF oscillator and it results in voltage signal V_{signal} measured by the lock-in amplifier. This signal can be calibrated if we know the tuner coefficient K: $\Delta C = V_{signal}/K$. Thus knowing the value of signal in resonance it is possible to find the only unknown value C/d:

$$\frac{C}{d} = \sqrt{\frac{2m^*\Gamma\omega}{K}\frac{V_{signal}}{\varphi^2}} . \qquad [4.3]$$

From here the amplitude of the reed oscillations can be found

$$a = d\frac{\Delta C}{C} = \frac{V_{signal}d}{KC} = \sqrt{\frac{\varphi^2 V_{signal}}{2m^*\Gamma\omega K}} . \qquad [4.4]$$

It is reasonable to assume that for the x and y coordinates the value $2m^*\Gamma\omega K$ is the same. Thus the amplitudes can be normalized by knowing that

$$\frac{a_x}{\varphi_x\sqrt{V_{signal}^x}} = \frac{a_y}{\varphi_y\sqrt{V_{signal}^y}} = const . \qquad [4.5]$$

Thus for the same driving voltage the resonance amplitudes relate as the square root of signal voltage

$$\frac{a_x}{a_y} = \sqrt{\frac{V_{signal}^x}{V_{signal}^y}}\Bigg|_{\varphi_x=\varphi_y} \qquad [4.6]$$

and this relation gives the normalization coefficient for the real amplitudes of oscillation along different axes.

4.2. Detwinning of the YBCO crystal

In the experiment we used YBa$_2$Cu$_3$O$_{7-\delta}$ crystals grown by Peter Fischer and Wolfgang Widder in our laboratory. The growth method is described in detail in the dissertation [57]. The results of the magnetisation study of the samples are also demonstrated there and will be shown in part 4.5.

The superconducting YBa$_2$Cu$_3$O$_{7-\delta}$ presents a typical example of a ferroelastic crystal with a highly twinned domain structure, made up of lamellar domains with a high density of twin walls [58] (see Fig.4.2.1). These domains can be easily seen under the polarising microscope [59, 60]. Since twin boundaries can be strong longitudinal pinning centres [61, 62] it was reasonable to reduce their effect by detwinning.
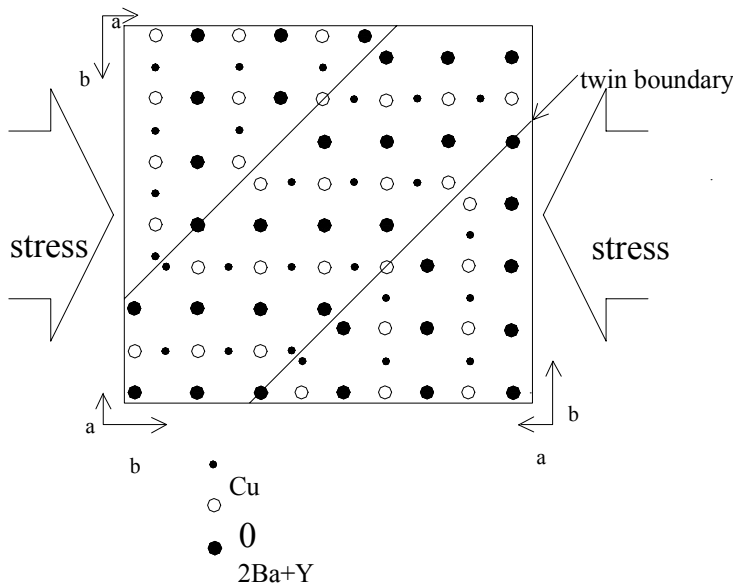
Figure 4.2.1. *Scheme of twin boundaries and the detwinning by stress.*

In order to obtain a large single domain for the vibrating experiment the usual stress technique was used [63-66]. Uniaxial stress was applied by the spring detwinning device constructed shown in Fig.4.2.2. The process of detwinning took place at temperature about 400-500°C, not exceeding 550°C to prevent deoxidising of the sample. For the same reason the crystal was all the time kept in an oxygen flow. The spring with k=2.18N/mm was steadily compressed for 3-4mm after heating the sample. This allows smoothly pressing the sample up to 25MPa by soft slightly melted glass without breaking the crystal. The detwinning usually takes about 5-10 hours. After this process the temperature was slowly decreased and pressure was steadily removed. As result we can observe the domain free surface of crystal under the polarising microscope. Unfortunately, it is possible to be certain about the absence of domains only on the crystal surfaces. But nevertheless it is a strong indication that we have a domain free crystal.
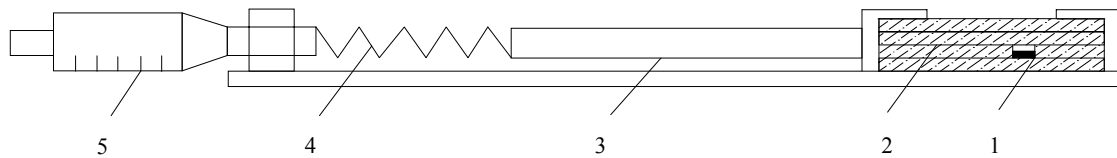
Figure 4.2.2. *Schematic picture of the device for detwinning of YBCO crystal.*

1. YBCO crystal

2. Glass plates

3. Glass rod

4. Spring with the elastic coefficient k = 2,18 N/mm

5. Micrometer screw

4.3. Oxidation of the YBCO crystal

The crystals of $YBa_2Cu_3O_{7-\delta}$ as obtained have superconducting transitions at 60 K. This indicates that the crystals are in the oxygen deficiency phase (δ is 0.2–0.4) [67-70]. It is known that oxygen vacancies often form one-dimensional structures, kind of chains [71-75], which can act as longitudinal pinning centres. Thus it is reasonable to convert 60K $YBa_2Cu_3O_{7-\delta}$ into oxygen saturated 90K $YBa_2Cu_3O_{7-\delta}$. Oxygenating requires long time, high temperature and high pressure because of the small diffusion coefficient of oxygen in the crystal. But the temperature should not exceed 600°C, the temperature of an orthorhombic-to-tetragonal phase transition in $YBa_2Cu_3O_{7-\delta}$ [70, 76 - 79].

The samples in the alumina crucible were placed into the device shown in Fig.4.3.1. The oxygen pressure in the device was about 200bar when the temperature was about 500°C. The chart of the temperature change is shown in Fig.4.3.2. First the temperature was increased rather fast (120°C/h) to 460°C. Then after several minutes of stabilisation it was increased steadily with rate about 50°/C. This stage allows reaching accurately the temperature 500°C without overheating. The inner cavity was filled by oxygen at room temperature to a pressure of 150bar. At high temperature the pressure reached 200bar. After a week of oxidation the temperature was decreased very slowly.
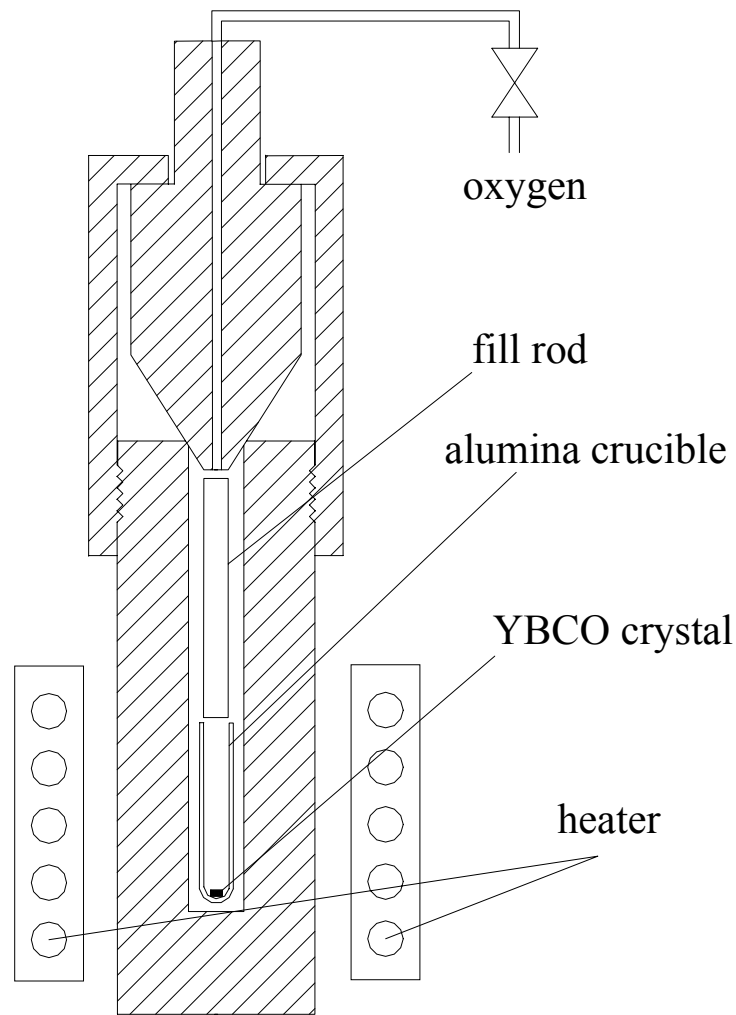
Pic.4.3.1. *Set-up for oxidising. The oxygen is under the pressure 200bar from the pressure gas cylinder.*

The oxidised samples showed $T_c=80\div90K$ as usual for saturated $YBa_2Cu_3O_{7-\delta}$. But these samples break more easily at detwinning than the crystals before the process. It is possible that oxidation results in crystal tension which increases the fragility of crystals. So it is reasonable to detwin the samples before oxidising. Fortunately the examination under the polarising microscope shows that oxidising does not affect the number of twin domains. Samples treated in this way have T_c about 80K and no visible traces of twins.
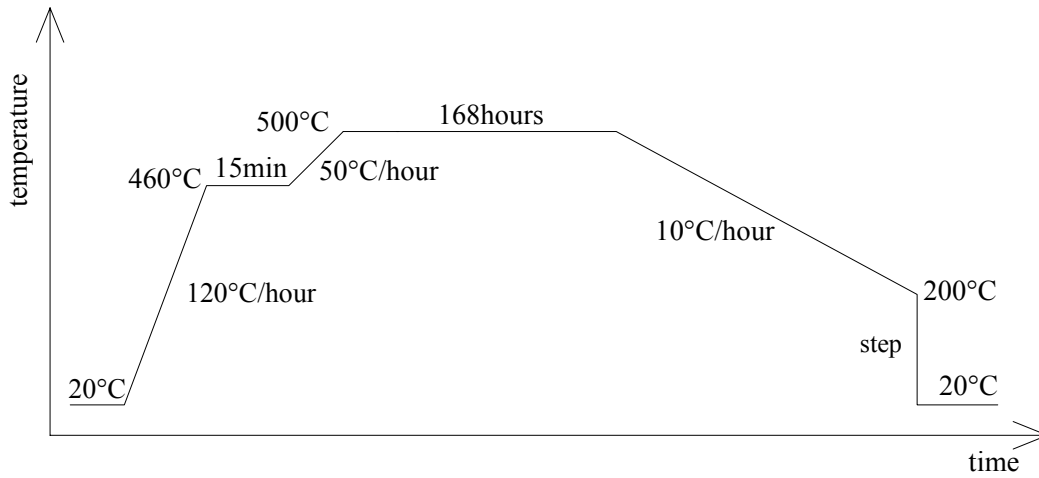
Pic.4.3.2. *Chart of the temperature program during oxidising. Fast heating, one week at high temperature and high pressure, then very slow cooling.*

4.4. Magnetic ac-susceptibility measurements

For the AC susceptibility measurements we used a conventional method [80, 81]. The set-up (shown in Fig.4.4.1.) consists of one primary coil, one secondary coil, in which a superconducting sample is placed, and another secondary reference coil. An AC current I_p can be put through the outer primary coil, thus creating a small AC field, which induces AC voltages in the secondary coils. The difference between the voltages induced in the secondary coils U_s is proportional to the complex ac-susceptibility of the sample $\chi_{ac} = \chi'_{ac} - i\chi''_{ac}$:

$$U_s = -ig\nu V_p h_0 \chi_{ac}.$$ [4.7]

Here V_p is volume of the sample, h_0 is amplitude of the oscillating field, and ν is the frequency. The coil coefficient g is proportional to the mutual inductance of the coils and can be determined by measurement of a sample with known susceptibility.
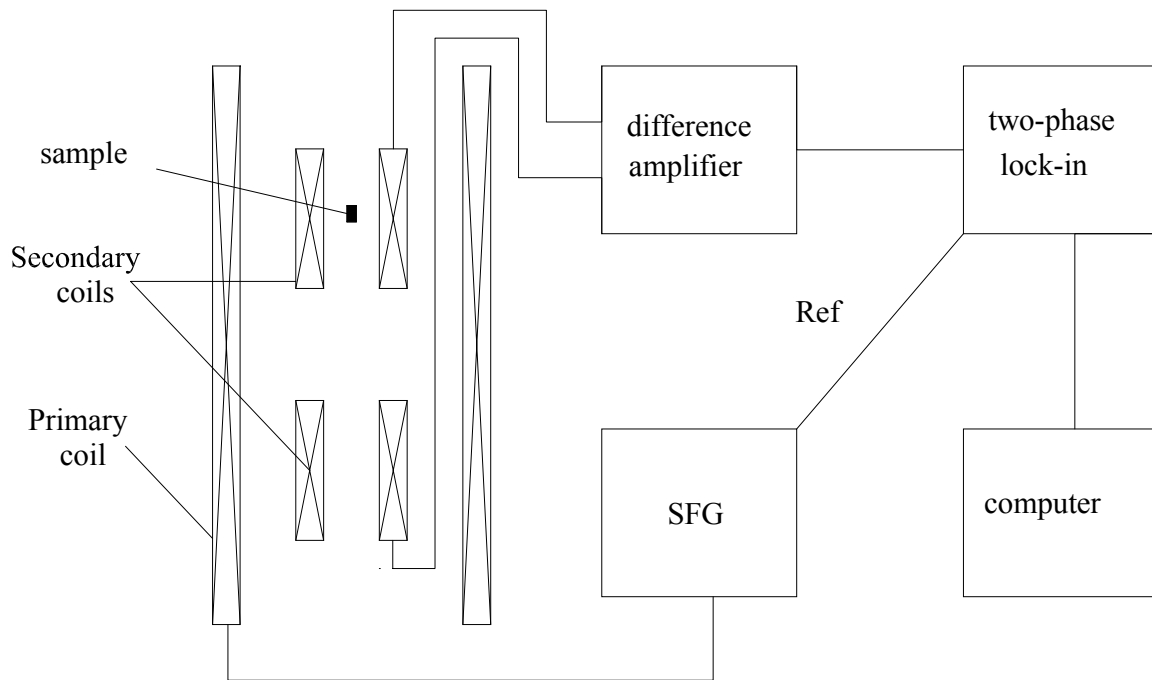
Figure 4.4.1. *Diagram for measurements of ac-susceptibility. SFG – synthesized function generator.*

4.5. SQUID-magnetometry

As mentioned above the studied $YBa_2Cu_3O_{7-\delta}$ crystals were grown by Peter Fischer and Wolfgang Widder. Also the measurements of magnetic properties were carried out with those samples by Peter Fischer. The magnetisation was measured by SQUID (Superconducting Quantum Interference Device) magnetometer set-up MPMS (Magnetic Properties Measurement System) of Quantum Design (San Diego, USA). The sample was placed in the cryostat equipped with superconducting magnet with maximal field 5.5 T.

The measurements were carried out with single crystal ($2 \times 2 \times 1$ mm^3) at temperatures 10, 40 and 77K with applied DC field B along the c-axis and perpendicular to the axis to study the anisotropy of the crystal magnetic properties. Relevant to our case experiment

with $B||c$ demonstrates hysteretic loops in increasing and decreasing magnetic field (see Fig.4.5.1).
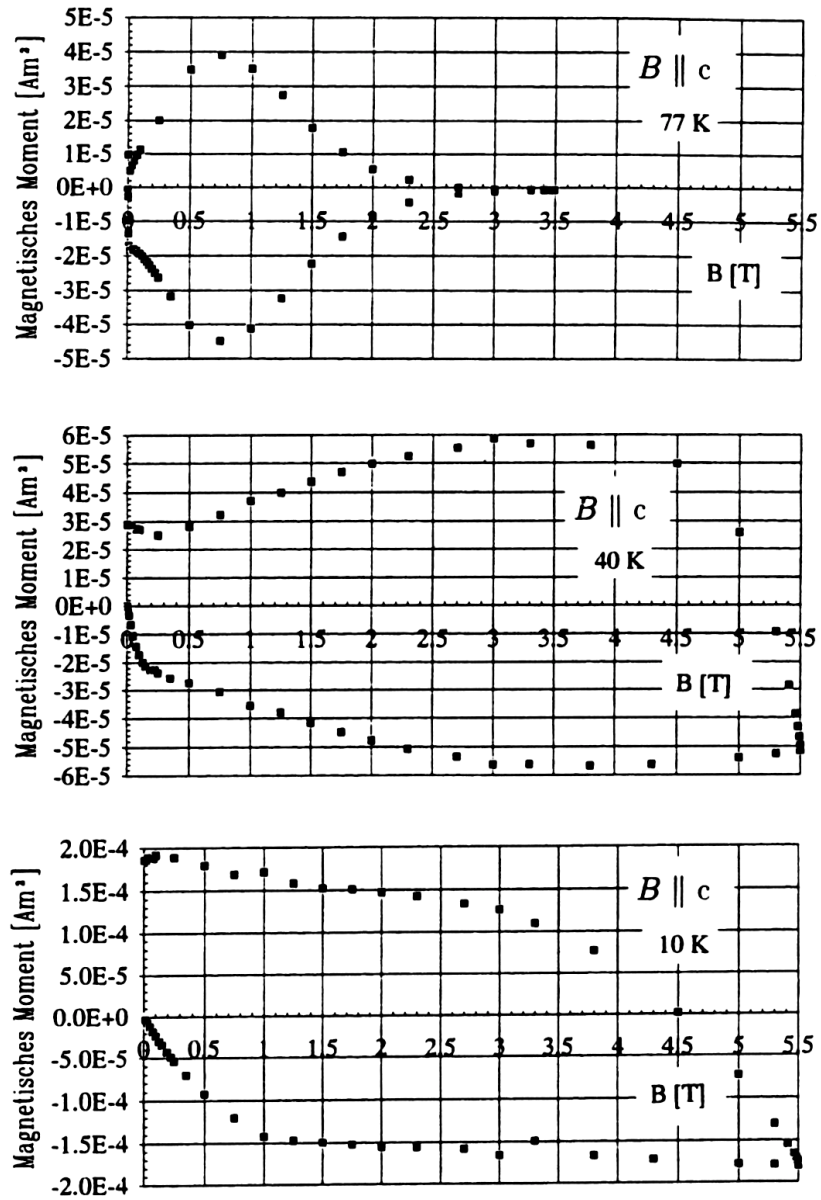
Figure.4.5.1. *Magnetisation of the single crystal (B||c) at temperatures 77, 40 and 10K. Increasing of the field yields the lower curve, decreasing of the field back to zero gives upper line of the hysteresis curve. Taken from ref. [57].*

4.6. Cryostat

The vibrating reed measurements took place in a cryostat equipped with a 9T superconducting magnet. The bore of the magnet is 43mm. The magnet power supply (Heinzinger TNSUs 5-100) allows a maximum current I_{max}=100A and a maximum voltage U_{max}=5V. The stability of the magnet current is about 10^{-5}.

The liquid helium volume of the cryostat is about 30 l and rate of the evaporation is about 0.5-1 l/h. So the stand time is about 30 hours. However, the working with the magnet is possible only when the level is high enough, i.e. only in the first 10-15 hours. A schematic picture of the cryostat is shown in Fig.4.6.1.
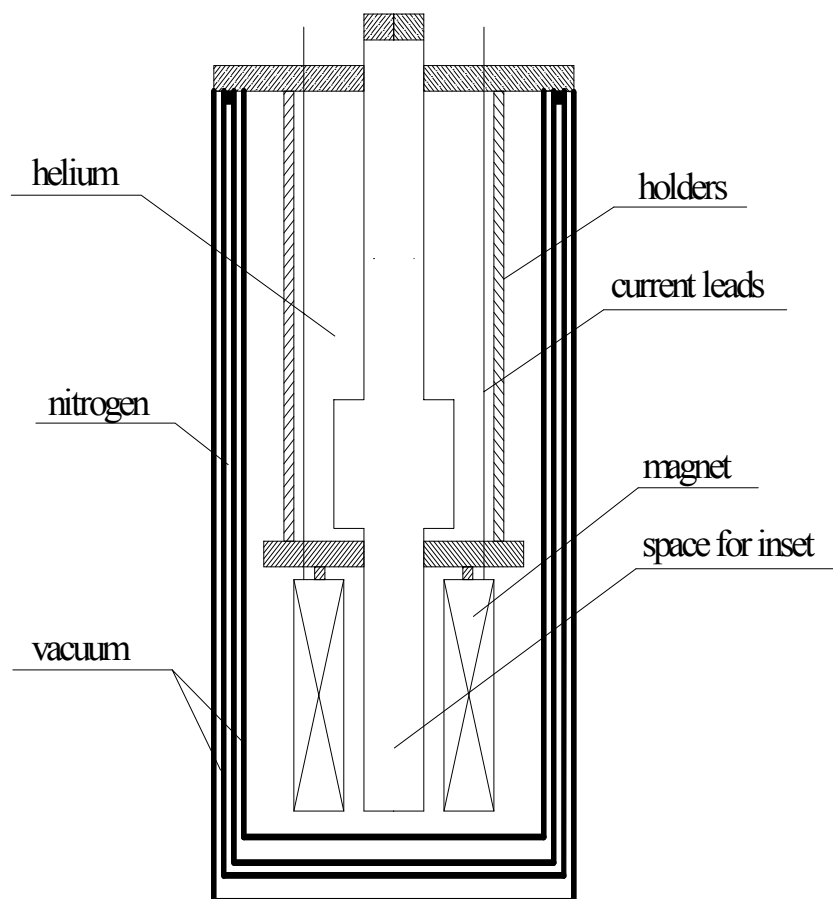
Pic.4.6.1. *Scheme of the cryostat.*

In the inner chamber of the cryostat the measurement stick with reed cell is placed. The presence of any gas leads to viscous damping of the reed oscillations. To avoid this effect the inner chamber is pumped. The pumping allows to reduce the damping by a factor of 10 and the quality factor of the reed can reach up to 50 000. For the thermal contact, Cu-Be clamps were used (see Fig.4.6.2.). The temperature range >10K can be set at gas pressure in the chamber $P \sim 10^{-6}$ mbar. For work at $T = 4.2$ K $-$ 10 K pressure $P \sim 10^{-4}$ mbar should be set. The temperature is regulated by Lake Shore Cryotronics DRC 91C temperature controller.
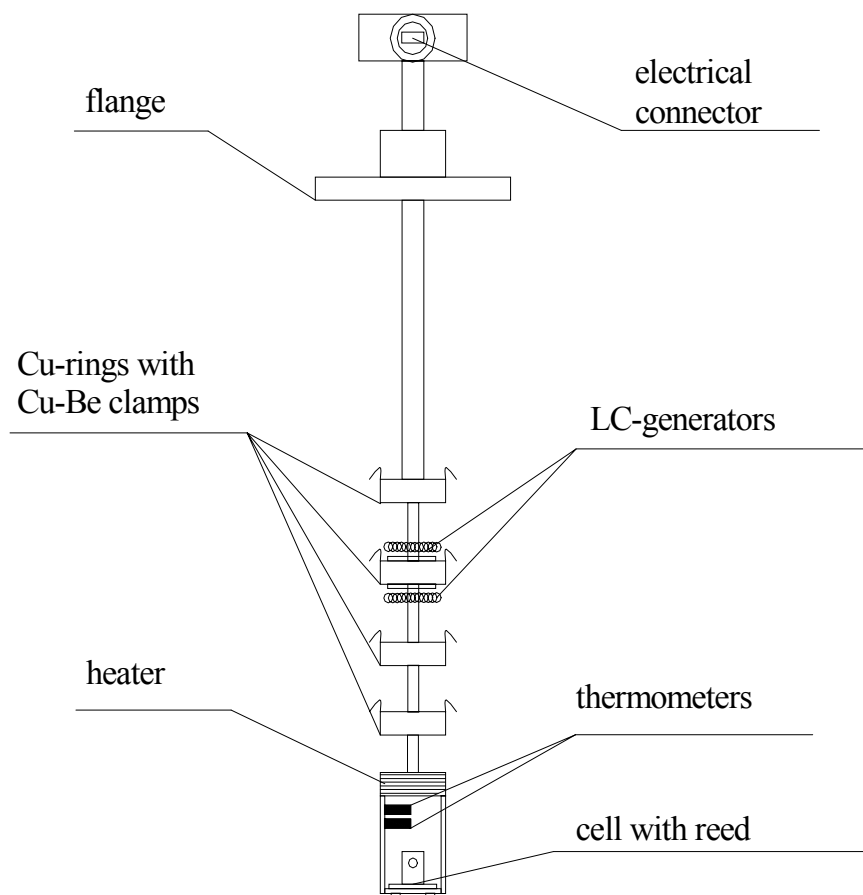
Pic.4.6.2. *Schematic picture of the measurement stick.*

Chapter 5

Mathematical description of a two-dimensional vibrating reed.

5.1. Two-fold symmetric potential

5.1.1. Reed without crystal

At small oscillations the reed without superconducting sample behaves like a driven harmonic oscillator with two degrees of freedom. So the movement of the reed can be described by two independent equations with two variables (see Appendix B):

$$\frac{d^2 x}{dt^2} + 2\Gamma_x \frac{dx}{dt} + \omega_{xr}^2 x = F_x e^{i\omega t};$$

$$\frac{d^2 y}{dt^2} + 2\Gamma_y \frac{dy}{dt} + \omega_{yr}^2 y = F_y e^{i(\omega t + \psi)} \equiv f_y e^{i\omega t},$$

[5.1.]

where Γ_x and Γ_y are the damping, ω_{xr} and ω_{yr} are the resonance frequencies of the reed for two modes of motion along two directions x and y, F_x and $f_y = F_y e^{i\psi}$ are proportional with factor $1/m^*$ (effective mass) to the amplitudes of the x and y components of the driving force acting on the reed with frequency ω. The phase shift between the driving forces is denoted ψ.

5.1.2. Reed with non-zero angle between crystal axes and reed axes

The behavior of the reed changes when an anisotropic superconducting sample is glued on it because of the vortex pinning. In the first case we will consider that the pinning potential has two-fold symmetry along crystal axis *a* and *b*. So this elliptical potential is proportional with factor $1/m^*$ to

$$U = \frac{\omega_{xs}^2 a^2}{2} + \frac{\omega_{ys}^2 b^2}{2},$$ [5.2.]

where $\omega_{xs}^2 - \omega_{ys}^2 = \gamma$ is the parameter of the anisotropy. If the crystal with such a pinning potential is glued so angle between the crystal system coordinate *a-b* and the reed system *x-y* is non-zero angle Θ (see Fig. 5.1.1), then coordinates *a* and *b* can be expressed as

$$a = x\cos\theta + y\sin\theta;$$
$$b = y\cos\theta - x\sin\theta.$$ [5.3.]
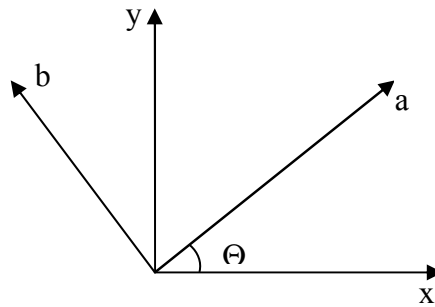
Figure 5.1.1. *Scheme of two coordinate systems: the easy axes x-y of the reed and the crystallographic axis a-b of the sample. The angle between them is Θ.*

The equations of motion are determined by the pinning forces proportional to $\dfrac{\partial U}{\partial x}$ and $\dfrac{\partial U}{\partial y}$.

$$\frac{d^2 x}{dt^2} + 2\Gamma_x \frac{dx}{dt} + \omega_{xr}^2 x + \frac{\partial U}{\partial x} = F_x e^{i\omega t};$$

$$\frac{d^2 y}{dt^2} + 2\Gamma_y \frac{dy}{dt} + \omega_{yr}^2 y + \frac{\partial U}{\partial y} = f_y e^{i\omega t};$$

[5.4.]

where m is effective inertia coefficient of the reed. Substituting [5.3] in the expression of the pinning potential we get

$$U = \frac{x^2}{2}\left(\omega_{xs}^2 - \gamma \sin^2 \theta\right) + \frac{y^2}{2}\left(\omega_{xs}^2 - \gamma \cos^2 \theta\right) + xy\gamma \cos\theta \sin\theta .$$

[5.4.]

Thus each partial derivative of the potential with respect to the coordinates has two terms

$$\frac{\partial U}{\partial x} = (\omega_{xs}^2 - \gamma \sin^2 \theta)x + (\gamma \cos\theta \sin\theta)y;$$

$$\frac{\partial U}{\partial y} = (\omega_{xs}^2 - \gamma \cos^2 \theta)y + (\gamma \cos\theta \sin\theta)x.$$

[5.5.]

So the pinning potential gives the additional restoring force (first term), which increases resonance frequencies ω_x and ω_y and adds mixing (second term) in the equations

$$\frac{d^2 x}{dt^2} + 2\Gamma_x \frac{dx}{dt} + \omega_x^2 x + cy = F_x e^{i\omega t};$$

$$\frac{d^2 y}{dt^2} + 2\Gamma_y \frac{dy}{dt} + \omega_y^2 y + cx = f_y e^{i\omega t};$$

[5.6.]

where

$$\omega_x^2 = \omega_{xr}^2 + \omega_{xs}^2 - \gamma \sin^2 \theta$$

$$\omega_y^2 = \omega_{yr}^2 + \omega_{xs}^2 - \gamma \cos^2 \theta$$

The c parameter depends only on angle θ and anisotropy γ

$$c = \gamma \sin\theta \cos\theta.$$

These equations can be solved in the standard way by substituting $x = \tilde{x}e^{i\omega t}$ and $y = \tilde{y}e^{i\omega t}$. The $\tilde{x}$ and $\tilde{y}$ are complex since they content the phase term $e^{i\delta_x}$ and $e^{i\delta_y}$.

$$-\tilde{x}\omega^2 + 2i\Gamma_x\tilde{x}\omega + \omega_x^2\tilde{x} + c\tilde{y} - F_x = 0;$$
$$-\tilde{y}\omega^2 + 2i\Gamma_y\tilde{y}\omega + \omega_y^2\tilde{y} + c\tilde{x} - f_y = 0.$$

These equations have been solved analytically using the Maple5 program:

$$\tilde{x} = -\frac{-\omega^2 F_x + 2i\Gamma_y\omega F_x + \omega_y^2 F_x + f_y c}{-\omega^4 + 2i\omega^3\Gamma_y + \omega^2\omega_y^2 + 2i\Gamma_x\omega^3 + 4\Gamma_x\Gamma_y\omega^2 - 2i\Gamma_x\omega\omega_y^2 + \omega_x^2\omega^2 - 2i\omega_x^2\Gamma_y\omega - \omega_x^2\omega_y^2 + c^2};$$

$$\tilde{y} = -\frac{-\omega^2 f_y + 2i\Gamma_x\omega f_y + \omega_x^2 f_y + F_x c}{-\omega^4 + 2i\omega^3\Gamma_y + \omega^2\omega_y^2 + 2i\Gamma_x\omega^3 + 4\Gamma_x\Gamma_y\omega^2 - 2i\Gamma_x\omega\omega_y^2 + \omega_x^2\omega^2 - 2i\omega_x^2\Gamma_y\omega - \omega_x^2\omega_y^2 + c^2}.$$

For a more clear interpretation it is possible to express these complex quantities in standard view: $\tilde{x} = \text{Re}_x + i\,\text{Im}_x$; $\tilde{y} = \text{Re}_y + i\,\text{Im}_y$, where

$$\text{Re}_x = \frac{A[(\omega^2 - \omega_y^2)F_x - cF_y\cos\psi] + B[2\Gamma_y\omega F_x + cF_y\sin\psi]}{A^2 + B^2};$$

$$\text{Im}_x = \frac{B[(\omega^2 - \omega_y^2)F_x - cF_y\cos\psi] + A[2\Gamma_y\omega F_x + cF_y\sin\psi]}{A^2 + B^2};$$

$$\text{Re}_y = \frac{A[2\Gamma_x\omega F_y\sin\psi + (\omega^2 - \omega_x^2)F_y\cos\psi - cF_x] + B[2\Gamma_x\omega F_y\cos\psi - (\omega^2 - \omega_x^2)F_y\sin\psi]}{A^2 + B^2};$$

$$\text{Re}_y = \frac{B[2\Gamma_x\omega F_y\sin\psi + (\omega^2 - \omega_x^2)F_y\cos\psi - cF_x] + A[2\Gamma_x\omega F_y\cos\psi - (\omega^2 - \omega_x^2)F_y\sin\psi]}{A^2 + B^2}.$$

Here denote

$$A = 4\Gamma_x\Gamma_y\omega^2 + c^2 - (\omega^2 - \omega_x^2)(\omega^2 - \omega_y^2);$$

$$B = 2\Gamma_x(\omega^2 - \omega_y^2) + 2\Gamma_y(\omega^2 - \omega_x^2).$$

[5.11.]

This solution means movement of the reed on an elliptical trajectory $x = |x|\, e^{i(\omega t + \phi_x)}$ and

$y = |y|\, e^{i(\omega t + \phi_y)}$, where $|x| = \sqrt{\mathrm{Re}_x^2 + \mathrm{Im}_x^2}$; $\tan\phi_x = \dfrac{\mathrm{Im}_x}{\mathrm{Re}_x}$ and analogically for y. When the

phase difference $\delta\phi = \phi_x - \phi_y$ is equal to 90°, the reed trajectory is a circle. When the

phase difference $\delta\phi$ is equal to zero the ellipse becomes a straight line.
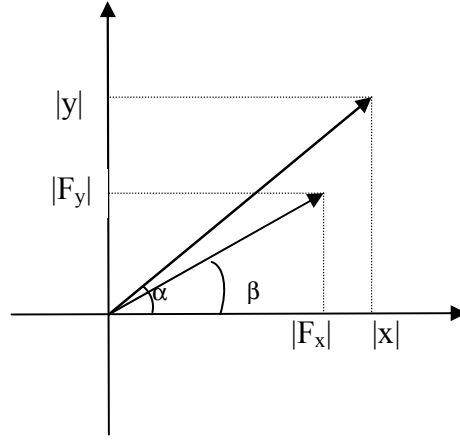
Figure 5.1.2. *Schematic picture of the driving force and amplitude directions.* $|x|$ *and* $|y|$ *are the components of the amplitude of the reed elongation from the equilibrium position. Angle* α *determines the elongation direction.* $|F_x|$ *and* $|F_y|$ *are the components of the amplitudes of the driving force and* β *is angle between the force direction and x axis.*

For such a mode of motion it is possible to extract the value of anisotropy c from this solution. One of the easiest ways (theoretically and experimentally) is to analyze the motion of the reed along a straight line, partially analyze the dependence of the elongation of the reed $(|x|, |y|)$ on the driving force $(|F_x|, |F_y|)$ at $\delta\phi = 0$ (see Fig.5.1.2). The adjusting of $\delta\phi$ is possible by changing phase shift ψ of the force y component $f_y = F_y e^{i\psi}$. Thus the condition $\delta\phi = 0$ leads to additional requirements for phase ψ:

54

$$\frac{\operatorname{Im}\widetilde{x}(\psi)}{\operatorname{Re}\widetilde{x}(\psi)} - \frac{\operatorname{Im}\widetilde{y}(\psi)}{\operatorname{Re}\widetilde{y}(\psi)} = 0 \,.$$

[5.12.]

From this equation we find the value of phase ψ, at which the reed moves along a straight line. Substituting of real experimental parameters allows solving of the equation [5.12.] numerically. Knowing of the value of the phase ψ allows to find the components of the amplitude of the reed elongations |x| and |y|. Thus we simulate the motion of the reed along a straight line with the amplitudes $\sqrt{|x|^2 + |y|^2}$ and direction angle $\alpha = \arctan(|x|/|y|)$. This angle is not equal to the driving force angle $\beta = \arctan(|F_x|/|F_y|)$ in the general case and the value of the parameter c is crucial for the dependence of α on β as shown in Fig.5.1.3. These results were obtained for reed parameters $\omega_x = 399.8 \text{ s}^{-1}$; $\omega_y = 400.2 \text{ s}^{-1}$; $\Gamma_x = 0.05 \text{ s}^{-1}$; $\Gamma_y = 0.05 \text{ s}^{-1}$ and for a driving frequency of 400 s^{-1}. It is obvious that for zero value of c the reed moves along the direction of the applied driving force and the deviation angle α is equal to the force angle β. With increasing c difference between α and β increases. Also some disturbances are observed around zero and $\pi/2$, caused probably by numerical problems. At very big values of c difference between α and β is almost $\pi/2$ and disturbances disappear. Here the results for positive anisotropy are shown. The calculation with negative value of c demonstrates similar behaviour with opposite phase shift.
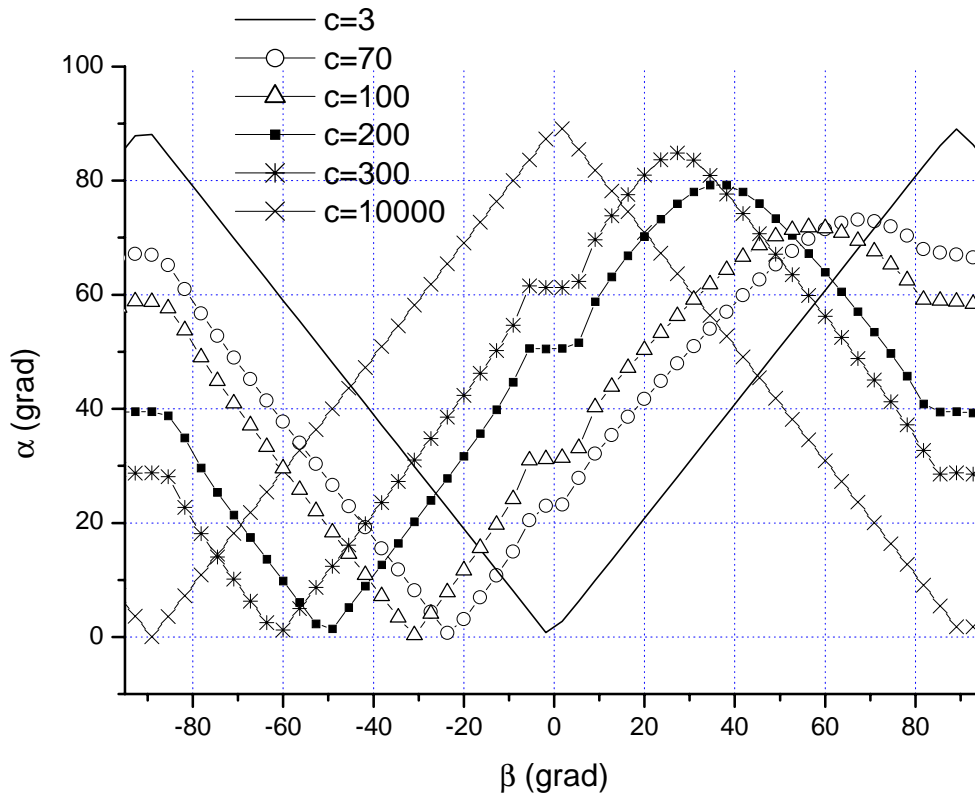
Figure 5.1.3. *Results of calculations for two-fold symmetric potential. The calculation has been carried out for ω_x =399.8 s^{-1} ; ω_y = 400.2 s^{-1}; Γ_x = 0.05 s^{-1}; Γ_x = 0.05 s^{-1} and for driving frequency 400 s^{-1}. The values of c were from 0 to 10000 s^{-1}. At smaller c the difference between α andβ is almost zero. With increasing anisotropy this difference also grows up asymptotically to 90°.*

5.2. Four-fold symmetric potential

5.2.1. The approximation of the pinning potential

To find higher order symmetry of the pinning potential it is necessary to eliminate the influence of the two-fold symmetric potential on the reed behaviour. This is possible in

experiment with sample glued so crystallographic axes coincide with principal axes of the reed. In this case the value of the two-fold anisotropy parameter $c = \gamma \sin\theta \cos\theta$ will by equal to zero.

Now let us consider the more complicated case of four-fold symmetry of the pinning potential. The simplest way to set such potential is approximate it by a term $X^2 \cdot Y^2$ (it gives fourfold symmetry) instead of $X \cdot Y$, which is equal to zero at zero angle between crystal and reed axis. Thus the potential is proportional with factor $1/m^*$ to

$$U_0 = \frac{\omega_s^2}{2} X^2 + \frac{\omega_s^2}{2} Y^2 + \beta_0 X^2 Y^2. \qquad [5.13.]$$

Here X and Y are the components of the displacement in the potential. Since the shape of the equipotential lines depends on the displacement, it is convenient to introduce the normalizing amplitude A and divide the equation by the square of it. Then we have the equation

$$U = \frac{\omega_s^2}{2} x^2 + \frac{\omega_s^2}{2} y^2 + \beta x^2 y^2, \qquad [5.13a]$$

where $x = X/A$ and $y = Y/A$ are dimensionless components of the displacement, U is value proportional to the potential, and β is parameter of four-fold anisotropy with dimension [s^{-2}].

For small amplitudes, the potential is almost isotropic. At range $x \sim \sqrt{\omega^2/\beta}$, this expression gives the shape of the potential similar to that theoretically described in Chapter 2 (see Fig. 2.3.3). The shape of the potential [5.13] was calculated for ω_s=3 s^{-1} and β = 1000 s^{-2} and is shown in Figure 5.2.1 in range x, y = [-0.2, 0.2]. For the amplitudes $x \gg \sqrt{\omega^2/\beta}$ the approximation yields the shape quite different from the theoretical description, which predicts an almost round shape of the potential at large amplitude.
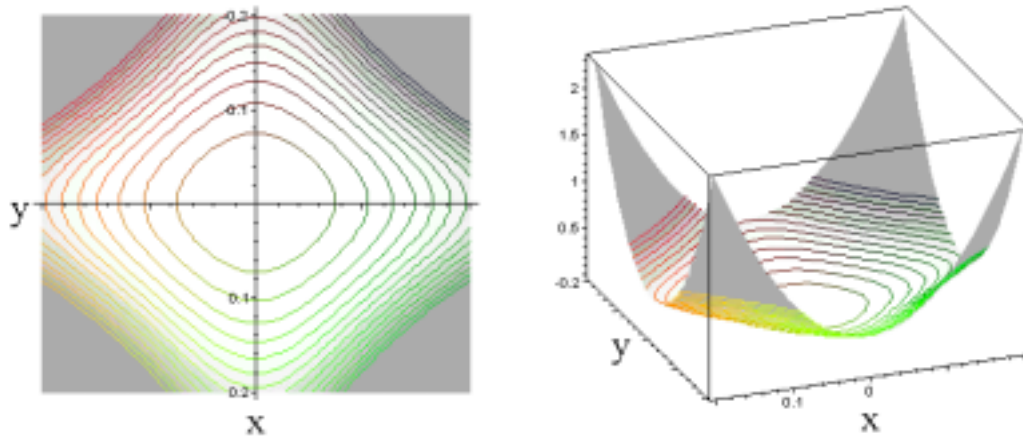
Figure 5.2.1. *Shape of the potential with four-fold symmetry*
$U = \dfrac{\omega_s^2}{2} x^2 + \dfrac{\omega_s^2}{2} y^2 + \beta x^2 y^2$. *Contour plot and 3D illustration. The ω_s=3 s^{-1} and β = 1000 s^{-2} for x, y $\in$ [-0.2, 0.2]*

5.2.2. Analysis of the equation of motion

Unfortunately the analytic solution of such equations is impossible, but some analysis of the equation can be done. Let us assume that we can make the reed to move in one plane in such potential. The movement parallel to one axis will be described by the simple equation of the harmonic oscillator with frequency ω_s. The more complicated case is the vibration at some angle to the axis. For oscillation in the 45°-plane $x = y$ and the pinning potential will be

$$U = \frac{\omega_s^2}{2} \bar{x}^2 + \frac{\beta}{4} \bar{x}^4 \,, \qquad [5.14.]$$

where $\bar{x} = \sqrt{2}x$. The equation of motion is determined by the pinning potential of the sample and the properties of the reed itself

$$\frac{d^2\overline{x}}{dt^2} + 2\Gamma\frac{d\overline{x}}{dt} + \omega_0^2\overline{x} + \beta\overline{x}^3 = fe^{i\omega t} . \qquad [5.15.]$$

Here $f = F/A{\cdot}m^*$ is value proportional to the applied driving force. The frequency $\omega_0^2 = \omega_r^2 + \omega_s^2$ is the resulting frequency of the reed and the sample. The solution of such an equation is considered elsewhere, for example in [82]. This anharmonic potential leads to a shift of the resonance frequency and appearance of the third harmonic. The shift of the resonance frequency is proportional to the square of the amplitude of the oscillations $a = |\overline{x}|$

$$\delta\omega = \frac{3\beta}{8\omega_0}a^2 . \qquad [5.16.]$$

The resonance curve near resonance is given by the equation:

$$a^2\left[(\varepsilon - \kappa a^2)^2 + \Gamma^2\right] = \frac{f^2}{4\omega_0^2} , \qquad [5.17.]$$

where $\varepsilon = \omega - \omega_0$ and $\kappa = \dfrac{3\beta}{8\omega_0}$. At small force f amplitude a is also small, so it is possible to neglect the terms of higher powers of a and we will have the symmetric resonance curve with the maximum at $\varepsilon = 0$ (see Fig. 5.2.2.). Increasing of f results in deformation of the curve and the maximum shifts to positive values in case of $\beta > 0$. From the three roots of the equation the only one is real. At $f > f_k$ the equation has three real roots, and the curve becomes two-valued and bistability occurs.
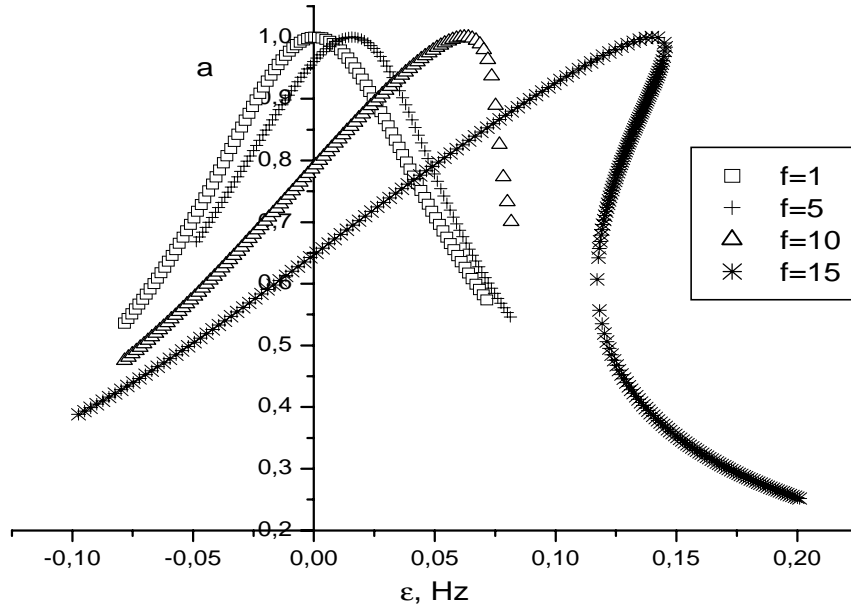
Figure 5.2.2. *Resonance curve of the anharmonic oscillator for different driving force. The amplitude of the oscillation were normalised to the resonance amplitude. The shift of the maximum increases with the driving force and the amplitude of oscillations. At f>10 s⁻² bistability appears. The shift of the resonance at f_k is $\sqrt{3}\Gamma$.*

The calculations present below were made for the parameters of the reed close to the experimental ones: $\omega_r = 400$ s⁻¹ and $\Gamma = 0.05$ s⁻¹. The parameters of the pinning potential in the sample were the same as before: $\omega_s = 9$ s⁻¹ and $\beta = 1000$ s⁻². These values of the parameters are in agreement with the experimental data (see Chapter 6): $\delta\omega^2 = \omega_0^2 - \omega_r^2 \approx 2\omega_r\omega_s = 7000 \text{ s}^{-2}$. The resonance curves shown in Fig.5.2.2 are obtained for different driving forces. The amplitude of oscillation are normalised to resonance amplitudes, which are equal to 0.025, 0.125, 0.25 and 0.375 for driving forces equal to1, 5, 10 and 15 s⁻² accordingly.

5.2.3. The estimation of the measured values

The position of the maximum can be found by equating the derivative of $a(\varepsilon)$ to zero:

$$\frac{da}{d\varepsilon} = \frac{-\varepsilon a + \kappa a^3}{\varepsilon^2 + \Gamma^2 - 4\kappa\varepsilon a^2 + 3\kappa^2 a^4} = 0 .$$ [5.18.]

Thus $\varepsilon = \kappa a^2$ and $a_{max} = f/2\omega_0\Gamma$ which is the same maximal amplitude as that of the harmonic oscillation. Bistability occurs at points A and B. The position of these points is determined by the condition $\frac{da}{d\varepsilon} = \infty$ and thus by the solutions of equation

$$\varepsilon^2 + \Gamma^2 - 4\kappa\varepsilon a^2 + 3\kappa^2 a^4 = 0 .$$ [5.19.]

When the determinant of this equation is equal to zero, it has only one solution and points A and B coincide. This happens at $f = f_k$. The resonance shift at the critical force f_k is $\varepsilon_k = \sqrt{3}\Gamma$ (about 0,06Hz) which is a measurable value.

The other feature of the anharmonity of the potential is the appearance of the third harmonic

$$x^{(3)} = \frac{a^3\beta}{32\omega_0^2}\cos 3\omega t .$$ [5.20.]

Thus the ratio of signal of the third harmonic to that of the first harmonic is proportional to $a^2\beta$. Since this parameter has dimensionality of s^{-2} and does not depend on the units of amplitude we can use the same values of $a = 1$ and $\beta = 1000$ for estimation. The estimation gives $\frac{|x^{(3)}|}{a} = 2\cdot10^{-4}$. Unfortunately, the accuracy of our experiment is not enough to detect such a signal.

Chapter 6

Experimental results

6.1. Two-fold anisotropy

6.1.1. The field dependence of the resonance enhancement

The vibrating reed technique is a powerful tool for the investigation of the interaction between the flux line lattice and the pinning centers in the superconductor. The direct measurement of the elastic coupling parameter α (Labusch parameter) is possible when the Campbell penetration depth λ_{44} is larger than the sample dimension along the field direction. In our case, the important sample size is the crystal thickness along the c direction since the field was always directed perpendicular to the a-b surface. The thickness of the samples used in the experiment was less than 100 μm.

As it was demonstrated in [36], the Labusch parameter α can be estimated from the frequency enhancement and from the line tension P

$$(\omega^2 - \omega_0^2)\frac{I}{l} = P = w_s l_s \alpha \frac{d_s^2}{3} \frac{d_s}{l} \qquad [6.1]$$

where I is the effective moment of inertia of the reed, l is its length, and $w_s,$ l_s and d_s describe the geometrical size of the superconducting sample.

Measurements of the resonance frequency enhancement of the YBa$_2$Cu$_3$O$_{7-\delta}$ single crystal (YBCO-A, 1.5 × 0.8 × 0.05 mm^2) are shown in Fig.6.1.1. From these measurements, we obtain an estimate of the Labusch parameter α about 10^{13} N m^{-4}. Thus, the penetration depth λ_{44} is about 200μm, which is larger than the sample thickness d$_s$/2 ≈ 25 μm. This estimate demonstrates the consistency of the description.
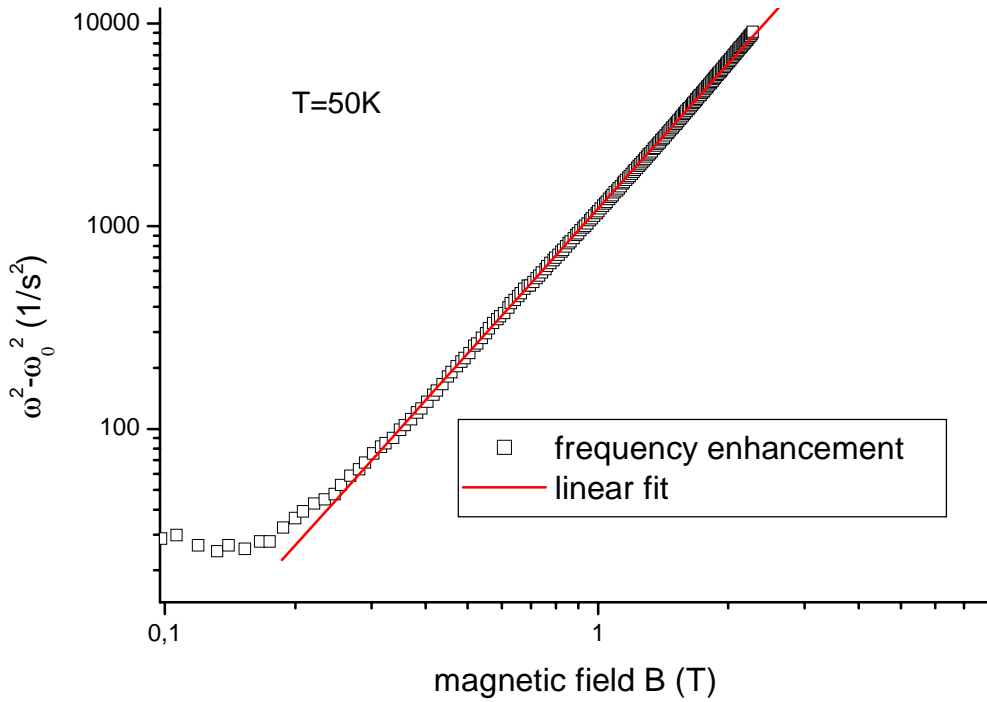
Figure 6.1.1. *Log-log plot of the resonance frequency enhancement of YBa$_2$Cu$_3$O$_{7-\delta}$ single crystal (YBCO-A) as a function of the magnetic field B at the temperature T = 50K. The line is linear fit proportional to B$^{2.4}$.*

This conclusion is confirmed by the measurements of the resonance frequency enhancement as a function of magnetic field. The experimental results show that frequency enhancement is not proportional to B^2 at temperatures below *75 K*. The linear fit of the data shows that $\omega^2 - \omega_0^2 \propto B^{2.4}$. This dependence of the line tension is different from the proportionality $c_{44} = B_a B/\mu$ which is attributed to the distortion of the

magnetic field or tilt of the flux line lattice. The proportionality different from B^2 might be interpreted as an indication that the line tension is provided by elastic pinning. In this case the dependence of line tension on magnetic field indicates that the Labusch parameter of the elastic coupling is proportional to $B^{2.4}$.

The most important conclusion is that the frequency enhancement and additional restoring force are not caused by a geometrical effect. They are provided by elastic interaction between flux line lattice and pinning centers.

6.1.2. Pulse excitation experiment

The response of the two-dimensional reed to a pulse excitation can be predicted from the equations of motion. When the reed is well adjusted the two coordinates x and y are independent. In this case, the motion of the reed would be the summation of two normal modes of the free oscillations with frequencies ω_{0x} and ω_{0y}. These oscillations decay because of the damping in time $\tau = \dfrac{Q}{2\pi\omega_0}$. Thus, the signal on each of the electrodes will be a damped oscillation with one degree of freedom. The output of the lock-in amplifier displayed on the oscilloscope is shown in Fig.6.1.2. Such signal of single-mode free oscillation is observed at any initial conditions and it is independent on direction and magnitude of the initial distortion of the reed.
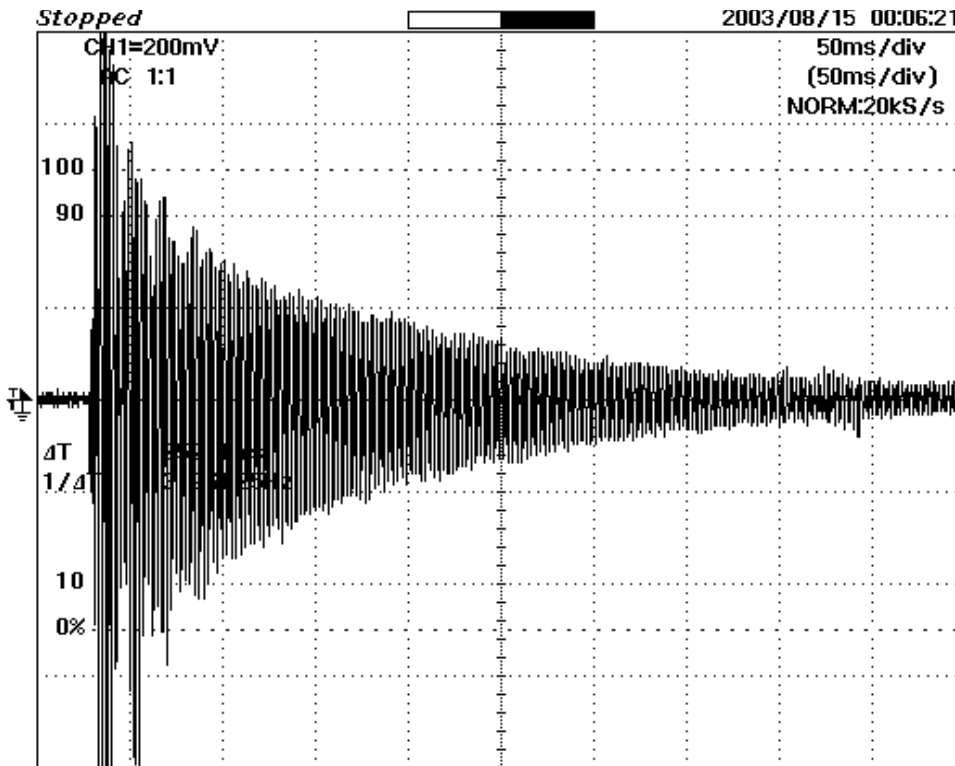
Figure 6.1.2. *Lock-in signal on the oscilloscope from the x electrode representing the response on a pulse excitation of the well adjusted reed. The x and y coordinates are completely independent so response is the same as the response of the one-dimensional damped oscillator.*

The situation changes when the additional mixing term appears in the restoring force. In this case, the damped oscillations have beating with frequency ω_{0x}-ω_{0y}. The additional restoring force acts on the superconductor and reed in a magnetic field. This force can have a mixing term if the superconducting crystal has a not isotropic pinning potential, and if such superconducting sample is glued to the reed under some nonzero angle between the main axis of inertia of the reed and crystal axis, i.e. axis of the pinning symmetry. A thin superconducting crystal $YBa_2Cu_3O_{7-\delta}$ (YBCO−A) was glued at 20° angle to reed axis. Fig.6.1.3 shows the response of the reed to the pulse excitation at *B=0.8 T* at a temperature below transition temperature. The beating of the oscillation is clearly seen in this case. The Fourier transform of the signal has two distinct peaks corresponding two modes *x* and *y*. The distance between the modes is about 10Hz. The

other peaks in the Fourier transform are the 100Hz modes from the outside noise. However being far away from the resonance frequency of the reed, these parasite signals have no effect on the experiment.
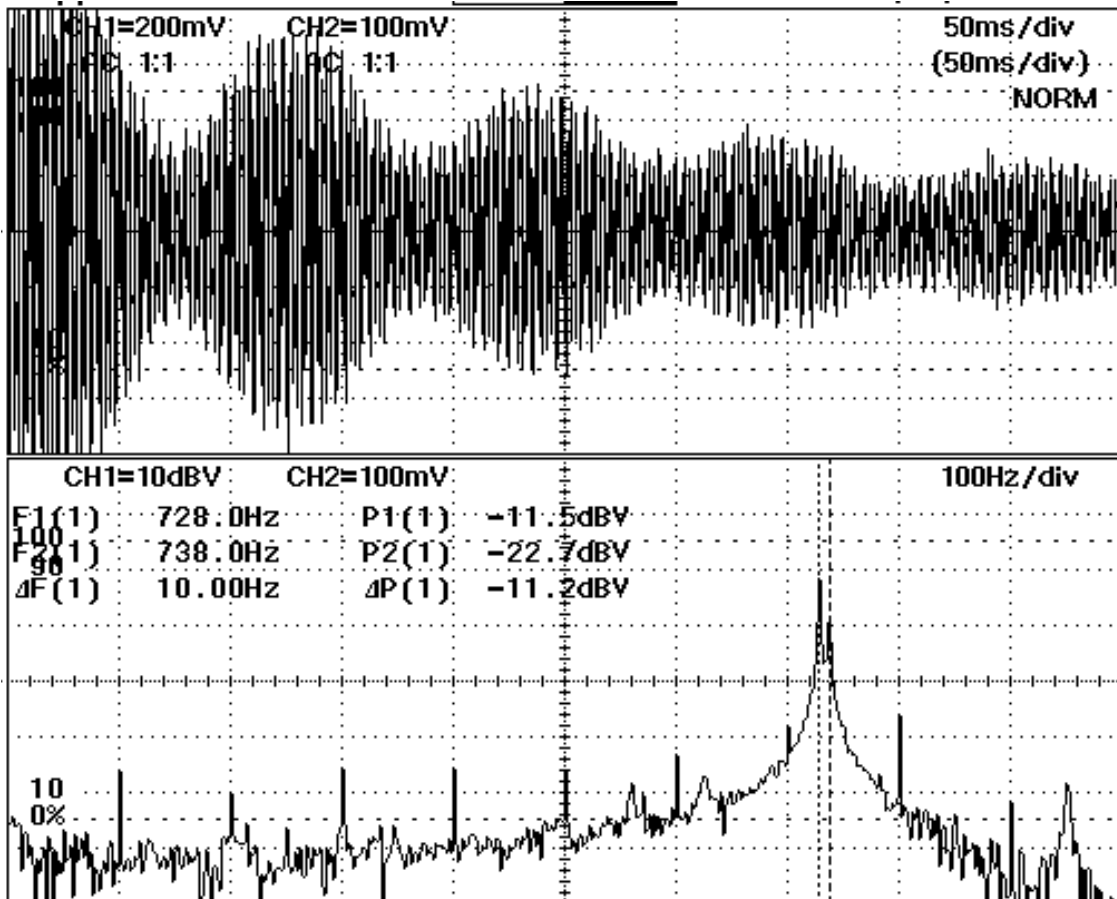
Figure 6.1.3. *The oscilloscope signal for the x direction in a magnetic field B = 0.8 T. The superconducting crystal YBCO-A was glued under an angle of about 20 degree between the crystal axis and the x-y directions of the oscillation. The lower picture is the Fourier transform of the signal. Two modes are clearly seen. Also 100Hz modes of the parasite signal can be seen.*

Above the transition temperature the magnetic field has no effect on the reed free oscillations and we observe the signal of two independent modes *x* and *y* on both electrodes.

The mixing of two modes demonstrates that the restoring force has anisotropic symmetry. This restoring force is associated with the pinning potential since the sample is thin (the thickness d is smaller than Campbell penetration depth λ) as is seen from the field dependence of the resonance enhancement. Thus, we observe the force associated with the Labusch parameter and this effect is not caused by geometrical size of the sample. Similar results were obtained in an experiment with a square-shaped crystal of $YBa_2Cu_3O_{7-\delta}$ (YBCO-B).

In addition, experiments with $Bi_2Sr_2CaCu_2O_{8+\delta}$ rectangular samples glued at some nonzero angle were carried out. The results of these experiments show no indication of the mode mixing at magnetic fields up to 3 T. This demonstrates that beating is associated with the anisotropy of the pinning potential. Most obviously, it is caused by the intrinsic symmetry of the $YBa_2Cu_3O_{7-\delta}$ crystal structure, which has a well established anisotropy in the a-b plane.

6.1.3. Constant drive experiment

The previous observation of free oscillations is a qualitative experiment. More information can be obtained from driven oscillations. In case of the adjusted reed no mode-mixing forces are acting on the reed. Thus, the driving voltage applied along one of the reed axes results in stable oscillation in this direction. The amplitude of this oscillation is proportional to the square of this driving voltage. The signal at the perpendicular direction is equal to zero. This fact and the absence of beating at free oscillations are used for the adjustment of the electrodes along main axes of inertia of the reed.

The mode-mixing force results in an elliptic motion. Thus, a signal appears in the direction perpendicular to applied driving force. In the experiment with the YBCO-A sample the perpendicular signal increases with the magnetic field since the mode-mixing force is associated with elastic pinning and increases with vortex density.

The results of this experiment are shown in Fig.6.1.4. The driving voltage was applied along the *x* direction. At zero magnetic field, the *y* signal was zero within the accuracy of the measurements. Applying a magnetic field leads to an increase of this signal. At a temperature *T=60 K* the amplitude along *x* direction does not change up to *B* = 1 T. The amplitude of the oscillation along the driving force is proportional to the damping, associated with vortex motion. Thus, the depinning of the vortices starts at higher magnetic field than the mode-mixing. Therefore, the mode-mixing force is not related to vortex motion and depinning.
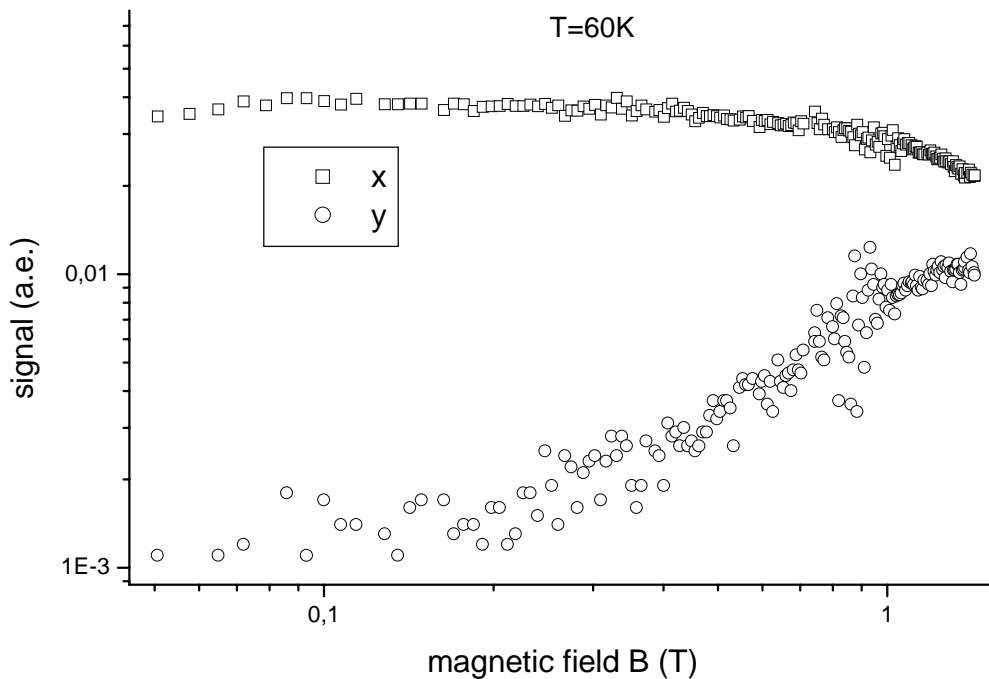
Figure 6.1.4. *Increase of the y-signal in magnetic field for a reed driven along the x direction. The experiment was carried out with superconducting crystal YBa₂Cu₃O₇₋δ (YBCO-A) at T =60 K. The mode-mixing appears at about 0.2 T. That is much smaller than the field at which depinning starts (about 1 T).*

For temperatures closer to T_c the depinning starts at lower fields. Figure 6.1.5 shows that at *T = 75 K* the damping starts to grow near the field *0.6 T* and the *x* amplitude

decreases. The *y* amplitude grows up at smaller fields (~0.2 T) and then drops because of high damping of the reed.

Thus, the effect of the mode-mixing is a property of the superconductor sample with pinned vortices. However, for more quantitative results, a detailed experiment with angular resolution is required.
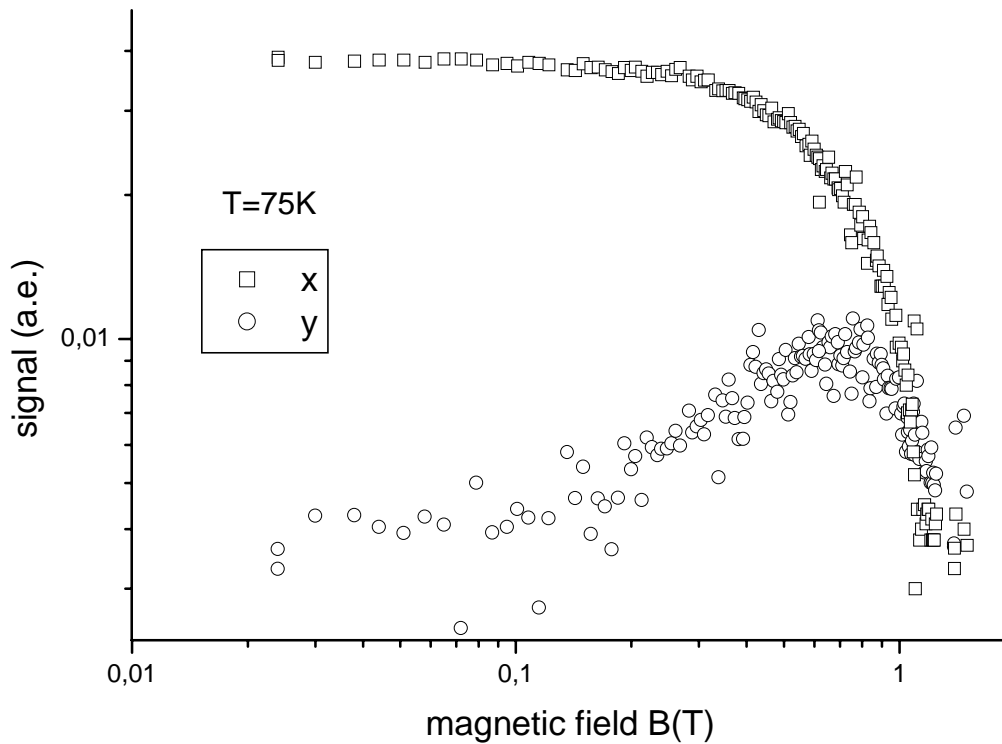
Figure 6.1.5. *Increase of the y-signal in magnetic field. The driving voltage is applied along x coordinates. The experiment was carried out with superconducting crystal YBa$_2$Cu$_3$O$_{7-\delta}$ at temperature T =75 K. Depinning starts at field about 0.6 T. At depinning both signals decrease to zero because of high damping.*

6.1.4. Angular dependence

The main idea of another constant drive experiment is clear after the mathematical consideration described in Chapter 5.1. The driven planar oscillations allow quantitative measurements of the anisotropy in the *a-b* plane. If two-fold symmetry anisotropy is assumed, the parameter *c* characterizes this anisotropy and it can be determined from the angular dependence of the response.

The motion of the reed depends on the magnitudes (F_x, F_y) and phases (ψ_x, ψ_y) of the applied driving forces. The amplitudes of the oscillations depend on the magnitudes of the force components. The phase difference of the driving forces ψ_x - ψ_y determines the signal phase difference. At a certain phase difference the reed performs planar oscillations. The regulation of the amplitudes and phases was carried out with the help of the program in LabView (Diag.4, Appendix A). This program controls one of the driving phases such that the signal phase difference is kept equal to zero or π. Simultaneously, the amplitudes are regulated such that the value $\sqrt{x^2 + y^2}$ is constant. While keeping these values constant, the program changed the ratio F_x / F_y to scan the angle β = arctan *(F_x/F_y)* from zero to $\pi/2$. Measuring the angle of reed deviation α = arctan *(x/y)* as a function of β gives the possibility to find the value of the two-fold anisotropy. It is clear that in absence of a magnetic field the reed oscillation direction is the same as the direction of the driving force, and $\alpha = \beta$. Measurable changes appear at higher fields when the mode-mixing force is strong enough.

The scanning of the angle β results in a multivalued function $\alpha(\beta)$, which is difficult to measure. This leads to an uncertainty in the values of the function and some additional artefact points near $\beta = 0$. However, careful low-noise measurements are possible and give results, which are very close to the mathematical simulations.

Figure 6.1.6 shows the dependence α on β measured by this method on the reed with YBCO-A crystal glued at a non-zero angle. The measurements were carried out at 76 K and at magnetic fields *B = 0.75 – 1.05 T* i.e. at fields when the mode-mixing force is

highest but the damping is still moderate. The graphs shown differ from the diagonal line $\alpha = \beta$. The main feature of the graphs is the second branch in the angular range $\beta <$ 0.3 rad. The zero value of β is not at the point $\alpha = 0$ as it is in the absence of a magnetic field and mode-mixing force. This point is displaced to a higher value of α. The position of this minimum depends on the magnetic field and shifts from $\alpha = 0.1$ rad ≈ 6 degree at $B = 0.75\ T$ to $\alpha = 0.35$ rad ≈ 20 degree at $B = 1.05$ T. At lower fields, the plot is almost undistinguishable from the zero field curve. At higher fields, the measurements become complicated because of the too strong mode-mixing and too strong damping.
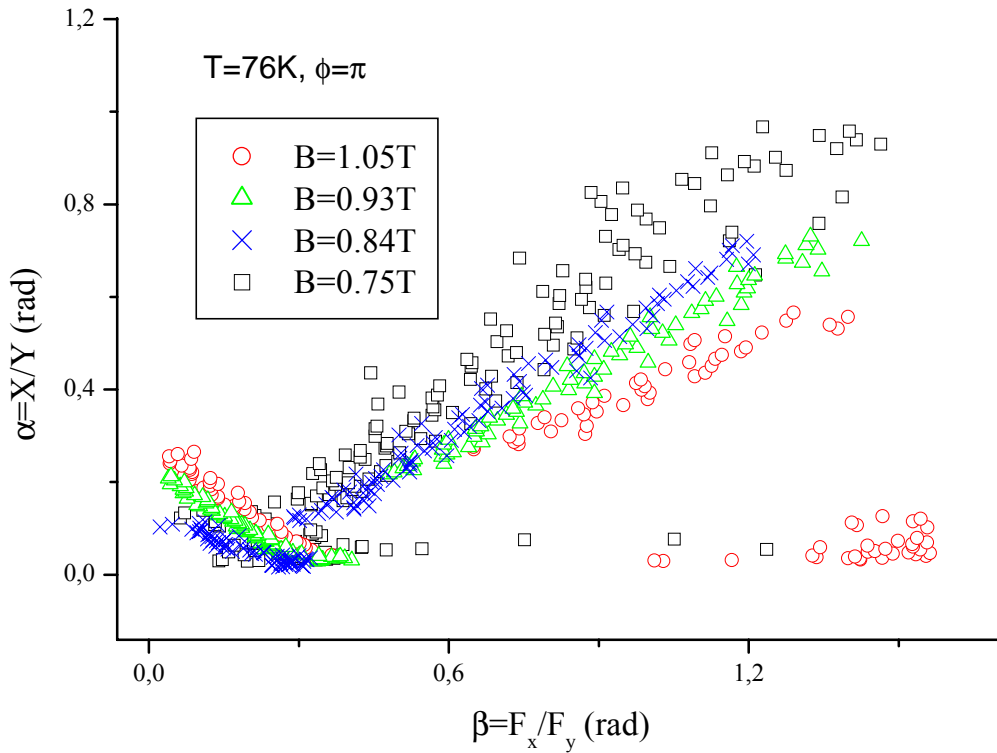
Figure 6.1.6. *The dependence of α on β measured at T = 76 K and magnetic fields B = 0.75 – 1.05 T. The signal phase difference ϕ was π. We observe a multivalued function, which has two branches at each field value.*

The results of the experiment carried out at $T = 76$ K and $B = 0.93$ T is shown in Fig.6.1.7. These measurements have been done for a phase difference $\phi = 0$ and $\phi = \pi$, i.e. at full range of the angle α. Thus we observe a curve which is very similar to the mathematical simulation described in Chapter 5.1. The calculations were made with Maple5 program. The parameters used in calculations were close to those measured: $\omega_x = 399.8$ Hz; $\omega_y = 400.2$ Hz; $\Gamma_x = 0.02$; $\Gamma_y = 0.02$ and driving frequency $\omega = 400$ Hz. The only fitting parameter c characterizes two-fold symmetry. The best fit yields $c = 60$.
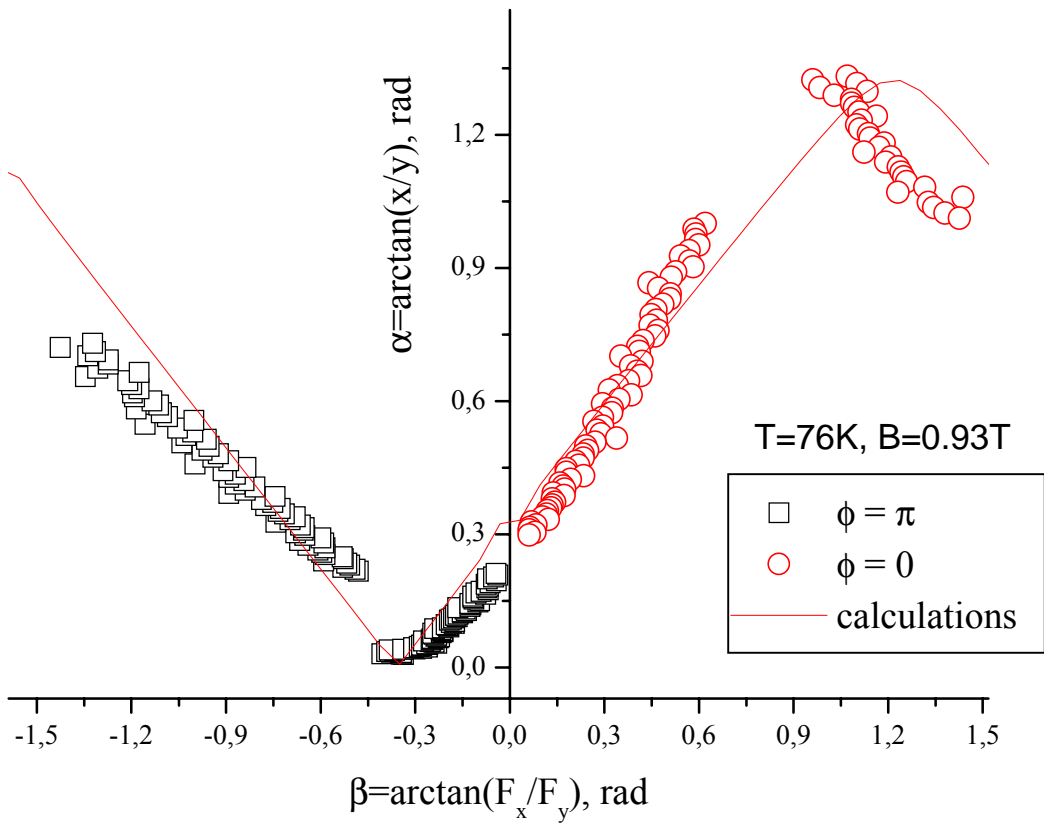
Figure 6.1.7. *The dependence of α on β measured at $T = 76$ K and magnetic fields $B = 0.93$. The signal phase difference was kept zero and π. Thus, we scan the full range of the angle α. The line is the result of the simulations. The parameter of the two-fold symmetry used for this fit was $c = 60$.*

6.1.5. Estimation of the anisotropy

Once the value of the parameter c is known, we can estimate the value of the two-fold symmetry. The parameter c is determined by the anisotropy γ of the pinning potential and angle θ between the direction of the crystallographic axes a-b and reed coordinates x-y:

$$c = \gamma sin\theta cos\theta. \qquad [6.2]$$
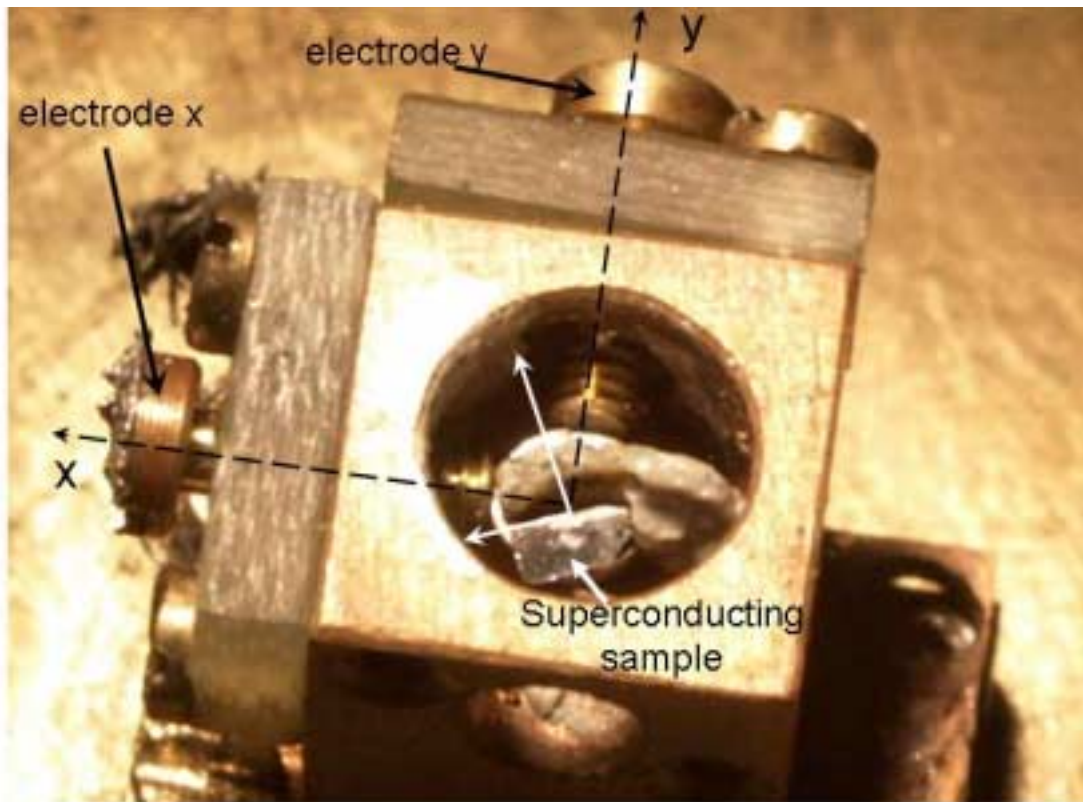
Figure 6.1.8. *Photograph of the cell. The two screws are the electrodes, which determine the directions x and y shown as dashed black lines. The thick white arrow points at the superconducting sample, which is glued on top of the reed (cannot be seen in the picture). Small white axes indicate the direction of the a-b crystallographic axes of the $YBa_2Cu_3O_{7-\delta}$ sample. The angle θ between these two coordinate systems is about 23°.*

The angle θ can be determined from the photograph shown in Fig.6.1.8. The coordinates x and y are determined by the two screws which are used as driving and detecting electrodes. The direction of the crystallographic axes a and b is readily determined from the photo since they are parallel to the crystal edges. Knowing the angle $\theta \approx 23°$ allows us to find the anisotropy $\omega_{xs}^2 - \omega_{ys}^2 = \gamma \approx 170$. Here ω_{xs}^2 and ω_{ys}^2 are the coefficients in the pinning potential of the superconducting sample $U = \dfrac{\omega_{xs}^2 a^2}{2} + \dfrac{\omega_{ys}^2 b^2}{2}$ (see Chapter 5.1.)

$$\omega_x^2 = \omega_{xr}^2 + \omega_{xs}^2 - \gamma \sin^2 \theta$$
$$\omega_y^2 = \omega_{yr}^2 + \omega_{xs}^2 - \gamma \cos^2 \theta \qquad\qquad [6.3]$$

This potential is the origin of the additional restoring force, which results in a frequency enhancement $\omega^2(B) - \omega_0^2 = \omega_{xs}^2 - \gamma \sin^2 \theta$. Thus, knowing the frequency enhancement, we can evaluate the relative anisotropy $\gamma = 1 - \omega_{xs}^2 / \omega_{ys}^2 \approx 10\%$. This value is in a good agreement with measurements of the anisotropy in the penetration depth of YBa$_2$Cu$_3$O$_{7-\delta}$ single crystals [83], which gives $\gamma_{ab} = 1.15$, and magnetic torque measurements [84] yielding $\gamma_{ab} = 1.18$.

6.2. Search of the four-fold symmetry

6.2.1. Reverse resonance curve

The mathematical description of the oscillation of the reed gives clues to the search of the four-fold symmetry of the pinning potential. The superconducting sample was glued so its crystallographic axes coincide with the principal axes of the reed. In this case, the two-fold symmetry parameter $c = \gamma \sin\theta \cos\theta$ is equal to zero. Thus, all two-fold symmetry effects should disappear. Indeed, for the YBa$_2$Cu$_3$O$_{7-\delta}$ samples glued parallel to the x-y axes, no mode-mixing was observed in a magnetic field up to 2.5 T. No

beating was observed in the free oscillation of the reed. Also in the experiment with constant drive, there was no increase of the signal perpendicular to the applied driving force.

As shown in Chapter 5.2, a four–fold symmetry should manifest itself in anharmonical motion and in the change of the resonance curve in dependence of the angle of the plane of oscillations. The theoretical prediction shows that four-fold symmetry of the pinning potential can be observed only in very narrow range of the elongation of the vortex from the pinning center. Thus, the measured effect depends strongly on the amplitude of the oscillation. Because of this fact, we measured reversed resonance curves, i.e. the amplitude of the oscillation was kept constant by changing the driving force in dependence of the frequency. The measurement was carried out with the LabView program shown in Appendix A, Diagram 3. The phase difference ϕ_x-ϕ_y of signals x and y was controlled by the program and was kept equal to zero or π by the program. The amplitude of the oscillation was kept constant while the frequency was scanned near the resonance. Thus, the driving force is minimal at the resonance frequency and increases away from the resonance.

6.2.2. YBa$_2$Cu$_3$O$_{7-\delta}$

The experiments with the YBa$_2$Cu$_3$O$_{7-\delta}$ samples (YBCO-A, -B, -C) were carried out in the temperature range 50 K – 70 K and fields of about 2 – 3 T. At higher temperature the damping starts at lower magnetic field. Unfortunately, in the lower temperature range, a large hysteresis of the resonance frequency enhancement appears in increasing and decreasing field similar as observed in Ziese's dissertation [85](see Fig. 6.2.1). This irreversible magnetisation is caused by penetration of the vortices into the superconductor. This leads to a nonequilibrium distribution of the vortices in the sample and obscures the measurements. The magnitude of this effect depends on the critical current density and increases with decreasing temperature. Thus, we have tried to carry out the experiments at not too low temperatures.
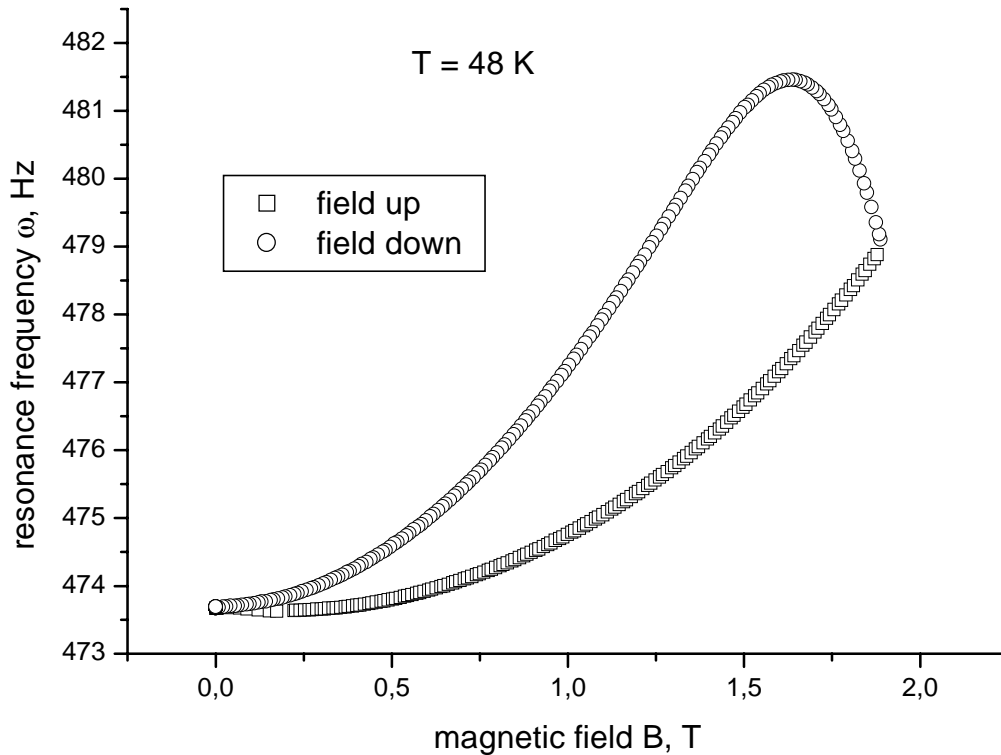
Figure 6.2.1. *The dependence of the resonance curve of the YBa$_2$Cu$_3$O$_{7-\delta}$ sample (YBCO-A) on magnetic field strength. A large hysteresis loop appears in increasing and decreasing field caused by penetration of the vortices into the superconducting sample. The temperature of the measurements is 48 K.*

Some of the experimental results are shown in Fig.6.2.2. The reverse resonance curves were measured near the resonance ω_y at a temperature $T = 66$K and magnetic field $B = 2.9$T for different angles $\alpha = 35° - 75°$. The resonance frequency differs by about 0.2Hz in different measurements. Unfortunately this effect was caused by an instability of the resonance frequency with time. The resonance frequency drifted slowly at stabilized temperature and magnetic field. For example, at temperature $T = 65$ K and field $B = 2$ T the resonance frequency decreased by ~0.15 Hz in three hours (see Fig.6.2.3). The same result was observed with other YBa$_2$Cu$_3$O$_{7-\delta}$ samples.
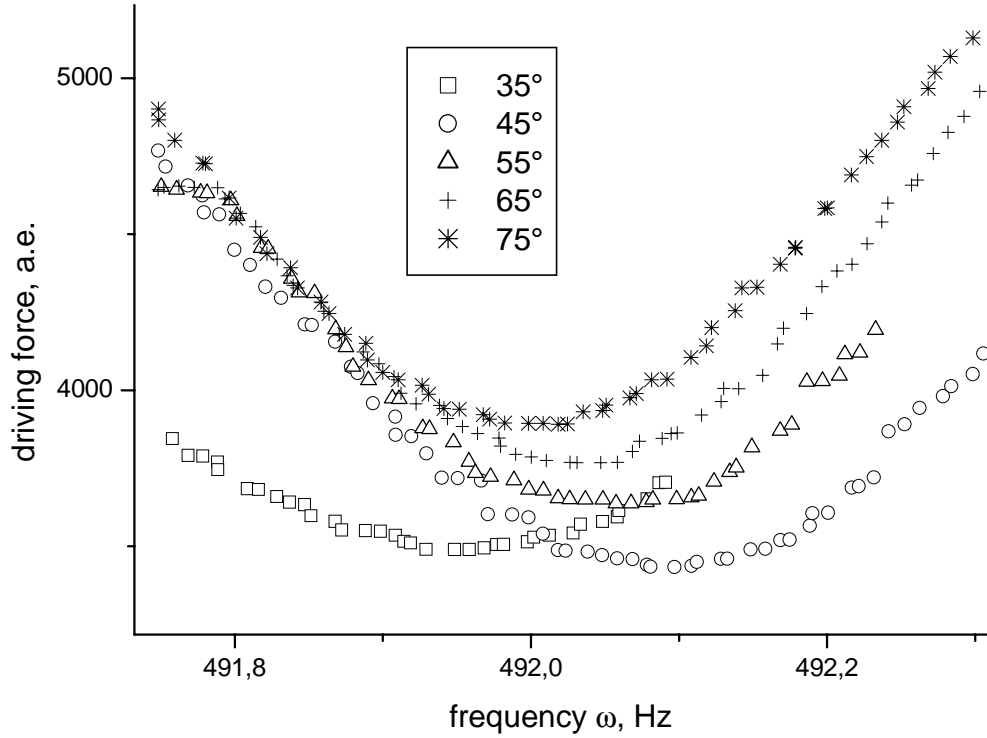
Figure 6.2.2. *Reverse resonance curves of the reed with a superconducting YBa₂Cu₃O₇₋δ crystal (YBCO-A). The measurements were carried out at T = 66K and B = 2.9T for different angles α = 35° − 75° near the resonance ωᵧ. The phase difference of x and y signal was kept equal to π.*

This effect is most likely caused by an unstable nonequilibrium state of the flux line arrangement. Since the drift of the resonance frequency is comparable to the frequency difference measured at different angles of the planar oscillation, it is impossible to obtain the dependence of the resonance curve on the angle α.
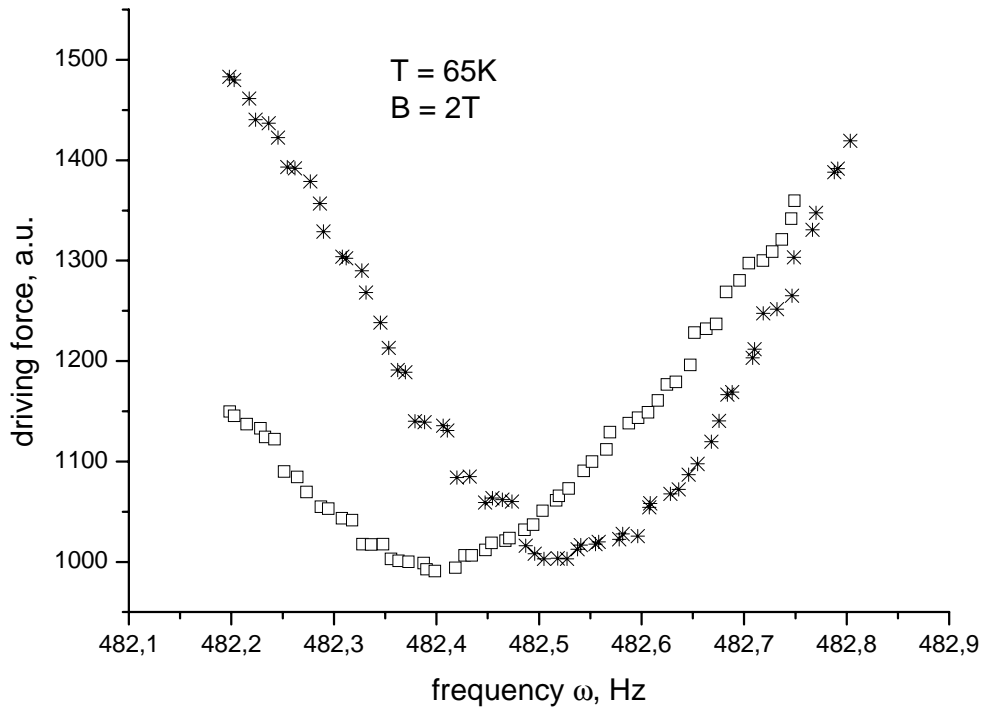
Figure 6.2.3. *Reverse resonance curves of YBa$_2$Cu$_3$O$_{7-\delta}$ sample (YBCO-A) measured at temperature 65K and magnetic field 2T. The phase difference of x and y signal was kept equal to 0 and α was 60°. The curves were measured at a different time. Within three hours, the resonance frequency has shifted by 0.15 Hz.*

6.2.3. Bi$_2$Sr$_2$CaCu$_2$O$_{8+\delta}$

The Bi$_2$Sr$_2$CaCu$_2$O$_{8+\delta}$ samples were grown at the Moscow State University in the laboratory of Prof. L.Shvanskaya. The method of growth was described in [86, 87]. Unfortunately, the crystals that we have obtained had the rather low transition temperature $T_c \approx 22$ K. Nevertheless, we carried out experiments with these samples.

For these samples, the irreversible magnetisation was much smaller than for YBa$_2$Cu$_3$O$_{7-\delta}$ crystals. It can be seen in Fig.6.2.4, which shows the dependence of the

resonance frequency on magnetic field measured at a temperature $T = 16\ K$ in increasing and decreasing field.

Evidently the vortex state in $Bi_2Sr_2CaCu_2O_{8+\delta}$ sample is much more stable than in $YBa_2Cu_3O_{7-\delta}$ crystals. The resonance frequency does not change in the observation time of several hours in stabilized magnetic field and temperature within the accuracy of the experiment.
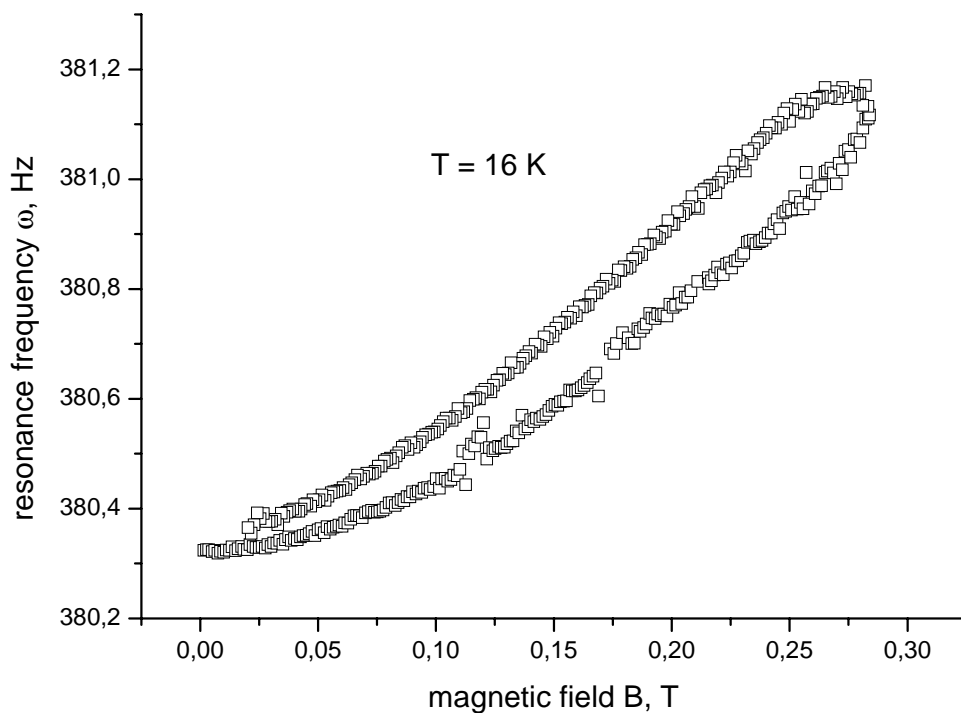
Figure 6.2.4. *The dependence of the resonance frequency of the $Bi_2Sr_2CaCu_2O_{8+\delta}$ sample on magnetic field. The hysteresis loop is smaller than that observed for the $YBa_2Cu_3O_{7-\delta}$ samples (see Fig.6.2.1). The measurements were carried out at temperature 16 K.*

A search for indications of the four-fold symmetry of the pinning potential was carried out at a temperatures of about 17 K and magnetic field lower than the depinning field,

i.e. $B = 2 - 3$ T. However the reverse resonance curves and resonance frequency show no dependence on the angle of the plane of the oscillations (Fig.6.2.5).

Another manifestation of the four-fold symmetry of the pinning potential is the appearance of an asymmetry in shape of the resonance curve (see Fig.6.2.5). Measurements of the resonance curve for plane oscillations at different angles were carried out with the LabView program similar to the program shown in Appendix A, Diagram 3, but now instead of the amplitude the driving force $|F|$ was kept constant.
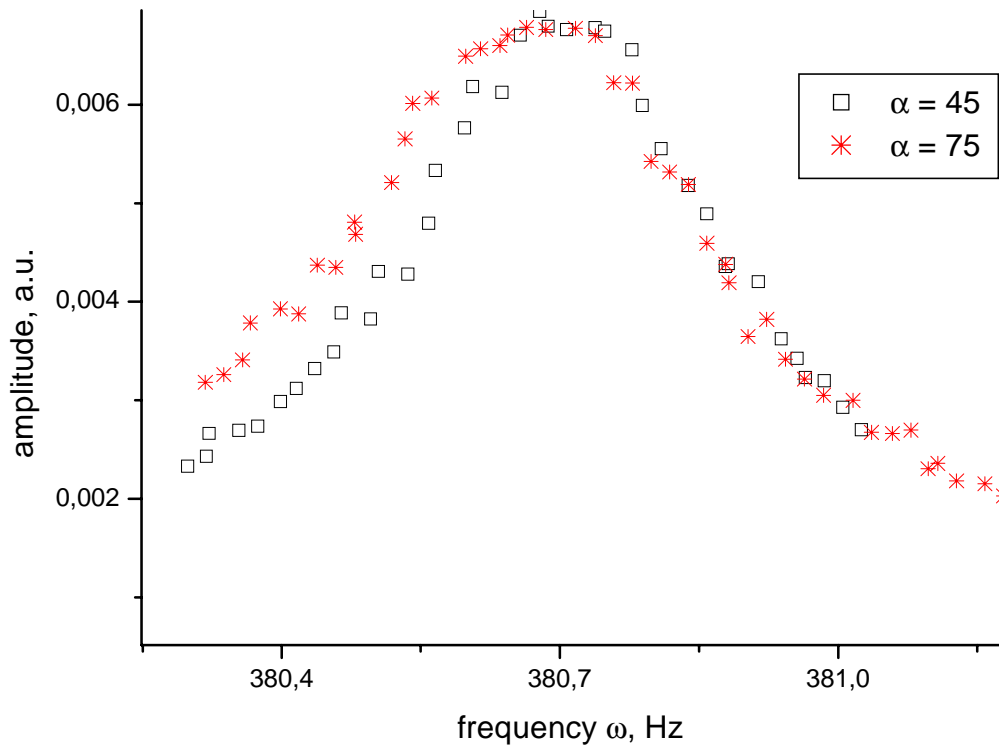
Figure 6.2.5. *Resonance curve of the $Bi_2Sr_2CaCu_2O_{8+\delta}$ sample at temperature $T = 17$ K and magnetic field $B = 2$ T. The resonance curves were measured for the oscillation at angle α equal to 45° and 75°. The difference in resonance frequency is negligible.*

The resonance curves measured at temperature $T = 17$ K and field $B = 2$ T are shown in Fig. 6.2.5. The angles of the oscillations were 45° and 75°. The difference in resonance curves is insignificant and probably caused by the measurement technique. A similar small difference of the resonance curves was observed at zero magnetic field or at temperatures above the superconducting transition.

6.3. Hysteretic behaviour

6.3.1. Resonance enhancement hysteresis

The behaviour of the reed in changing magnetic field allows an investigation of penetration of the magnetic flux into the superconductor sample and permits estimations of the critical currents of the superconductor. The shielding currents and surface barriers result in an irreversible magnetisation and hysteretic behaviour of the magnetic properties of the superconductor.

In a magnetic field a superconductor with static magnetisation M experiences a torque τ, proportional to the field and angle ϕ between applied field B_a and magnetisation. This torque leads to a change of the resonance frequency of the reed

$$\omega^2 - \omega_0^2 = \frac{V_s}{I}(B_a^2 + 2MB_a \cos\phi),$$ [6.4]

where V_s is volume of the sample and I is the effective moment of inertia of the reed. A magnetisation M is different in increasing and decreasing field and this leads to the appearance of the hysteresis in resonance frequency enhancement [85, 88]. Application of the Bean model permits to estimate critical current in the sample

$$J_c = 2(M_\downarrow - M_\uparrow)/d_s = \frac{2I}{B_a V_s d_s}(\omega_\downarrow^2 - \omega_\uparrow^2),$$ [6.5]

where $\omega_\downarrow$ and $\omega_\uparrow$ are the resonance frequencies for decreasing and increasing fields.

Our investigations also show hysteresis loops of the frequency enhancement in changing field (see Figures 6.2.1 and 6.2.4). This hysteresis is rather large for the YBa$_2$Cu$_3$O$_{7-\delta}$ crystals and depends on temperature. Figure 6.3.1 shows the frequency enhancement $\omega^2(B) - \omega^2(0)$ in a changing magnetic field at different temperatures 35 K, 50 K, 68 K and 76 K. Increasing temperature leads to decreasing hysteresis loops and at temperatures higher than 76K, hysteresis disappears. These measurements show that the critical current density increases from 10^5 A/cm^2 to 10^6 A/cm^2 in this temperature range.
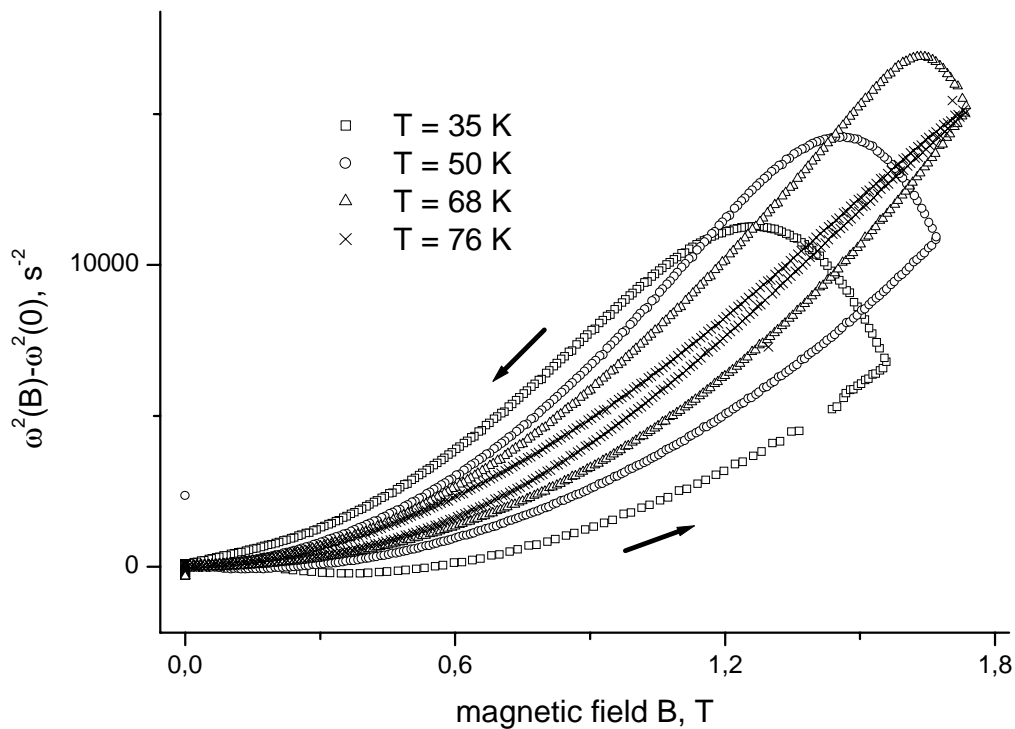
Figure 6.3.1. *Resonance frequency enhancement of YBa$_2$Cu$_3$O$_{7-\delta}$ crystals at different temperatures. The arrows show the direction of the field change. At temperatures higher than T = 76 K hysteresis is too small to be measured*

6.3.2. Amplitude hysteresis

Besides resonance frequency hysteresis at low temperature, we have observed also large hysteresis of the resonance amplitude of the oscillations. Since the vibrations were excited by constant driving force, the amplitude depends only on damping and the distance between driving/detecting electrode and the reed. However, careful measurements of the resonance curves show that the width of the resonance does not change with field up to 3 T.
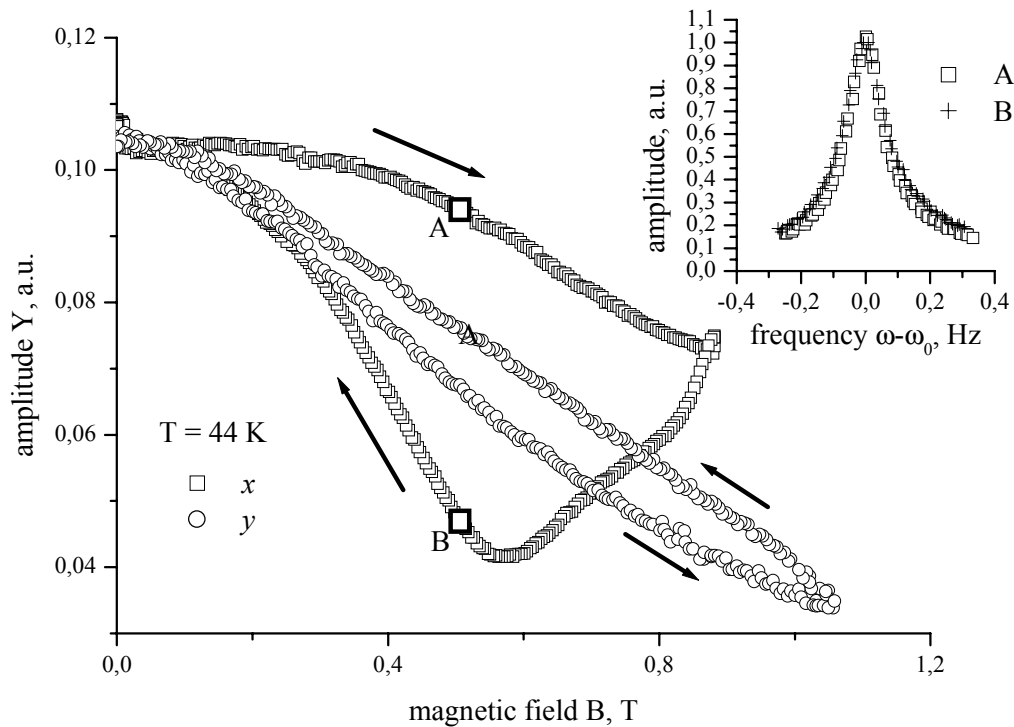
Figure 6.3.2. *The first experimental run. Large hysteresis of the amplitude of oscillations along x in magnetic field at temperature 44 K. Arrows shows the direction of the field changes. Almost no hysteresis occurred in y direction of the oscillations.*

Insert: normalised resonance curves measured in points A and B.

Figure 6.3.2 shows the hysteresis in magnetic field at temperature T = 44 K. In x direction of the oscillations we observed large hysteresis. In points A and B the amplitudes differ by almost a factor of two. However, as shown in the insert, the resonance curves in these points are the same. That means that the difference in amplitude of the oscillations is caused not by a change in damping, but by the bending of the reed. The reason of this bending is a torque, which appears in magnetic field. That means that the sample has a static magnetisation directed at some angle to the field direction.

In the experiment shown in Fig. 6.3.2, the hysteresis loop was observed only in x direction of oscillations. The signal along y direction had very small hysteresis.
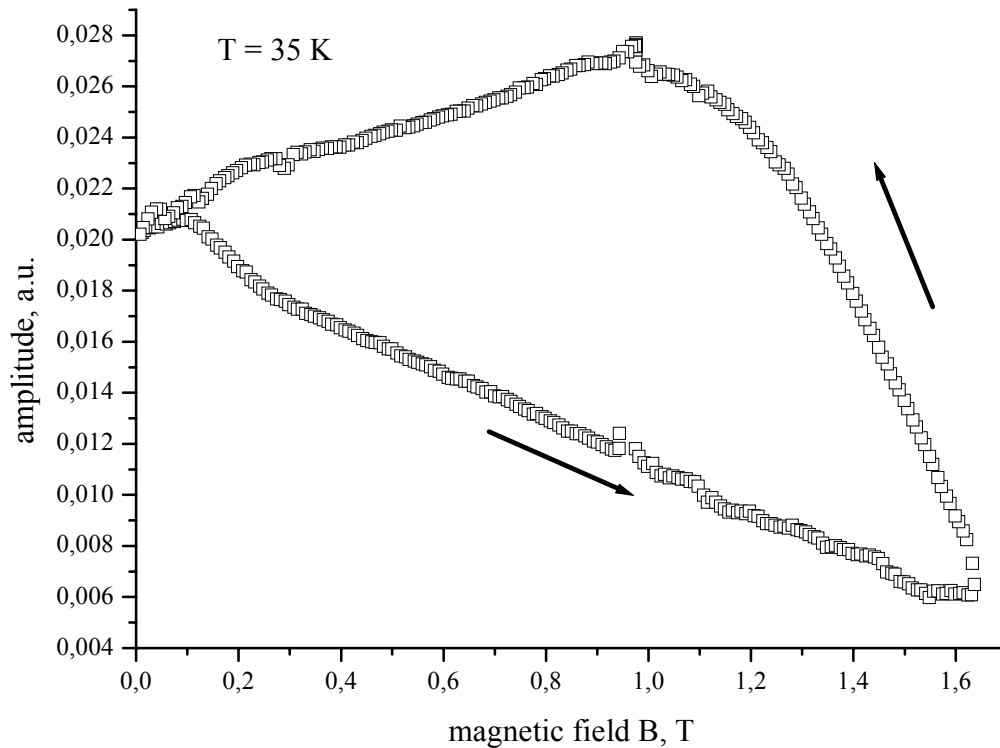
Figure 6.3.3. *The second experimental run. Hysteresis of the amplitude of oscillations along y coordinate in magnetic field at temperature 35 K. Arrows shows the direction of the field changes*

The second experimental run was carried out with the same sample turned by 90° around the *c* axis. In this case, the *a* and *b* axes are interchanged relative to the *x* and *y* directions. We now observed hysteresis in the *y* direction. However, the hysteresis had different sign, i.e. the amplitude of oscillations in decreasing field was larger than the amplitude in increasing field (see Fig.6.3.3). Another experiment shows the hysteretic behaviour in both directions (not presented).

We interpret these observations such, that hysteresis caused by the orientation of the sample relative to the direction of the applied magnetic field and the small angle between the *c* axis of the sample and field direction B_a leads to a torque bending the reed in the magnetic field.

Another interesting feature was observed at temperatures in range 45 – 60 K. The non-monotonous change of the signal in field is clearly seen in Fig. 6.3.4. The observed small bump is very similar to the "fishtail", which was reported by P. Fischer and M. Ziese in magnetization measurements [57, 85]. This effect was discussed widely in many works [89 - 93]. At present, the origin of the "fishtail" or peak effect is commonly associated with transformation of the quasiordered vortex glass into disordered amorphous vortex state [94 - 96].
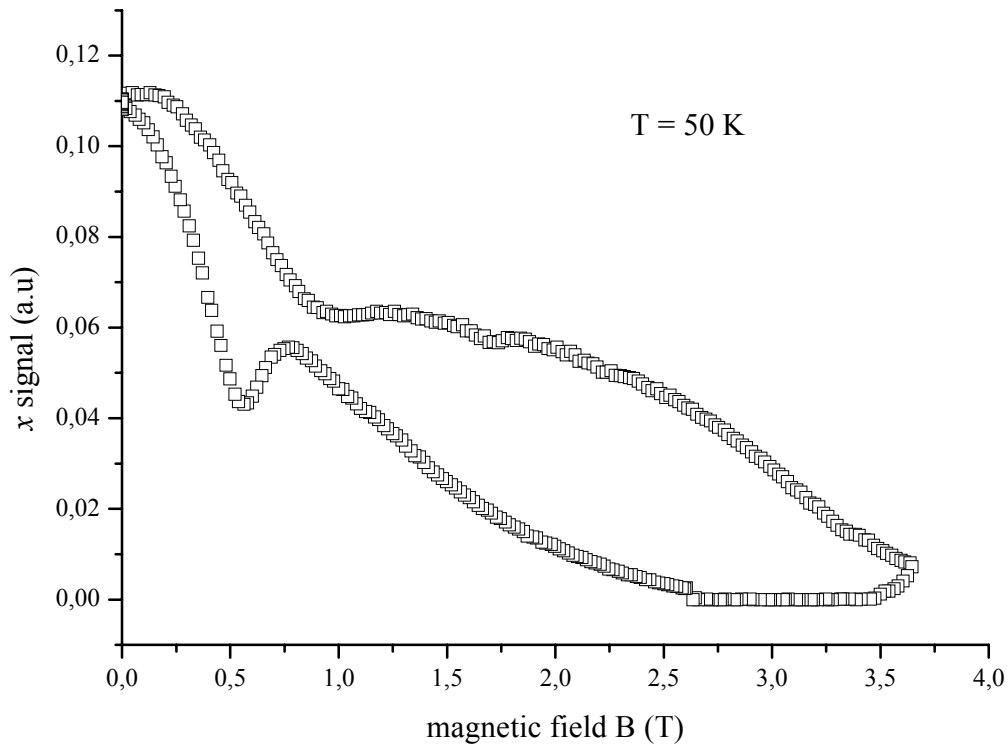
Figure 6.3.4. *The x signal changes with field non-monotonously. The measurement was carried out at T= 50 K with the sample YBCO-A.*

6.3.3. Orientation of the sample and double peak in damping

The measurements of the damping near the transition temperature verify the assumption, that the reason of the torque is the small inclination of the sample relative to the field direction. As shown in [51] (see Chapter 3.4.), the double peak structure in damping manifests depinning in the sample in the tilting magnetic field. Our experiments show that double peaks in damping and hysteresis are observed in the same directions of the oscillations. For example, in the first experimental run hysteresis was observed only for the *x* coordinate. The double peak of depinning is also observed in

this direction of the oscillations (see Fig.6.3.5). In the other direction, only one maximum with a small shoulder is observed.

Similar results were observed for other experimental runs. In all these experiments, the presence of the damping double peaks was correlated with the observation of the hysteresis. This was confirmed for six experimental runs with three different $YBa_2Cu_3O_{7-\delta}$ samples to make sure, that it is not just coincidence.

Thus we can claim that hysteretic behaviour is caused by reed bending due to the torque, which appears in the sample tilted relative to the applied magnetic field.
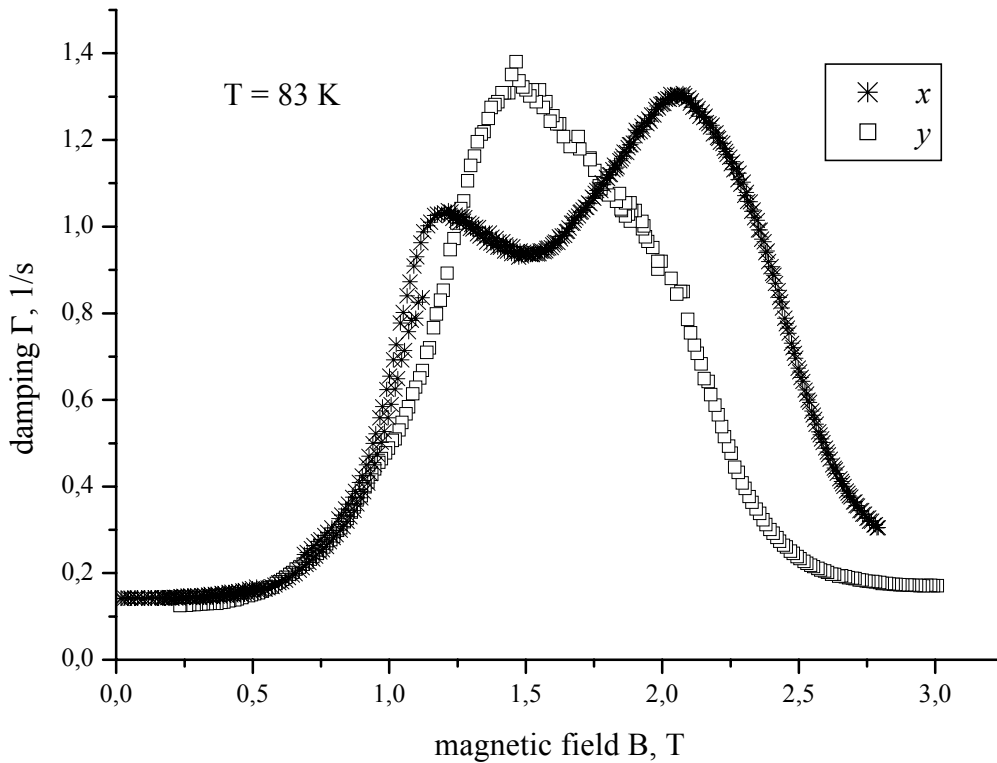
Figure 6.3.5. *Double peak in damping of YBa$_2$Cu$_3$O$_{7-\delta}$ sample in the first experimental run near T$_c$. for oscillations along x and y directions. The damping for x oscillations has a pronounced double peak. Along the y directions there is only one maximum.*

6.3.4. Magnetization of the slab in the inclined field

To understand the appearance of the torque bending the reed in a magnetic field, it is necessary to consider the magnetisation of a superconductor in increasing and decreasing magnetic field. This problem was analyzed in many papers for samples of different simple shapes and different orientation relative to the field direction [97-102] and was reviewed in [103].

To compare our configuration with these cases one should consider field and magnetisation components parallel and perpendicular to the *ab* plane of the superconductor as shown in figure 6.3.6.
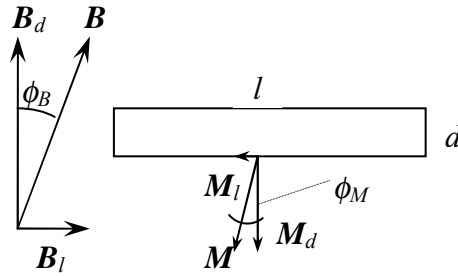
Figure 6.3.6. *Magnetization of the superconducting slab in the tilted magnetic field. Field and magnetization can be resolved into components parallel and perpendicular to the slab.*

According to the Bean model [97, 98] the field, parallel to the *ab* planes B_l, causes the appearance of shielding currents which lead to a negative magnetisation

$$M_l = J_c d \left(\frac{2H_l}{H_c} - \frac{H_l^2}{H_c^2} \right). \qquad [6.6]$$

Here we assume that $B(H_a) = \mu_0 H_a$. In equation [6.6] H_c and J_c denotes critical field and critical current density.

In our case we apply a magnetic field $B \geq 1T$ and the angle of the field inclination ϕ_B can be about 1–3°. That means that $H_l \ll H_c$ and we have the ideal shielding case in which the applied field is expelled completely. Then the magnetisation is

$$M_l = H_l d. \tag{6.7}$$

For an estimate of the magnetization component parallel to the c axis it is necessary to use the solutions for the transverse geometry. In this configuration, the original model has to be modified. The problem of flux penetration was solved analytically for a thin circular disc in [99, 100, 103] and we can use this result in our case neglecting the rectangular shape of the superconducting crystal. The solution for the disc of radius l is the negative magnetic moment

$$M_d = \frac{8}{3} H_d l S\left(\frac{H_d}{H_c}\right) \tag{6.8}$$

where

$$S(x) = \frac{1}{2x}\left(\arccos\frac{1}{\cosh x} + \frac{\sinh|x|}{\cosh^2 x}\right). \tag{6.9}$$

At $B \geq 1T$ we have full penetration, and the magnetisation is equal to [103]

$$M_d = \frac{2\pi}{3} l H_c \tag{6.10}$$

Thus from equations [6.7] and [6.10] we can determine the angle between the magnetisation and the c axis of the superconductor

$$\phi_M = \frac{3}{2\pi}\frac{d}{l}\frac{H_l}{H_d} = \frac{3}{2\pi}\frac{d}{l}\phi_B. \tag{6.11}$$

That means that the negative magnetisation is not parallel to the inclined applied field mainly because of the geometric parameters of the sample. Since the thickness d of the sample usually is 10–20 times smaller than its longitudal dimension l, the magnetisation is almost parallel to the c axis of the sample. Thus, the angle between applied magnetic field and magnetisation of the sample is almost equal to ϕ_B. When this angle is not zero, the torque acts on the sample and bends the reed toward the electrodes or away from them in dependence of the direction of the inclination of the sample. This leads to an increase or decrease of the amplitude of oscillations in increasing magnetic field. When the magnetic field is decreasing, the magnetisation changes sign and the reed bends in the opposite direction. This results in hysteresis of the amplitude of oscillations.

6.3.5. Sensitivity of torque measurements

These experiments are very similar to the usual torque measurements with the sample glued to a cantilever, which bends in magnetic field. It is easy to estimate the sensitivity of our torque measurements knowing that the signal from detection electrode depends on the fourth power of the distance d between reed and electrode. This follows from the equations [4.2]:

$$V_{signal} = K\Delta C = \frac{K}{2m^*\Gamma\omega}\frac{\varphi^2 C^2}{d^2} = \frac{K\varphi^2}{2m^*\Gamma\omega}\frac{\varepsilon_0^2 A^2}{d^4} = \frac{k}{d^4} \qquad [6.12]$$

where K is the coefficient of the tuner convertion; m^*, Γ and ω are parameters of the reed; A is the effective surface of the reed/electrode capacitance and φ is the driving voltage. Thus the change of the signal can be found:

$$\Delta V_{signal} = k\left(\frac{1}{d^4} - \frac{1}{(d+\Delta d)^4}\right) = \frac{k}{d^4}\frac{4\Delta d}{d} = V_{signal}\frac{4\Delta d}{d}. \qquad [6.13]$$

From here we can determine how the change of the torque determines the signal change:

$$\Delta\tau = \frac{I\omega^2}{l}\Delta d = \frac{I^*\omega^2}{l}\frac{d\Delta V_{signal}}{V_{signal}}. \qquad\qquad [6.14]$$

where l is the length of the reed (7mm), $I^* \sim m^*l^2$ is the effective moment of inertia and ω is the resonance frequency of the reed. Thus we can estimate the sensitivity of the torque measurements which is about 10^{-9} Nm.

Another method of torque measurements, described in part 6.3.1, gives much higher sensitivity. In this method, the torque is measured by changes of resonance frequency and very high quality factor of the vibrating reed allows to realise extremely sensitive measurements, since the torque τ leads to resonance frequency enhancement (see Chapter 3)

$$\delta(\omega^2 - \omega_0^2) = \frac{\tau}{I^*}\frac{l}{a}, \qquad\qquad [6.15]$$

where a is the amplitude of the oscillations. The high quality factor permits to measure $\delta\omega$ with a sensitivity of about 0.01 s^{-1}. Thus the minimal measurable value of $\delta(\omega^2 - \omega_0^2) \cong 2\omega_0\delta\omega$ is about 10 s^{-2}. This gives an estimate for the torque sensitivity of 10^{-14}Nm.

In addition, we can compare the torque values obtained with both methods. From equations [6.5] and [6.14] we can find the ratio of the torque τ_1 obtained by the resonance measurements and the torque τ_2 obtained by the measurements of the oscillation amplitude:

$$\frac{\tau_1}{\tau_2} = 4\frac{\Delta\omega^2}{\omega^2}\frac{l}{d}\frac{V_{signal}}{\Delta V_{signal}}.$$

Since the torque caused by magnetisation M in field B_a is proportional to the angle between them, the ratio of the torques is equal to the ratio of the angles in both

cases $\dfrac{\tau_1}{\tau_2} = \dfrac{\theta}{\phi}$. Here θ is angle of the reed distortion at oscillations, and ϕ is angle of inclination of the sample relative to the field direction. If we substitute the parameters from the experiment $l = 10^{-2}$ m, $d = 2 \cdot 10^{-6}$ m, $\Delta\omega^2 = \delta(\omega^2 - \omega_0^2) = 8 \cdot 10^3$ s^{-2} and $\omega^2 = 16 \cdot 10^4$ s^{-2}, we get the ratio $\theta/\phi = 2000$. Taking the approximate value of the amplitude of oscillation as 100nm we find the $\theta = 10^{-5}$ and consequently $\phi = 1°$. This estimation gives rather consistent result proving the validity of our assumptions.

Chapter 7

Conclusions

In this work the anisotropy of the pinning forces in the *ab* plane of single crystals of high-temperature superconductors was studied. For this purpose a vibrating reed with two degrees of freedom was constructed. This device allows measuring the shape of the pinning potential in $YBa_2Cu_3O_{7-\delta}$ and $Bi_2Sr_2CaCu_2O_{8+\delta}$ single crystals.

7.1. Two-dimensional vibrating reed

For the study of the *ab* anisotropy of the pinning forces acting on the vortices the two-dimensional vibrating reed was built. This reed consists of a sapphire fiber glued into a hole of the ruby disc, which is used as a sample holder. The superconducting sample was glued on top of the disc with the c-axis parallel to the sapphire fiber. Thus we have the possibility to vibrate the sample in any direction of the *ab* plane. The magnetic field directed along the *c* axis creates vortices in the superconductor. Vibrating of the superconductor leads to the distortion of the flux lines and displacement of the vortices from the point-like oxygen defects, which act as pinning centers. Such an experimental configuration has never been used before and gives the possibility to study the symmetry of the pinning potential.

7.2. Mathematical model

A mathematical model was developed to describe the effect of the shape of the pinning potential on the vibrating reed motion. The two simplest cases of two- and four-fold symmetry of the potential were considered in this model.

According to the equations of motion it is clear that it is possible to make the two-dimensional reed move in a plane, thus the free end of the reed moves along a straight line trajectory. In this case it was proven that the two-fold symmetry of the potential leads to a change in the dependence of the reed displacement (x,y) on the driving force (F_x, F_y). The dependence of the motion direction $\alpha = \arctan(|x|/|y|)$ on the driving force direction $\beta = \arctan(|F_x|/|F_y|)$ was studied. The presence of two-fold symmetry results in shift of the curve of α versus β. This shift depends on the parameter of anisotropy and this fact gives a clue to the experimental measurements of the anisotropy by the vibrating reed with two degrees of freedom.

The mathematical model of the reed motion in a potential with four-fold symmetry has been developed. According to this model the four-fold symmetry should manifest itself in a change of the resonance curve in dependence on the angle of the plane of the oscillations. For an oscillation in a plane at 45° to the crystallographic axes, the shift of the resonance frequency is expected to be maximal and the resonance curve should have asymmetry shape.

7.3. Two-fold symmetry

The experiments with the two-dimensional vibrating reed were carried out with single crystals of $YBa_2Cu_3O_{7-\delta}$, glued with some angle between the easy axis of the reed (the x direction) and the crystallographic axis a and b. These experiments demonstrated the

presence of the two-fold symmetry of the pinning potential of the sample. The anisotropy of the pinning potential manifests itself by the appearance of beating in the free oscillations.

Moreover the experiments with the in-plane oscillations at constant drive give the results predicted by the mathematical model. The direction of the oscillations α depends on the direction of the driving force β as it was expected. The dependence curve α versus β shifted in magnetic field proving that pinning potential has two-fold symmetry. The mathematical simulations allow to estimate the anisotropy parameter from the experimental data. This parameter appears to be about 10% which is in a good agreement with experimental measurements of the anisotropy in the penetration depth and in the magnetic torque

7.4. Four-fold symmetry

The experiments with the samples glued so that the crystallographic axes coincide with the easy axes of the reed eliminate the effect of the two-fold symmetry of the pinning potential. Unfortunately, the experiments with $YBa_2Cu_3O_{7-\delta}$ show that at temperatures lower than 78K the vortices are in a nonequilibrium state. This leads to a drift of the resonance frequency with time and prevents the comparison of resonance curves in different directions of oscillations.

In $Bi_2Sr_2CaCu_2O_{8+\delta}$ single crystals the vortices are in more stable state, but the measurements of the resonance curves in different directions show no indication of the four-fold symmetry.

7.5. Amplitude hysteresis

The experiments carried out at temperatures lower than 60K with $YBa_2Cu_3O_{7-\delta}$ crystals reveals strong hysteretic behaviour in changing magnetic field. Hysteresis of the

resonance frequency enhancement caused by irreversible magnetisation was observed earlier in vibrating reed experiments. However the hysteresis of the amplitude of the oscillation was observed for the first time. It was verified experimentally by measuring resonance curves that the damping does not change in a small field in this range of temperature. The damping increases only at fields higher than 2 T, when the depinning starts. From this we conclude that the change in the measured signal is caused by the change of the gap between the reed and the driving/detecting electrode because of bending of the reed. This bending is the result of a torque caused by the irreversible magnetisation. This magnetisation is directed mainly perpendicular to the flat surface of the superconductor because of a geometrical shape of the sample. At a consequence, the small inclination of the sample relative to the magnetic field direction leads to the appearance of the torque which bends the reed. A comparison of the values of the magnetisation estimated from the measured hysteresis of the resonance frequency and hysteresis of the signal gives a consistent result. This proves that our assumption of the origin of the hysteresis of the measured signal is correct.

Literature

1. J. G. Bednorz, and K. A. Müller:, Z.Phys. B64, 189 (1986).

2. H. F. Hess, R. B. Robinson, R. C. Dynes, J. M. Valles, Jr., and J. V. Waszczak: Phys. Rev. Lett. 62, 214–216 (1989).

3. A. Chang, Zhao Y. Rong, Yu. M. Ivanchenko, Farun Lu, and E. L. Wolf: Phys. Rev. B 46, 5692–5698 (1992).

4. J. Annett, N. Goldenfeld, and S.R. Renn: Phys. Rev. B 43, 2778–2782 (1991).

5. H. Monien, P. Monthoux, and D. Pines: Phys. Rev. B 43, 275–287 (1991).

6. S. E. Barrett, J. A. Martindale, D. J. Durand, C. H. Pennington, C. P. Slichter, T. A. Friedmann, J. P. Rice, and D. M. Ginsberg: Phys. Rev. Lett. 66, 108–111 (1991).

7. N. E. Bickers, D. J. Scalapino, and S. R. White: Phys. Rev. Lett. 62, 961–964 (1989).

8. M.Ziese, P.Esquinazi, and H.F. Braun: Supercond. Sci. Technol. 7, 869-890 (1994).

9. J. A. Martindale, S. E. Barrett, K. E. O'Hara, C. P. Slichter, W. C. Lee, and D. M. Ginsberg: Phys. Rev. B 47, 9155–9157 (1993).

10. Z.–X. Shen, D. S. Dessau, B. O. Wells, D. M. King, W. E. Spicer, A. J. Arko, D. Marshall, L. W. Lombardo, A. Kapitulnik, P. Dickinson, S. Doniach, J. DiCarlo, T. Loeser, and C. H. Park: Phys. Rev. Lett. 70, 1553–1556 (1993).

11. Jeffrey Kane, Qun Chen, K.–W. Ng, and H.–J. Tao: Phys. Rev. Lett. 72, 128–131 (1994).

12. T. P. Devereaux, D. Einzel, B. Stadlober, R. Hackl, D. H. Leach, and J. J. Neumeier: Phys. Rev. Lett. 72, 396–399 (1994).

13. T. Ishida, K. Okuda, H. Asaoka, Y. Kazumata, K. Noda, and H. Takei: Phys. Rev. B 56, 11897–11902 (1997)

14. M. Willemin, C. Rossel, J. Hofer, H. Keller, Z. F. Ren, and J. H. Wang: Phys. Rev. B 57, 6137–6144 (1998).

15. D. J. Van Harlingen: Rev. Mod. Phys. 67, 515–535 (1995).

16. V. B. Geshkenbein, A. I. Larkin, and A. Barone: Phys. Rev. B 36, 235–238 (1987).

17. M. Sigrist and T. M. Rice: J. Phys. SocJpn. 61, 4283 (1992)

18. D. A. Wollman, D. J. Van Harlingen, J. Giapintzakis, and D. M. Ginsberg: Phys. Rev. Lett. 74, 797–800 (1995).

19. A. G. Sun, D. A. Gajewski, M. B. Maple, and R. C. Dynes: Phys. Rev. Lett. 72, 2267–2270 (1994).

20. P. Chaudhari and Shawn–Yu Lin: Phys. Rev. Lett. 72, 1084–1087 (1994).

21. M. H. S. Amin, A. N. Omelyanchouk, S. N. Rashkeev, M. Coury, and A. M. Zagoskin

22. M. Sigrist, D. B. Bailey, and R. B. Laughlin: Phys. Rev. Lett. 74, 3249–3252 (1995).

23. M. Matsumoto and H. Shiba, J. Phys. Soc. Jpn. 65, 2194 (1996).

24. T. Ishida, K. Okuda, H. Asaoka, Y. Kazumata, K. Noda, and H. Takei: J. Low Temp. Phys. 105, 1165

25. M. Endres, unpublished, private communications

26. E. V. Thuneberg, J. Kurkijärvi and D. Rainer: Phys. Rev. B 29, 3913–3923 (1984).

27. A. I. Larkin and Yu. V. Ovchinnikov: J. Low Temp. Phys. 34, 409 (1979).

28. P. Esquinazi: J. of Low Temp. Phys. 85, 139–232 (1991).

29. R. Labusch: Crystal Lattice Defects 1, 1 (1969).

30. E. H. Brandt, P. Esquinazi, H. Neckel, and G. Weiss: Phys. Rev. Lett. 56, 89–92 (1986).

31. P. L. Gammel, L. F. Schneemeyer, J. V. Wasczak, and D. J. Bishop: Phys. Rev. Lett. 61, 1666–1669 (1988).

32. P. J. Flanders: Journal of Applied Physics 63, 3940-3945 (1988)

33. G. D'Anna, W. Benoit, W Sadovski, and E. Walker: Europhys. Lett. 20, 167 (1992).

34. E. H. Brandt: J. of Low Temp. Phys. 26, 709 (1977).

35. E. H. Brandt and A. Sudbø: Physica C 180, 426 (1991).

36. A. Gupta, Y. Kopelevich, M. Ziese, P. Esquinazi, P. Fischer, F. I. Schulz, and H. F. Braun: Phys. Rev. B 48, 6359–6372 (1993).

37. E. H. Brandt, P. Esquinazi, and H. Neckel: J. of Low Temp. Phys. 63, 187 (1986)

38. A. M. Campbel and J. E. Evetts: Critical Currents in Superconductors (1972).

39. E. H. Brandt: Reports on Progress in Physics. Version of 10 March 1995.

40. P. Esquinazi, H. Neckel, G. Weiss, and E. H. Brandt: J. of Low Temp. Phys. 64, 1 (1986)

41. J. Kober, A. Gupta, P. Esquinazi, H. F. Braun, and E. H. Brandt: Phys. Rev. Lett. 66, 2507–2510 (1991).

42. .A. Gupta: Doctoral dissertation, Bayreuth (1992).

43. D. Dew-Hughes: Cryogenics 28, 674 (1988).

44. P. H. Kes, J. Aarts, j. van den Berg, C. J. van der Beek, and J. A. Mydosh: Supercond. Sci. Technol. 1, 242 (1989).

45. P. W. Anderson and Y. B. Kim: Rev. Mod. Phys. 36, 39–43 (1964).

46. M. R. Beasley, R. Labusch, and W. W. Webb: Phys. Rev. 181, 682–700 (1969).

47. E. H. Brandt: Z. Phys. B, 80, 167 (1990).

48. V. B. Geshkenbein, V. M. Vinokur, and R. Fehrenbacher: Phys. Rev. B 43, 3748–3751 (1991).

49. E. H. Brandt: Phys. Rev. Lett 67, 2219 (1991).

50. M. W. Coffey and J. R. Clemm: Phys. Rev. Lett 67, 386 (1991).

51. E. H. Brandt: Phys. Rev. Lett. 68, 3769–3772 (1992).

52. C. Duran, J. Yazyi, F. de la Cruz, D. J. Bishop, D. B. Mitzi, and A. Kapitulnik: Phys. Rev. B 44, 7737–7740 (1991).

53. Y. Kopelevich, A. Gupta, P. Esquinazi, C. -P. Heidmann, and H. Müller: Physica C 183, 345-354 (1991).

54. J. Yazyi, A. Arribére, C. Durán, F. de la Cruz, D. B. Mitzi, and A. Kapitulnik: Physica C 184, 254–258 (1991).

55. L. Krusin-Elbaum, L. Civale, T. K. Worthington and F. Holtzberg: Physica 185-189C, 2337–2338 (1991).

56. M. Ziese, P. Esquinazi, Y. Kopelevich, and A. B. Sherman: PhysicaC 224, 79–90 (1994).

57. P. Fischer: Doctoral dissertation, Bayreuth (1993).

58. K. Aizu: Phys. Rev. B 2, 754 (1970).

59. H. Schmid, E. Burkhardt, E. Walker, W. Brixel, M. Clin, J.-P. Rivera, J.L. Jorda, M. Francois, and K. Yvon: Z. Phys. B 72, 305 (1988).

60. H. Schmid, J.-P. Rivera, M. Clin, A. Williams, and E. Burkhardt: Physica C 153-155, 1748 (1988).

61. L. J. Swartzendruber, A. Roitburd, D. L. Kaiser, F. W. Gayle, and L. H. Bennett: Phys. Rev. Lett. 64, 483–486 (1990).

62. W. K. Kwok, U. Welp, G. W. Crabtree, K. G. Vandervoort, R. Hulscher, and J. Z. Liu: Phys. Rev. Lett. 64, 966–969 (1990).

63. H. Schmidt, E. Burkhardt, B.N. Sun, and J.-P. Rivera: Physica C 157, 555-560, (1989).

64. T. Hatanaka and A Sawada: Jpn. J. of Appl. Phys. 28, L392 (1989).

65. U Welp, M. Grimsdithch, H. You, W. K. Kwok, M.M. Fang, G. W. Crabtree, and J. Z. Liu: Physica C 161, 1 (1989).

66. E. Burkhardt, Z.-G. Ye and H. Schmid: Rev. Sci. Instrum. 66, 3888-3893 (1995).

67. R. J. Cava, B. Batlogg, C. H. Chen, E. A. Rietman, S. M. Zahurak, and D. Werder: Phys. Rev. B 36, 5719–5722 (1987).

68. M. Tokumoto, H. Ihara, T. Matsubara, M. Hirabayashi, N. Terada, H. Oyanagi, K. Murata, and Y. Kimura: Jpn. J.of Appl. Phys. 26, L1565 (1987).

69. P. Meuffels, B. Rupp, and E. Pörschke: Physica C 156, 441-447 (1988).

70. J. D. Jorgensen, B. W. Veal, A. P. Paulikas, L. J. Nowicki, G. W. Crabtree, H. Claus, and W. K. Kwok: Phys. Rev. B 41, 1863–1877 (1990).

71. R. J. Cava, B. Batlogg, C. H. Chen, E. A. Rietman, S. M. Zahurak, and D. Werder: Phys. Rev. B 36, 5719–5722 (1987).

72. R. J. Cava, B. Batlogg, C. H. Chen, E. A. Rietman, S. M. Zahurak, and D. Werder: Nature 329, 423 (1987).

73. D. J. Werder, C. H. Chen, R. J. Cava, and B. Batlogg: Phys. Rev. B 37, 2317–2319 (1988).

74. R. Beyers, B. T. Ahn, G. Gorman, V. Y. Lee, S. S. P. Parkin, M. L. Ramirez, K. P. Roche, J. E. Vazqez, T. M. Gur, and R. A. Huggins: Nature 340, 619 (1989).

75. C. Chaillout, M. A. Alario-Franco[*], J. J. Capponi, J. Chenavas, J. L. Hodeau, and M. Marezio: Phys. Rev. B 36, 7118–7120 (1987).

76. J. D. Jorgensen, M. A. Beno, D. G. Hinks, L. Soderholm, K. J. Volin, R. L. Hitterman, J. D. Grace, I K. Schuller, C. U. Segre, K. Zhang, and M. S. Kleefisch: Phys. Rev. B 36, 3608–3616 (1987).

77. D. Shi and D. W. Capone: Appl. Phys. Lett. 53, 159-161 (1988).

78. J. P. Rice, E. D. Bukowski, and D. M. Ginsberg: J. of Low Temp. Phys. 77, 119-132 (1989).

79. R. Beyers and B. T. Ahn: Annu. Rev. Mater. Sci. 21, 335 (1991).

80. R. A. Hein, T. L. Francavilla, and D. H. Liebenberg, Eds "Magnetic Susceptibility of Superconductors and other spin Systems" (1992)

81. D. -X. Chen, A. Sanchez, T. Puig, L. M. Martinez and J. S. Muñoz: Physica C 168, 652-667 (1990).

82. L. D. Landau and E. M. Lifshits: Theoretical Course of Physics, I Mechanics (1988).

83. D. N. Basov, R. Liang, D. A. Bonn, W. N. Hardy, B. Dabrowski, M. Quijada, D. B. Tanner, J. P. Rice, D. M. Ginsberg, and T. Timusk: Phys. Rev. Lett. 74, 598–601 (1995).

84. Takekazu Ishida, Kiichi Okuda, Hidehito Asaoka, Yukio Kazumata, Kenji Noda, and Humihiko Takei: Phys. Rev. B 56, 11897–11902 (1997).

85. M. Ziese: Doctoral dissertation, Bayreuth (1995)

86. E. L. Belokoneva, L. I. Leonyuk, G.–J. Babonas, and V. S. Urusov: Superconductivity 2, 25 (1989).

87. L. Leonyuk, G.-J. Babonas, V. Rybakov, E. Sokolova, R. Szymczak, V. Maltsev, and L. Shvanskaya: J.Phys.Chem.Solids, v.59, 1591-1595 (1998)

88. Y. T. Wen, T. S. Ke, H. G. Bohn, H. Soltner, and W. Schilling: J. Phys.: Condens. Matter 4, 4519-4526 (1992).

89. M. Jirsa, L. Pust, D. Dlouhý, and M. R. Koblischka: Phys. Rev. B 55, 3276-3284 (1997).

90. L. Klein, E. R. Yacoby, Y. Yeshurun, A. Erb, G. Müller–Vogt, V. Breit, and H. Wühl: Phys. Rev. B 49, 4403–4406 (1994).

91. A. A. Zhukov, H. Küpfer, H. Claus, H. Wühl, M. Kläser, and G. Müller–Vogt: Phys. Rev. B 52, R9871–R9874 (1995).

92. K. Deligiannis, P. A. J. de Groot, M. Oussena, S. Pinfold, R. Langan, R. Gagnon, and L. Taillefer: Phys. Rev. Lett. 79, 2121–2124 (1997).

93. L. Krusin–Elbaum, L. Civale, V. M. Vinokur, and F. Holtzberg: Phys. Rev. Lett. 69, 2280–2283 (1992)

94. Y. Paltiel, E. Zeldov, Y. Myasoedov, M. L. Rappaport, G. Jung, S. Bhattacharya, M. J. Higgins, Z. L. Xiao, E. Y. Andrei, P. L. Gammel, and D. J. Bishop: Phys. Rev. Lett. 85, 3712–3715 (2000).

95. T. Nishizaki, T. Naito, S. Okayasu, A. Iwase, and N. Kobayashi: Phys. Rev. B 61, 3649–3654 (2000).

96. G. P. Mikitik and E. H. Brandt: Phys. Rev. B 64, 184514 (2001).

97. C. P. Bean: Rev. Mod. Phys 36, 31 (1964).

98. C. P. Bean: J. appl. Phys. 41, 2482 (1970).

99. P. N. Mikheenko and Kuzovlev: Physica C 204, 229 (1993).

100. J. Zhu, J. Mester, J. lockhart, and J. Turneaure: Physicaa C 212, 216 (1993).

101. E. H. Brandt: Phys. Rev. B 48, 6699–6702 (1993).

102. E. H. Brandt: Phys. Rev. Lett. 71, 2821–2824 (1993).

103. E. H. Brandt: Review for „Reports on Progress in Physics" (1995)

Acknowledgments